

AD-A112 904

PENNSYLVANIA STATE UNIV UNIVERSITY PARK DEPT OF CHEMISTRY F/8 7/4
CHARACTERIZATION OF SOLIDS AND SURFACES USING ION BEAMS AND MAS--ETC(U)
DEC 81 N WINOGRAD
N00014-80-C-0491

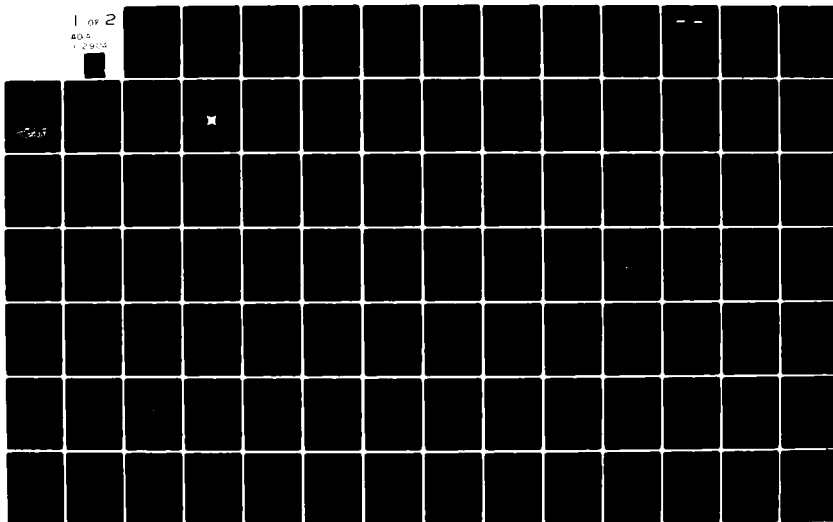
UNCLASSIFIED

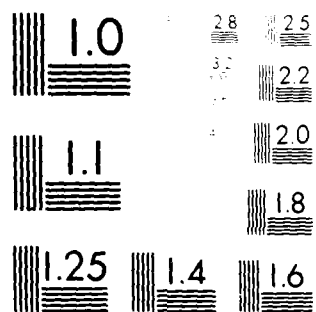
TR-4

NL

1 of 2

AD-A
1 2904





MICROCOPY RESOLUTION TEST CHART
NATIONAL BUREAU OF STANDARDS-1963-A

OFFICE OF NAVAL RESEARCH

Contract N00014-80-C0491

Task No. NR-051-744

TECHNICAL REPORT No. 4

//

Characterization of Solids and Surfaces
Using Ion Beams and Mass Spectrometry

by

Nicholas Winograd

Prepared for Publication

in

Progress in Solid State Chemistry

The Pennsylvania State University
Department of Chemistry
University Park, PA 16802-6389

December 1981

Reproduction in whole or in part is permitted for
any prupose of the United States Government.

This document has been approved for public release
and sale; its distribution is unlimited.

DTIC
ELECTED
APR 2 1982

A

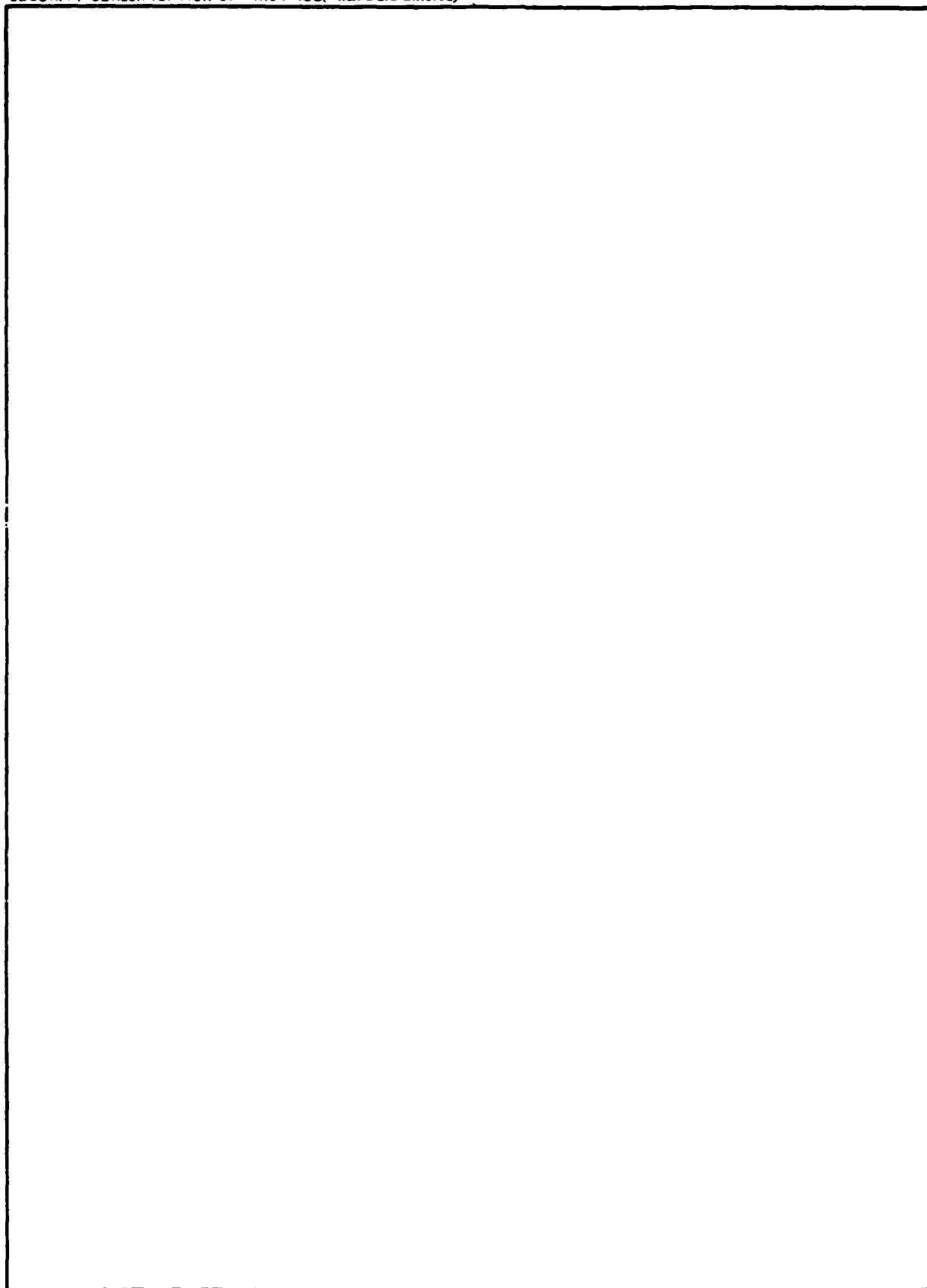
81 12 23 138

ADA 112 4

DTIC FILE COPY

REPORT DOCUMENTATION PAGE		READ INSTRUCTIONS BEFORE COMPLETING FORM
1. REPORT NUMBER	2. GOVT ACCESSION NO.	3. RECIPIENT'S CATALOG NUMBER
4. TITLE (and Subtitle) Characterization of Solids and Surfaces Using Ion Beams and Mass Spectrometry		5. TYPE OF REPORT & PERIOD COVERED Technical Report
		6. PERFORMING ORG. REPORT NUMBER
7. AUTHOR(s) Nicholas Winograd		8. CONTRACT OR GRANT NUMBER(s) N00014-80-C0491
9. PERFORMING ORGANIZATION NAME AND ADDRESS Chemistry Department The Pennsylvania State University University Park, PA 16802-6389		10. PROGRAM ELEMENT, PROJECT, TASK AREA & WORK UNIT NUMBERS NR-051-744
11. CONTROLLING OFFICE NAME AND ADDRESS		12. REPORT DATE December 1981
		13. NUMBER OF PAGES 91
14. MONITORING AGENCY NAME & ADDRESS (if different from Controlling Office)		15. SECURITY CLASS. (of this report) Unclassified
		15a. DECLASSIFICATION, DOWNGRADING SCHEDULE
16. DISTRIBUTION STATEMENT (of this Report) This document has been approved for public release and sale; its distribution is unlimited.		
17. DISTRIBUTION STATEMENT (of the abstract entered in Block 20, if different from Report)		
18. SUPPLEMENTARY NOTES To be published in <u>Progress in Solid State Chemistry</u> .		
19. KEY WORDS (Continue on reverse side if necessary and identify by block number) ion bombardment, SIMS, surface science		
20. ABSTRACT (Continue on reverse side if necessary and identify by block number) In this review, we will examine the possibility of utilizing energetic ion beams as tools to characterize the chemistry and structure of solids and surfaces. This approach may appear somewhat unusual to most spectroscopists who are generally concerned with the quantum mechanical interaction of electromagnetic radiation with matter. But, there have been a number of developments that have surfaced over the last few years which have attracted our attention to this particular field and which merit close consideration.		

SECURITY CLASSIFICATION OF THIS PAGE(When Data Entered)



SECURITY CLASSIFICATION OF THIS PAGE(When Data Entered)

Table of Contents

	<u>Page</u>
I. Introduction.....	1
II. Ion Bombardment Methods.....	4
A. Sputtering.....	4
B. Secondary Ion Emission.....	12
III. Theoretical Description of the Ion Bombardment Event.....	18
A. Sputtering Yield Calculations.....	18
1. Transport Theories.....	18
2. Molecular Dynamics Calculations.....	22
B. Ionization of the Ejected Atoms.....	31
IV. Structure-Sensitive Factors.....	50
A. Yields.....	51
B. Angular Distributions of Atoms Ejected From Clean Single Crystals.....	53
C. Angular Distributions for Adsorbate-Covered Single Crystals.....	55
V. Cluster Formation Processes.....	60
A. Theoretical Aspects of Molecular Ejection.....	60
B. Molecular Clusters and the Ionization Process.....	74
VI. Molecular SIMS.....	78
A. A Model Study with Benzene.....	80
B. Matrix Effects.....	83
C. Alkali Halides.....	84
D. Surface Reactions.....	84
E. Molecular SIMS and Related Methods.....	84
Acknowledgement.....	87
References.....	88

Due to the length of this article, the remainder will be sent upon request.

N. Winograd
12/15/81

Received
 Date _____
 By _____
 District _____
 Special _____
 A

TECHNICAL REPORT DISTRIBUTION LIST, GEN

	<u>No.</u> <u>Copies</u>		<u>No.</u> <u>Copies</u>
Office of Naval Research Attn: Code 472 300 North Quincy Street Arlington, Virginia 22217	2	U.S. Army Research Office Attn: CRD-AA-IP P.O. Box 1211 Research Triangle Park, N.C. 27709	1
ONR Western Regional Office Attn: Dr. R. J. Marcus 1030 East Green Street Pasadena, California 91106	1	Naval Ocean Systems Center Attn: Mr. Joe McCartney San Diego, California 92132	1
ONR Eastern Regional Office Attn: Dr. L. E. Peebles Building 114, Section D 666 Summer Street Boston, Massachusetts 02210	1	Naval Weapons Center Attn: Dr. A. B. Amstar, Chemistry Division China Lake, California 93555	1
Director, Naval Research Laboratory Attn: Code 6100 Washington, D.C. 20390	1	Naval Civil Engineering Laboratory Attn: Dr. R. W. Drisko Port Hueneme, California 93401	1
The Assistant Secretary of the Navy (RE&S) Department of the Navy Room 4E736, Pentagon Washington, D.C. 20350	1	Department of Physics & Chemistry Naval Postgraduate School Monterey, California 93940	1
Commander, Naval Air Systems Command Attn: Code 3100 (H. Rosenwasser) Department of the Navy Washington, D.C. 20360	1	Scientific Advisor Commandant of the Marine Corps (Code RD-1) Washington, D.C. 20380	1
Defense Technical Information Center Building 5, Cameron Station Alexandria, Virginia 22314	12	Naval Ship Research and Development Center Attn: Dr. G. Bosmajian, Applied Chemistry Division Annapolis, Maryland 21401	1
Dr. Fred Saalfeld Chemistry Division, Code 6100 Naval Research Laboratory Washington, D.C. 20375	1	Naval Ocean Systems Center Attn: Dr. S. Yamamoto, Marine Sciences Division San Diego, California 91232	1
		Mr. John Boyle Materials Branch Naval Ship Engineering Center Philadelphia, Pennsylvania 19112	1

TECHNICAL REPORT DISTRIBUTION LIST, 056

	<u>No. Copies</u>		<u>No. Copies</u>
Dr. G. A. Somorjai Department of Chemistry University of California Berkeley, California 94720	1	Dr. C. P. Flynn Department of Physics University of Illinois Urbana, Illinois 61801	1
Dr. L. N. Jarvis Surface Chemistry Division 4555 Overlook Avenue, S.W. Washington, D.C. 20375	1	Dr. W. Kohn Department of Physics University of California (San Diego) LaJolla, California 92037	1
Dr. J. B. Hudson Materials Division Rensselaer Polytechnic Institute Troy, New York 12181	1	Dr. R. L. Park Director, Center of Materials Research University of Maryland College Park, Maryland 20742	1
Dr. John T. Yates Surface Chemistry Section National Bureau of Standards Department of Commerce Washington, D.C. 20234	1	Dr. W. T. Peria Electrical Engineering Department University of Minnesota Minneapolis, Minnesota 55455	1
Dr. Theodore E. Madey Surface Chemistry Section Department of Commerce National Bureau of Standards Washington, D.C. 20234	1	Dr. Chia-wei Woo Department of Physics Northwestern University Evanston, Illinois 60201	1
Dr. J. M. White Department of Chemistry University of Texas Austin, Texas 78712	1	Dr. D. C. Mattis Polytechnic Institute of New York 333 Jay Street Brooklyn, New York 11201	1
Dr. Keith H. Johnson Department of Metallurgy and Materials Science Massachusetts Institute of Technology Cambridge, Massachusetts 02139	1	Dr. Robert M. Hexter Department of Chemistry University of Minnesota Minneapolis, Minnesota 55455	1
Dr. J. E. Demuth IBM Corporation Thomas J. Watson Research Center P.O. Box 218 Yorktown Heights, New York 10598	1	Dr. R. P. Van Duyne Chemistry Department Northwestern University Evanston, Illinois 60201	1

TECHNICAL REPORT DISTRIBUTION LIST, 056

	<u>No. Copies</u>		<u>No. Copies</u>
Dr. S. Sibener Department of Chemistry James Franck Institute 5640 Ellis Avenue Chicago, Illinois 60637	1	Dr. Martin Fleischmann Department of Chemistry Southampton University Southampton SO9 5NH Hampshire, England	1
Dr. M. G. Lagally Department of Metallurgical and Mining Engineering University of Wisconsin Madison, Wisconsin 53706	1	Dr. J. Osteryoung Chemistry Department State University of New York at Buffalo Buffalo, New York 14214	1
Dr. Robert Gomer Department of Chemistry James Franck Institute 5640 Ellis Avenue Chicago, Illinois 60637	1	Dr. G. Rubloff I.B.M. Thomas J. Watson Research Center P. O. Box 218 Yorktown Heights, New York 10598	1
Dr. R. G. Wallis Department of Physics University of California, Irvine Irvine, California 92664	1	Dr. J. A. Gardner Department of Physics Oregon State University Corvallis, Oregon 97331	1
Dr. D. Ramaker Chemistry Department George Washington University Washington, D.C. 20052	1	Dr. G. D. Stein Mechanical Engineering Department Northwestern University Evanston, Illinois 60201	1
Dr. P. Hansma Chemistry Department University of California, Santa Barbara Santa Barbara, California 93106	1	Dr. K. G. Spears Chemistry Department Northwestern University Evanston, Illinois 60201	1
Dr. P. Hendra Chemistry Department Southampton University England SO9JNH	1	Dr. R. W. Plummer University of Pennsylvania Department of Physics Philadelphia, Pennsylvania 19104	1
Professor P. Skell Chemistry Department Pennsylvania State University University Park, Pennsylvania 16802	1	Dr. E. Yeager Department of Chemistry Case Western Reserve University Cleveland, Ohio 44106	2
Dr. J. C. Hemminger Chemistry Department University of California, Irvine Irvine, California 92717	1	Professor D. Hercules University of Pittsburgh Chemistry Department Pittsburgh, Pennsylvania 15260	1

TECHNICAL REPORT DISTRIBUTION LIST, 056

No.
Copies

~~Professor N. Winograd~~
The Pennsylvania State University
Department of Chemistry
University Park, Pennsylvania 16802 1

Professor T. F. George
The University of Rochester
Chemistry Department
Rochester, New York 14627 1

Professor Dudley R. Herschbach
Harvard College
Office for Research Contracts
1350 Massachusetts Avenue
Cambridge, Massachusetts 02138 1

Professor Horia Metiu
University of California,
Santa Barbara
Chemistry Department
Santa Barbara, California 93106 1

Professor A. Steckl
Rensselaer Polytechnic Institute
Department of Electrical and
Systems Engineering
Integrated Circuits Laboratories
Troy, New York 12181 1

Professor R. D. Archer
University of Massachusetts
Chemistry Department
Amherst, Massachusetts 01003 1

Dr. A. C. Pastor
Hughes Research Laboratories
3011 Malibu Canyon Road
Malibu, California 90265 1

Characterization of Solids and Surfaces Using Ion Beams and Mass Spectrometry

Nicholas Winograd

Department of Chemistry
The Pennsylvania State University
University Park, Pennsylvania 16802

Table of Contents

	<u>Page</u>
I. Introduction.....	1
II. Ion Bombardment Methods.....	4
A. Sputtering.....	4
B. Secondary Ion Emission.....	12
III. Theoretical Description of the Ion Bombardment Event.....	18
A. Sputtering Yield Calculations.....	18
1. Transport Theories.....	18
2. Molecular Dynamics Calculations.....	22
B. Ionization of the Ejected Atoms.....	31
IV. Structure-Sensitive Factors.....	50
A. Yields.....	51
B. Angular Distributions of Atoms Ejected From Clean Single Crystals.....	53
C. Angular Distributions for Adsorbate-Covered Single Crystals.....	55
V. Cluster Formation Processes.....	60
A. Theoretical Aspects of Molecular Ejection.....	60
B. Molecular Clusters and the Ionization Process.....	74
VI. Molecular SIMS.....	78
A. A Model Study with Benzene.....	80
B. Matrix Effects.....	83
C. Alkali Halides.....	84
D. Surface Reactions.....	84
E. Molecular SIMS and Related Methods.....	84
Acknowledgement.....	87
References.....	88

I. Introduction

In this review, we will examine the possibility of utilizing energetic ion beams as tools to characterize the chemistry and structure of solids and surfaces. This approach may appear somewhat unusual to most spectroscopists who are generally concerned with the quantum mechanical interaction of electromagnetic radiation with matter. But, there have been a number of developments that have surfaced over the last few years which have attracted our attention to this particular field and which merit close consideration.

The idea behind the experiment of interest is illustrated in Figure 1. We begin with a

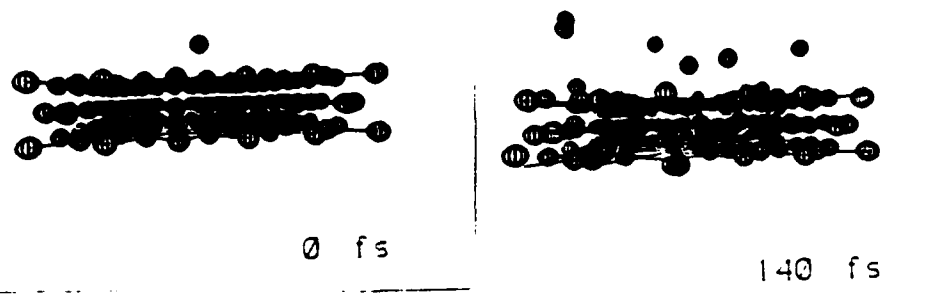


Figure 1 - Positions of the atoms. (a) Before the primary ion (the lone sphere above the solid) has struck. (b) Consequences of a single ion impact. The two atoms ejecting to the left form a dimer. For graphical clarity, only a selected group of atoms is shown, and their size is arbitrarily drawn for best graphical clarity.

single crystal substrate represented by an ordered array of spheres containing, in this case, three layers. The atom above the crystal in Figure 1a represents the incident particle whose kinetic energy is generally between a few hundred and a few thousand electron volts. After the collision, the atoms in the crystal begin to move in various directions as the energy of the incident particle is shared between these atoms. In Figure 1b, after less than 10^{-12} s, some particles have ejected into the vacuum and may therefore, in principle, be detected in the laboratory.

The question is - can we learn something about the solid by a detailed analysis of the motion subsequent to the primary bombardment event? The answer and implications of such a question are certainly not obvious. In fact, to illustrate the difficulty it is appropriate to make an analogy to the game of pool. Here, a cue ball is incident upon a triangular array of 15 target spheres placed on an isolated surface. What we would like to know is - suppose a player comes into the room with the pool table and then initiates the action. After all the balls stop moving, he leaves the room and a second observer enters who is asked to reconstruct the original configuration of the balls. He is asked not only to reveal their original structure but also to place the numbered balls in their respective sequence. Thus, was the eight ball originally touching the two ball? If we could do this on an atomic scale, we could obviously learn a great deal about the structure and interaction forces between atoms near the point of impact of the bombarding particle.

This general subject has been important outside of the field of chemistry for nearly a century. The applications appear in such diverse fields as ion implantation, particularly for doping semi-conductors, fusion reactor design and the determination of the effect of wall reactions on plasma temperatures, and astrophysics and the study of the influence of

the solar wind (He^+) on extraterrestrial surfaces. The interest may be focussed on the damage imparted to the solid by the incident particle or to the analysis of the ejected material.

There is a long history to the development of the current state of this field. Before 1970 most of the research was carried out by physicists who really were not concerned with any of the possible chemical implications. Furthermore, most of the experiments were completed under rather ill-defined conditions. Thus, we have chosen not to comprehensively review all published literature but to try to congeal from many fragmentary pieces of data a scenario which should be of interest in the development of new approaches to the chemical and structural analysis of a wide variety of materials.

There are a number of excellent reviews of related topics for those readers interested in filling in the gaps. First, there is a landmark publication by Carter and Colligan (1) which is comprehensive and complete through 1967. Next, there have been several publications that have appeared during the last 5 years which are reprints from major symposia. These include an International Workshop on Inelastic Ion-Surface Collisions held in July of 1976 at Bell Laboratories in Murray Hill, New Jersey (2), the Proceedings of the 8th International Conference on Atomic Collisions in Solids held in August of 1979 in Hamilton, Canada (3), the Second International Conference on SIMS in August of 1979 at Stanford University (4), an International Symposium on Sputtering held in Vienna in April of 1980 (5) and an International Workshop on Inelastic Ion-Surface Collisions held in Feldkirchen-Westerham, Germany in September of 1980 (6). Finally, there are several journals usually not familiar to those outside of the field including Radiation Effects and the Journal of Nuclear Instruments and Methods where a number of relevant articles may be found.

A further point is that we shall ignore completely the ultimate fate of the incident particle. This aspect of the problem, however, also provides complementary information and there are fascinating experiments proceeding along these lines. For example, the techniques of ion scattering spectrometry (6), MeV backscattering (7), and atomic beam diffraction (8) are providing intimate details about the structure of solid surfaces.

The development of this article will proceed along the following path. We will begin by citing a few of the key experiments which influenced most strongly the current direction of the field. Next, we shall review some of the major theoretical developments that have led to the current detailed understanding of what happens during the bombardment event, and finally we will elucidate some of the applications that should be of interest to chemists in their constant search for new types of analysis methods.

II. Ion Bombardment Methods

To characterize the ejection of material from the solid, it is possible to devise experimental techniques to detect both the neutral particles and those that are ionized directly by the surface. Although it is easier to detect small quantities of ejected ions, the neutrals have more interest from a theoretical point of view. In this section, the experimental approaches to characterizing the ejected neutrals and ions will be presented. The emphasis will be placed on the use of single crystal samples since the question of atomic structure is central to this article.

A. Sputtering

As shown in Figure 1 when a keV ion strikes a solid, there is sufficient momentum transferred to the target atoms that considerable nuclear motion is initiated. A fraction of the moving atoms may obtain a sufficient component of momentum oriented into the vacuum that they are able to overcome the surface binding force and eject from the solid. Some of these particles emerge directly as positive or negative ions, while others are ejected as either ground or excited state neutral atoms as illustrated in Figure 2. The emission

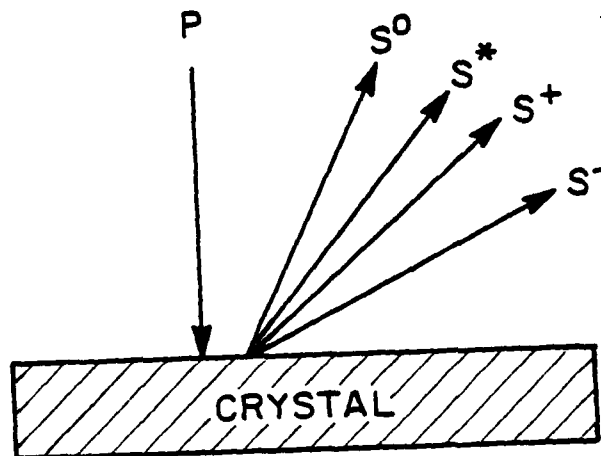


Figure 2 - Schematic representation of the ion bombardment experiment. The primary particle, P, generally is given a few hundred to a few thousand eV of kinetic energy.

process and the associated radiation damage in the solid are often referred to as sputtering, a term left over from the earliest observations of the phenomenon back in the 1850's. These workers were concerned about the erosion of cathodes in gas discharge sources (9). According to a recent review (10), the word "sputtering" intimates a microscopic appreciation for the ejection process since it implies that matter is emitted in discrete blobs from the areas of the surface that are struck by the bombarding ion. In the modern sense, the dictionary definition of the word is "To emit saliva from the mouth in small

particles", hardly a scientific term. It appears, however, that the old terminology is destined to remain with us for some time. Historically, then, the first studies of ion bombarded solids involved the investigation of the sputtered species.

Most ion bombardment studies up until the mid 1960's were spent collecting seemingly unrelated determinations of the sputtering yield as a function of all possible variables. Here the yield, Y , is defined as

$$Y = S/i_0 \quad (1)$$

where S is the number of ejected particles (atoms plus ions) from the target and i_0 is the number of incident ions. Y was found to vary with the angle of incidence of the primary ion, the atomic weights of all involved species, the primary ion energy, the primary ion current and the angle of the ejecting particles (1). The value of Y was nearly independent of temperature at temperature values well-below the melting point of the target (1).

The investigations mainly involved measurement of the weight loss of the target. Other analysis methods included measurement of changes in the resonant frequency of a crystal on which the target is plated (11), noting changes of the target resistance (12) and use of radiotracers (13). Reproducible results were extremely difficult to obtain since vacuums were only $\sim 10^{-6}$ torr and impurities could have a large influence on the results. In addition, the morphology of the sample influenced Y and this property would generally change during the measurement. Nevertheless, there were several key experiments that have influenced present day concepts of ion/solid interactions.

The influence of Y on the surface morphology provided the first clue to the fact that the momentum dissipation of the primary ion was sensitive to the atomic structure. In Figure 3, for example, is shown an etch pattern of a Cu(11,3,1) target and a single crystal

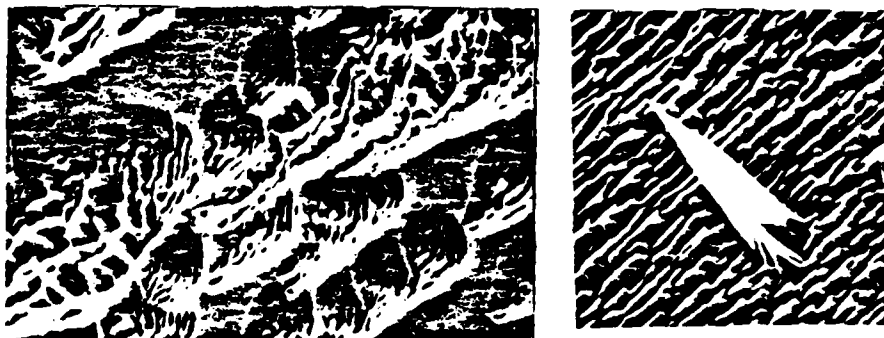


Figure 3 - Electron micrograph of surfaces bombarded by 9 keV Ar⁺.
(a) Cu(11,3,1), magnification 2000x (b) Si crystal,
magnification 5000x. From reference 14.

silicon surface bombarded by 9 keV Ar^+ ions (14). In both cases, the notable feature is one of faceting which, for Cu, seems to emerge from the base of etch pits. The theory that different facets of a polycrystalline surface exhibited different yields was proposed by Wehner some years earlier (15,16). In fact Wehner found preferential etching patterns which reflected the atomic symmetry of the target crystal face. Since these studies pictures of many spectacular surface features have been published, including those of great columns and cones, like those of Figure 3 reminiscent of the surfaces of distant worlds. These changes, however, indicated that the observable could be a function of primary ion dose (dose = ions-sec⁻¹-cm⁻¹ x time). It became apparent, then, that techniques which required the smallest dose would be most desirable.

With improvements in vacuums and primary ion sources, the quality of yield measurements began to improve markedly. Initially, it was found that Y generally increased with the kinetic energy of the primary ion to a maximum value. At even higher kinetic energies, the yield then began to decrease, presumably since the primary ion penetrated too far into the target to cause ejection of surface atoms. Of particular interest was that there is a strong dependence of yield on the orientation of single crystal samples. In Figure 4, for example, is presented the yield vs. primary kinetic energy curve for Ar^+ normally incident on Cu(111), Cu(110), Cu(100) and polycrystalline Cu (17-19). Note that at least above 1 keV Ar^+ ion energy, $Y(111) > Y(100) > Y(110)$ and that the maximum yield can approach 10 ejected Cu atoms per incident Ar^+ ion. This same trend has been reported for Ag (19) and Au (20) indicating the importance of crystallographic effects. Similar variations of yield with angle of incidence have been reported as shown in Figure 5 (21) where the yield minima correspond to open crystallographic directions. We must admit that these results are somewhat surprising, especially in view of the rather strong effects the incident ion may have on the surface morphology as demonstrated in Figures 1 and 3. It would be particularly valuable to repeat these studies where surface damage effects do not occur.

Crystallography, however, clearly is an important factor in sputtering which may be the reason that most workers during the 1960's spent much effort analyzing single crystals. Probably the most spectacular discovery of that era was that of Wehner. Using the very simple discharge tube apparatus shown in Figure 6 (22), he utilized a Hg^+ ion discharge to bombard a Cu crystal and collect the sputtered atoms on a flat plate. An example of the type of pattern that could be collected using this procedure is given in Figure 7 (18,23). The patterns showed clear evidence for large angular anisotropies in the yields which also reflected the symmetry of the atoms in the surface layer. Since these papers, more than 100 studies have appeared in the literature, detailing the effects for a wide variety of crystals under many ion bombardment conditions. These studies have waned in recent years

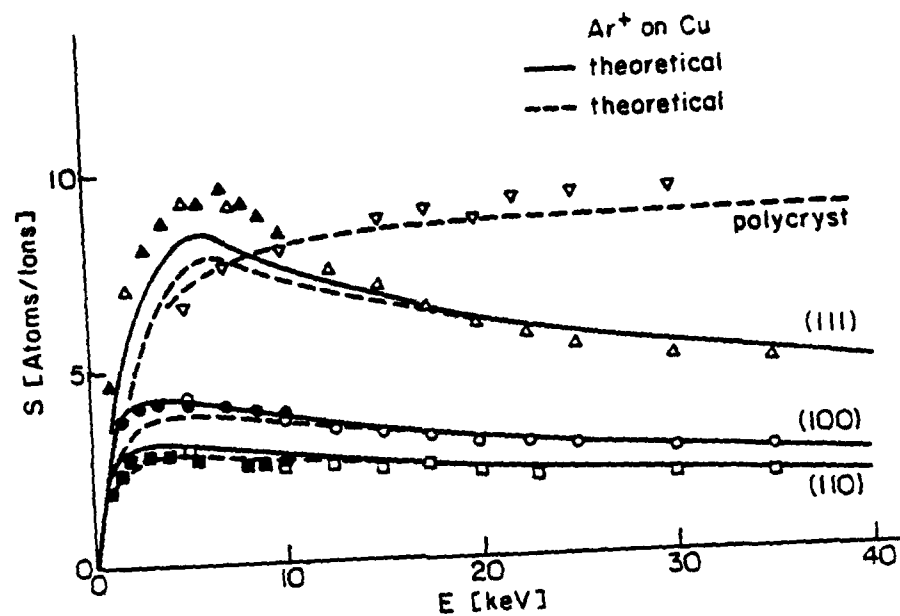


Figure 4 - The sputtering yield as a function of energy for normally incident Ar^+ ions on various crystal faces of copper. The theoretical model is described in reference 16.

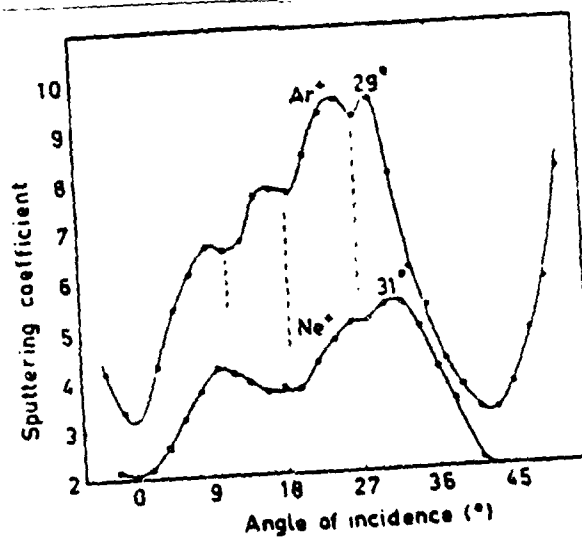


Figure 5 - The sputtering yield for a (001) surface of a copper crystal, which is turned around a [010] direction in the surface. The 20-keV bombarding ions are Ar^+ and Ne^+ , respectively. From reference 20.

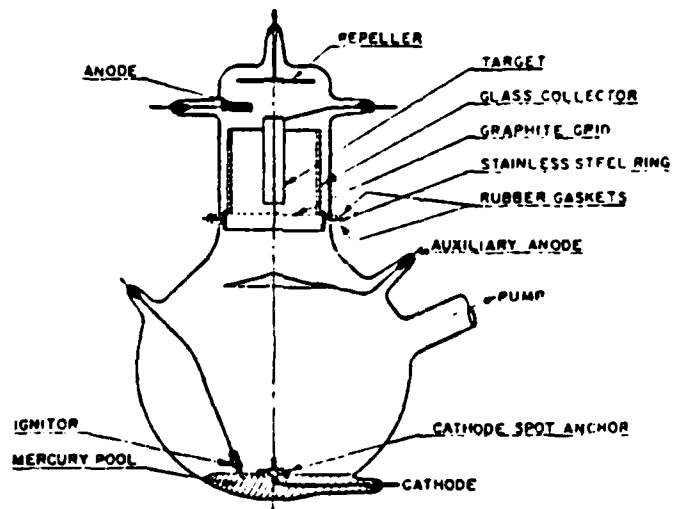


Figure 6 - Discharge tube. From reference 21.

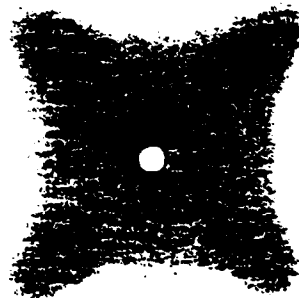


Figure 7 - Angular distributions of atoms ejected from Cu(001) from reference 17.

due to the lack of a cohesive theory to explain the anisotropy and due to the experimental difficulties of maintaining an uncontaminated and undamaged crystal surface.

An improved approach has recently been developed for studying these anisotropies. Specifically, the sputtered material is collected on an aluminum plate and subsequently analyzed using Rutherford backscattering, a highly quantitative and sensitive measurement technique which requires nearly two orders of magnitude smaller primary ion doses than previous methods (24). With this apparatus, it has been found that for gold (111) bombarded by 4 keV Ne^+ that more than 50% of the sputtered material is emitted into the

spots. The shapes of the spots are nearly independent of the projectile mass and energy for energies greater than ~ 4 keV (24). These findings contrast previous assertions that these anisotropies constitute only a minor part of the sputtering process and may therefore be ignored (10).

An additional, important piece of information which provides insight into the sputtering process is the velocity distribution of the ejected atoms. These were first reported by Thompson and Nelson (13) using a time of flight analysis of the atom velocities and later by Stuart and Wehner using a fluorescence method (16). The distributions as shown in Figure 8 are similar for most materials in that the curve is 0 at 0.0 eV, peaks at the fairly low energy of 2-5 eV and then tails off with an energy dependence of somewhere between $1/E$ and $1/E^2$. The total yield, Y , then can be expressed in terms of an energy spectrum where

$$Y = \int_0^{E_m} y(E) dE \quad (2)$$

where $y(E)dE$ is the differential secondary particle yield, and E_m is the maximum energy that any of the ejected particles has attained. The energy distributions are markedly different

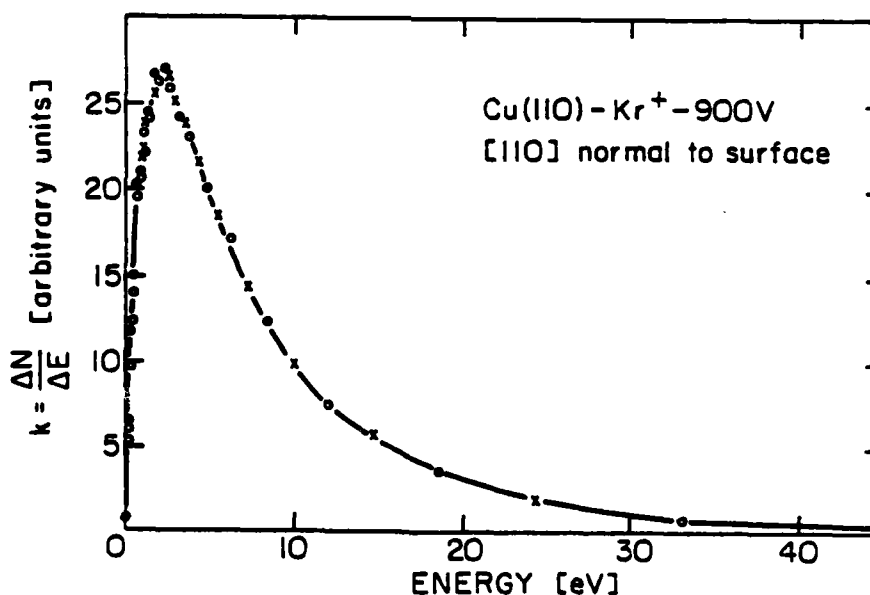


Figure 8 - Energy distribution of atoms ejected in the [110] direction from the (110) surface under bombardment by normally incident Kr ions. From reference 16.

from those expected for thermal evaporation processes where the full width at half maximum of the peak would be Maxwell-Boltzman in shape and considerably smaller.

Although these studies have provided much of the fundamental information that we have regarding the ion bombardment event, the scope of the techniques is severely limited by their ultimate sensitivity and general lack of chemical specificity. A number of approaches have been tested in order to obtain better information from the ejected neutrals. One idea involves the post-ionization of the ejected species either by electron bombardment (25) or by a low energy plasma discharge (26). The ion which is formed is then detectable with single particle detection limits using a mass spectrometer. This concept has been exploited by Konnen et al. (27) who employed a time of flight technique to determine particle velocities, but then utilized an ionization scheme to detect the mass-selected beam. This procedure worked well for alkali metals but did not provide sufficient sensitivity for other particles (28,29). In fact most post-ionization methods are hard pressed to compete with the older sputtering methods based on weight loss analysis. The efficiency of ionization by electrons, for example, is generally only about 10^{-5} . In addition the ionization cross-section is strongly dependent on the particle velocity, a severe difficulty for these experiments because of the broad energy distribution of the ejected particles. And finally, the process of electron bombardment may in itself cause fragmentation of ejected molecular clusters, muddling the picture still further.

The use of a hot maxwellian electron gas maintained by electron cyclotron wave resonance has shown considerable promise as an approach to study the sputtering phenomenon (26). Ionization of neutrals occurs with an efficiency approaching 1%. In addition, sputtered neutral mass spectrometry (SNMS) has been successful in measuring dimer to monomer ratios for a number of different metals. For example, Oechsner found that the Cu_2/Cu ratio from polycrystalline Cu was approximately 10% (30).

Perhaps one of the most promising methods for analysis of the neutral particles is via the use of laser spectroscopy. One such approach involves the excitation of the ejected atom by a laser, followed by the measurement of the doppler-shifted fluorescent intensity (31). Using this approach, very high quality energy distributions can be obtained for sputtered neutrals using incident ion doses small enough to avoid significantly altering the surface. The block diagram for a typical apparatus is shown in Figure 9, with the resulting energy distribution shown in Figure 10 (32). It is likely that with the advent of ultra-high vacuum instrumentation and the evolution of sensitive methods of analysis of the neutrals that very high quality sputtering data from well-defined solid surfaces will soon be available. At the present time, however, it is not possible to perform yield measurements without damaging the crystal surface.

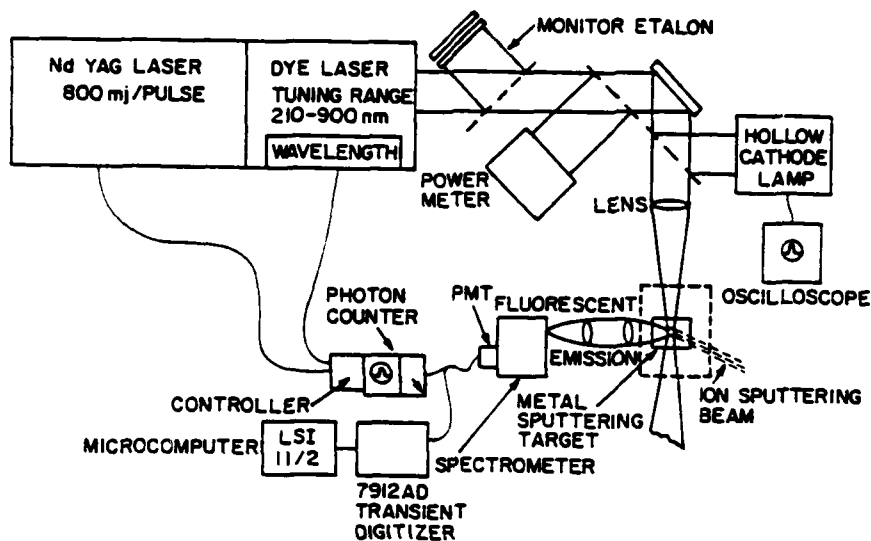


Figure 9 - Diagram of apparatus used in the doppler-shifted laser spectral experiments used to measure the energy distribution of the neutrals. From reference 32.

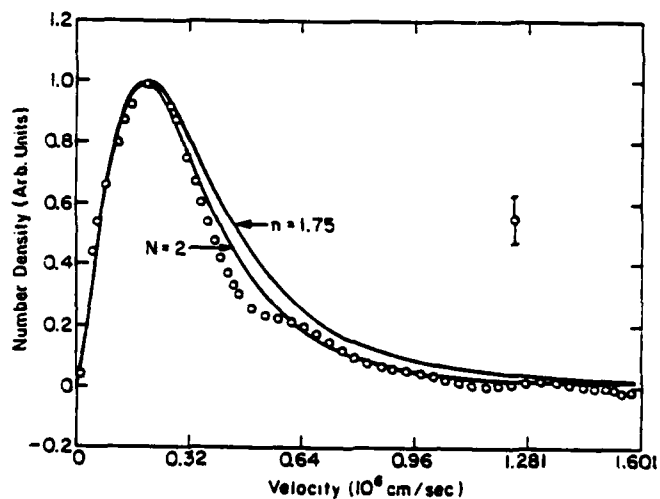


Figure 10 - Number density velocity distribution of neutral ground state zirconium atoms sputtered by normally incident 1.5 keV Kr^+ . The (O) represent deconvoluted data averaged over several runs. The solid curves are obtained from Thompson's equations (13). An average error is displayed in the right-hand corner. From reference 32.

3. Secondary Ion Emission

It has been recognized for more than 50 years (33) that a fraction of the particles ejected from an ion bombarded target are either positive or negative ions. The secondary positive (negative) ion yield $Y^{+(-)}$ is defined as

$$Y^{+} = R^{+} Y \quad (3)$$

where R^{+} is the probability that the ejecting neutral species will leave the solid in an ionized state. A similar expression could be written for negative ions. It is possible that R^{+} is a function of energy so that combining Eq. (2) and (3) we obtain

$$Y^{+} = \int_0^{E_0} R^{+}(E) y(E) dE \quad (4)$$

For many systems, the value of Y^{+} may be large enough to permit detection of very low concentrations of surface species. Much of the early interest in secondary ion emission in fact stemmed from this potential analytical application. Initially, a lot of effort was spent developing the ion microscope (34) and the scanning ion microprobe (35). Here, the secondary ions were directly imaged into a double focussing mass spectrometer and detected with single ion limits. Evaluation of the secondary ion intensity I^{+} [counts/sec] recorded during bombardment of the sample is more complex than for the neutral species as determined by weight loss, but it is easy to see the potential sensitivity of this approach. For this case ignoring angular effects (36)

$$I^{+} = i_0 \gamma_M \beta(M^{+}) T(E_0, R) \int_{E_1}^{E_2} y^{+}(E') dE' \quad (5)$$

where i_0 is the flux of primary ions, γ_M is the isotope abundance of element M, $\beta(M^{+})$ is the detector efficiency which depends on the mass and velocity of the ion (37) and $T(E_0, R)$ is the transmission of the ion optical system which depends upon energy position $E_0 + \Delta E/2$ and width $\Delta E = E_2 - E_1$ of the energy window and the mass resolution of the mass spectrometer. For typical values of $i_0 = 10^{-9}$ amps of Ar^{+} ions spread over 10^{-3} cm^2 ($6 \times 10^{13} \text{ ions-sec}^{-1}\text{-cm}^{-2}$), $\gamma_M \beta T = 10^{-3}$, $E_0 = 10 \text{ eV}$, $\Delta E = 5 \text{ eV}$ and the integral in Eq. 5 equal to approximately 10^{-2} , the $I^{+} = 6 \times 10^8 \text{ counts/sec}$. With a detection limit of $\sim 1 \text{ cps}$, it is clear that measurements in the parts per million (ppm) atomic percent range can be completed. In addition, there is also sufficient sensitivity to detect ions ejected from a very small area. Early development of these secondary ion mass spectrometric (i.e. SIMS) methods, however, was hindered mainly due to the the very high cost of the instrumentation.

There are two additional disadvantages of this approach. First, it turns out to be very difficult to obtain quantitative ion yield measurements. This is due to the difficulty in evaluating ST and to the large variations found in $y^+(E)$ in Eq. 5 (or K^+ in Eq. 3) with the sample matrix. For example, the yield of Ni^+ from Ni is 10^3 times smaller than the yield of Ni^+ from NiO (38) under otherwise identical conditions. To understand these results it is necessary to have a theoretical understanding of the secondary ion formation mechanism. As we shall see in Section III, there are a number of possible approaches to explaining the ionization process, although none have yet proven to be very satisfactory.

A second major problem with SIMS as presented above is that although the primary ion current is small, the primary ion flux is extremely large, typically 10 to 100 $\mu\text{amp}/\text{cm}^2$, or 10^{14} to 10^{16} incident ions- sec^{-1} . If we assume there are roughly 10^{15} atoms- cm^{-2} on a typical metal surface and the sputtering yield, Y , is ~ 1 , then the sample is being eroded away at the rate of 0.1 to 10 monolayers- sec^{-1} . The magnitude of the sample damage is clearly quite large and the prospect for performing a chemical analysis on a molecular system would appear dim.

During the late 1960's, this problem was ingeniously overcome by Benninghoven and his co-workers (39,40) who simply proposed to expand the size of the primary ion beam and reduce the total dose of ions to less than $\sim 10^{13}$ atoms- cm^{-2} . By using incident currents of $\sim 10^{-9}$ to 10^{-10} amps/cm^2 , then, he could study the chemical nature of a surface for minutes without altering the surface composition. The erosion rate was effectively reduced to 10^{-5} - 10^{-6} monolayer- sec^{-1} . In addition, since a wide area was being imaged into the mass spectrometer, he was able to considerably enhance sensitivity by utilizing a quadrupole mass filter instead of a magnetic sector (41). This implementation was also important since the energy distribution of the ejected species extends over quite a range as shown in Figures 8 and 10 and quadrupoles are generally insensitive to ion energy. The cost, not incidentally, is considerably lower and the equipment can be made compatible with ultra-high vacuum (UHV or 10^{-10} torr) conditions. A typical experimental set-up (42) is shown in Figure 11.

Thus, there have evolved several approaches to characterizing the phenomenon of secondary ion emission. There is the small beam, ion microprobe SIMS method that provides microanalysis and high sensitivity but rapidly erodes the sample surface. At the other extreme, there is the large beam, low dose SIMS method that minimizes sample damage and allows possible surface chemical studies. The former is often referred to as dynamic SIMS and the latter as static SIMS (43). The application of ion beam techniques to depth profiling using mass spectrometric detection where both the beam size and primary ion current are large is also referred to as dynamic SIMS. Finally, for the case where the beam

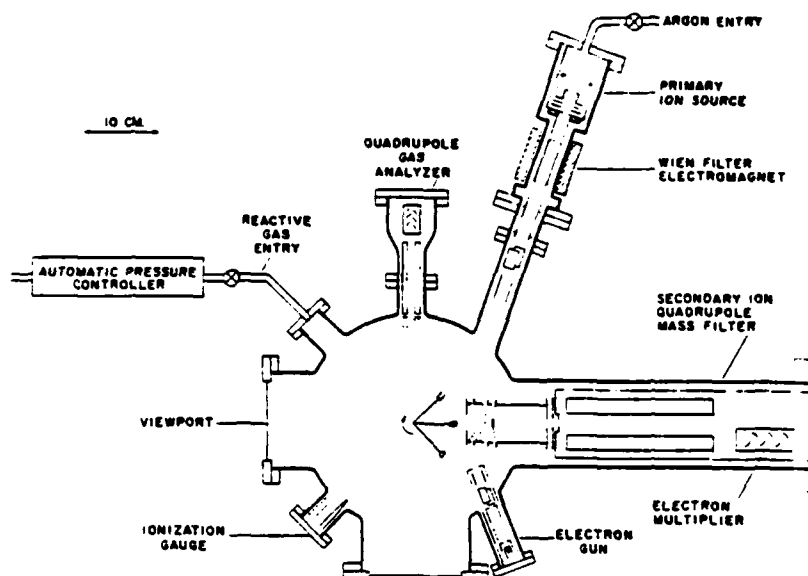


Figure 11 - A general view of a secondary ion mass spectrometer system.
From reference 42.

dose is somewhat larger than necessary to maintain static conditions, the term quasi-dynamic SIMS has been applied. It would seem that this approach minimizes the information content of the signal.

We have learned a great deal about the sputtering process by analyzing the mass, energy and ejection angle of the secondary ions. Of particular interest is that in addition to ejected monatomic ions, there are also high yields of molecular cluster ions that are found to eject. These were first observed by Honig (44) from Ag bombarded by 200-400 keV Kr^+ and Xe^+ ions and later from semiconductors and insulators, graphite (45) and tungsten (46). For the case of tungsten, as shown in Figure 12, clusters containing up to 12 atoms are visible. Although many of the variables which effect the yields of cluster ions have been investigated, the results of the studies have not provided much insight into how the process occurs. An exception is the energy distribution of the dimer ions relative to the monomer ions. As shown in Figure 13 for niobium, the energy distribution of the dimers is more strongly peaked toward lower values of the kinetic energy (47). Similar observations of the energy distribution by Konnen et al. for ejection of neutral K_2 (48) led the workers to conclude that the dimers were formed by a recombination of ejecting monomers above the solid. The presence of molecular cluster ions also was recognized to provide potentially more information about the chemistry of the solid. Their analysis was immediately exploited in the ion microprobe (49). The possibility that these species formed after considerable

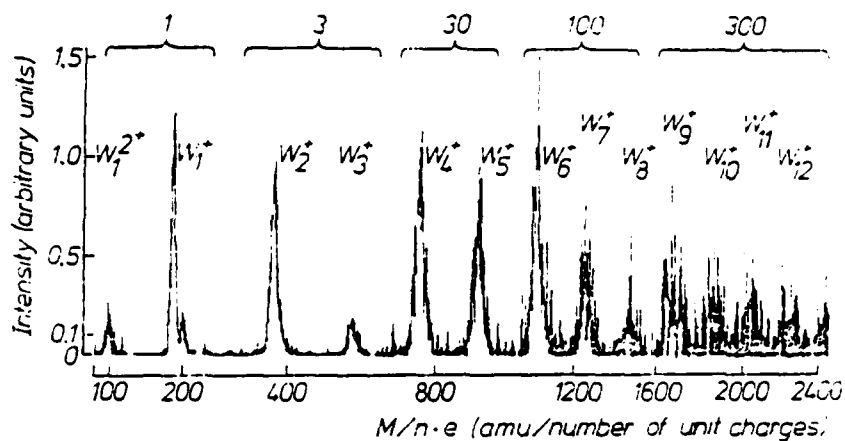


Figure 12 - Mass spectrum of tungsten clusters sputtered by 150 keV xenon ions. The energy of the secondary particles recorded is 30 eV, the energy width 0.83 eV. The numbers above the brackets give the ordinate amplification. From reference 46.

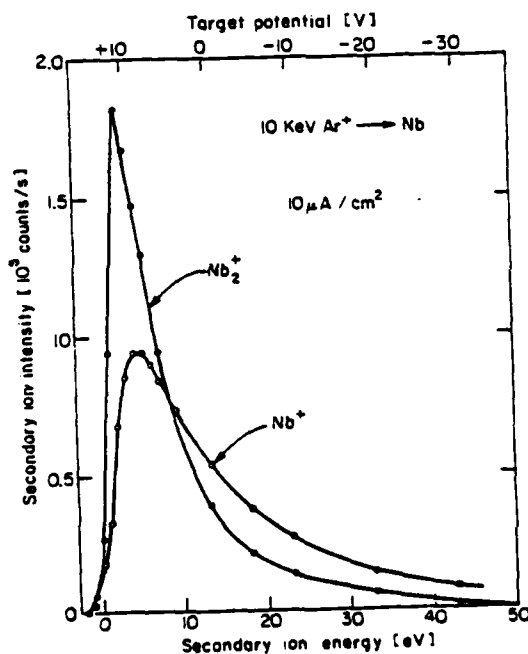


Figure 13 - Secondary ion spectra of Nb^+ and Nb_2^+ , not corrected for changes in emittance of the secondary ion source.

rearrangement and that the primary ion induced considerable structural damage in the sample loomed as major factors mitigating against the dynamic SIMS methods as viable structural characterization tools.

The analysis of clusters using static SIMS at least removes the ambiguities introduced to the sample by the primary beam and a number of workers have now attempted to exploit this fact. Benninghoven (43) first proposed that for a number of different metals exposed to oxygen, that observed clusters of the type $M_mO_n^{\pm}$ were formed from contiguous atoms in the solid and that the solid structure could therefore be reconstructed by an appropriate analysis of the cluster ion intensities. This idea was further reinforced by the work of Buhl and Preisinger (50) who studied ZnS crystals and found mainly polyatomic ions such as ZnS^+ , ZnS^- , Zn_2S^+ and ZnS_2^- . Other polyatomic ions such as Zn_2^+ or S_2^- which were not originally present in the crystal, were observed only in very low intensities. Meanwhile, it became clear that static SIMS could become a useful tool for the detection of many non-volatile organic and inorganic molecules. Benninghoven first showed that when a thin film of an amino acid on a silver foil was bombarded with Ar^+ ions that a cluster ion equal to the molecular weight of the organic compound with a proton attached was ejected from the solid intact (51). Since that discovery many groups have exploited this observation and now such delicate molecules as proteins with molecular weight above 2000 amu can be observed.

The generality of this assessment has been questioned both theoretically and experimentally. For example, Rabalais and co-workers found that CsCl diluted into KCl still produced significant numbers of Cs_2^+ cluster ions and that recombination of ejecting monomers could occur over several hundred angstroms (52). Thus, it appears that under certain circumstances, rearrangement is observed but in others, the clusters are ejected from the sample intact. We shall see in later sections how these observations can be collected together to develop a more unified theory of the cluster emission process.

Of further interest was the proposal that static SIMS could be utilized to characterize monolayers formed during chemisorption of small molecules onto solid surfaces. For example, Benninghoven studied the reaction of O_2 with a clean polycrystalline vanadium surface at room temperature (43). As shown in Figure 14, as the surface becomes oxidized a number of metal-oxygen clusters begin to appear. At high exposure (100L O_2 where 1L = 1 Langmuir = 10^{-6} torr-sec), the SIMS spectrum is similar to that found for V_2O_5 , indicating the formation of an oxide layer. The ion yield fluctuations at low coverage are more difficult to understand, but it was felt that this behavior was characteristic of a chemisorbed oxygen layer.

Further possibilities for the study of monolayers were put forth by Barber and Vickerman and co-workers who studied chemisorption of CO on clean polycrystalline V1

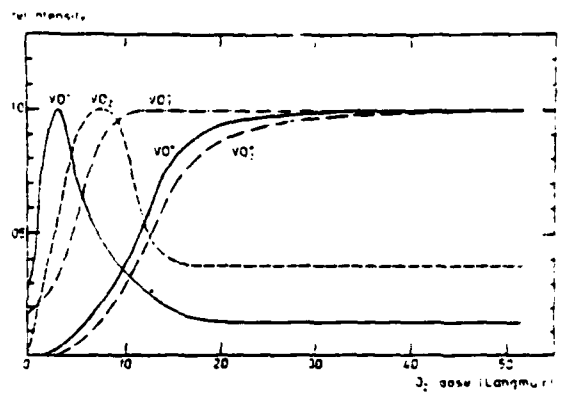


Figure 14 - Change of secondary ion emission during O_2 exposure of a clean vanadium surface. From reference 43.

surfaces (53). They found cluster ions of the type Ni_2^+ , $NiCO^+$, and Ni_2CO^+ but none of the type NiC^+ , NiO^+ , Ni_2C^+ or Ni_2O^+ , indicating that CO adsorbs in a molecular state on Ni. Further, by comparison to vibrational spectra for this system they were able to make a correlation between the Ni_2CO^+ ion and bridge bonded CO, and the $NiCO^+$ ion and linear bonded CO. Their rationale for this observation was that the molecular cluster was ejected as a fragment of the surface without rearrangement as schematically shown in Figure 15. These

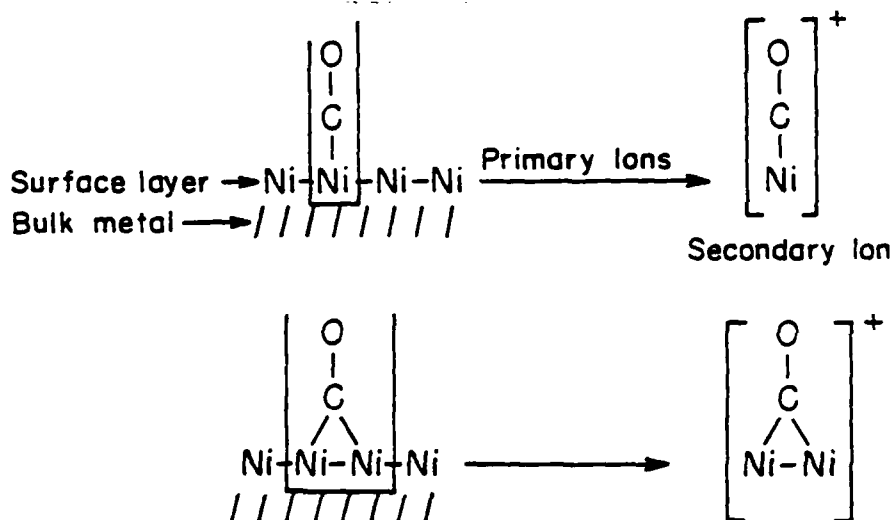


Figure 15 - Surface processes which would give rise to the appearance of $NiCO^+$ and Ni_2CO^+ . From reference 53.

workers made similar conclusions with the adsorption of ethylene on Ni where, both $Ni_2C_2H_4^+$ and $NiC_2H_4^+$ ions were observed in the SIMS spectrum (54). Although the interpretation of many of the above results has been questioned in recent years, there is no doubt that the static SIMS approach coupled with the study of the cluster ions offers a unique method of

surface analysis. To further the interpretation of secondary ion yields, however, we must move to expand our theoretical understanding of the ion impact event.

III. Theoretical Descriptions of the Ion Bombardment Event

At this point in the discussion, it is clear that many consequences of the primary ion impact can be observed experimentally. For example, we have given examples where measurements of the sputtering yield as a function of ejection angle, secondary particle energy and mass for both neutral atoms and secondary ions have been reported. To fully appreciate the significance of these results and to effectively interpret the fascinating SIMS spectra from monolayers, a detailed theoretical treatment is clearly required. There are essentially two aspects to this problem. First, we must be able to determine how the nuclear positions of the atoms or molecules in the sample change with time in response to the impact of the primary ion. Secondly, we must have a quantitative description of the ionization processes which cause certain species to leave the sample surface as ions. In this section, we shall briefly review some of the existing approaches to solving these two problems but will place perhaps undue emphasis on the models preferred by the author.

A. Sputtering Yield Calculations

There are basically two approaches to calculating the energy dissipation of the primary ion. The first, and most widely used, utilizes a statistical model to solve the transport equations for the momentum deposition. This approach allows the yield to be expressed in terms of a simple formula which can be easily used by experimentalists. The second approach receiving considerable attention is to model the impact more explicitly using classical trajectory methods to follow the motion of the relevant particles. This method usually requires a large computer and generally does not provide simple answers.

In general, there are a series of events which must be described following the impact of the primary ion. First, the incoming ion penetrates the solid after striking a target atom. This atom then attains considerable momentum in the direction away from the surface and collides with neighboring atoms producing secondary displacements. Some of these recoil atoms have the possibility of being scattered back toward the surface with sufficient kinetic energy to escape from the sample. There will also be many recoil atoms moving inside the solid, slowing down only as they experience more and more collisions. The primary ion and the target atom may either come to rest inside the solid (implantation) or be ejected themselves. Thus, the sputtering process is a complex event involving multiple atomic collisions (or cascade) initiated by the primary ion.

1. Transport Theories

There have been a number of attempts to derive analytical expressions which predict various properties of the sputtering phenomenon. The most widely used are those of Sigmund

(55-57) whose yield formula are ubiquitous throughout the sputtering literature and of Thompson (58) who has provided a relationship for the yield as a function of secondary particle velocity. In both of these approaches, the initial assumption is that each target atom generates one secondary collision cascade in which energy is shared by a series of collisions. Next, it is assumed that the collisions themselves occur only between two atoms at a time. These approximations have a number of important consequences. First, any electronic energy loss processes are ignored. This is probably a realistic approximation for metals bombarded at less than 50 keV by heavy ions, although for insulators such as alkali halides (59), coulombic interactions may contribute to sputtering. For elastic collisions, the assumption that each collision sequence can be treated separately restricts application of the theory to the region of linear collision cascades (10,55). As shown in Figure 16a, this condition applies only when a small fraction of all atoms within a certain volume are in motion. When more than one cascade is initiated by the primary ion, as shown in Figure 16b, or when a large fraction of the atoms near the impact point are moving, the approach begins to breakdown. This region is often referred to as a dense cascade or a spike. One final consequence is that the binary collision approximation (BCA) should only apply to collisions which exceed several hundred eV. For example, in Figure 16a, the sizes

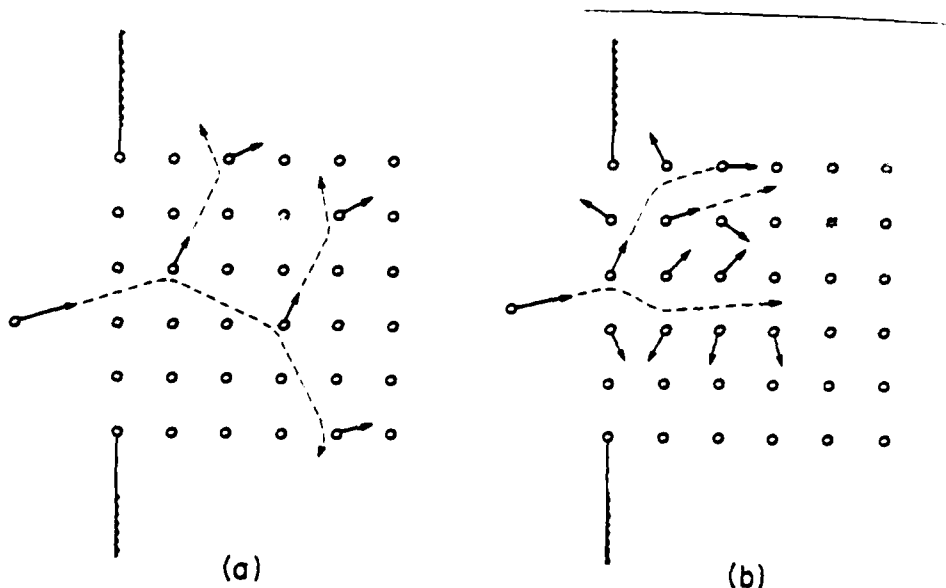


Figure 16 - (a) Linear collision cascade. The structure is preserved, and a small fraction of the atoms is in motion.
(b) Dense cascade (spike). The structure is destroyed locally. All atoms within the spike volume are in motion.
From reference 10.

of the atoms are drawn such that it is impossible for more than two atoms to be interacting simultaneously. If the atomic radii had been drawn such that adjacent atoms nearly touched, as in the case for collision energies below ~ 10 eV, even binary collisions are indeed improbable. It is disturbing that most of the collisions that lead to the ejection of atoms in the solid are those whose energy is below 10 eV as illustrated by the secondary particle energy distributions given in Figures 8 and 10.

In the Sigmund theory, the solid is approximated by an amorphous array of atoms that interact with differential cross sections developed for calculations aimed toward predicting the range of energetic atoms in solids (55). The nuclear stopping cross section $S_n(E)$, can be evaluated from these quantities. The flow of energy through the cascade is then determined using the Boltzmann transport equation. The sputtering yield is evaluated from the flux of particles crossing an imaginary plane at a point in the solid where the target atom is given its initial energy. To include the effect of the surface, it is assumed that the atom must surmount a potential barrier, U , acting on the perpendicular component of the velocity. This potential will act to keep slow moving particles from escaping the barrier and will deflect the faster moving ejecting particles away from the surface normal. This correction is termed the planar surface binding model (55,56). If the collision cascade is restricted to the linear regime by utilizing bombardment energies below a few keV and by utilizing light ion and target masses, the equation for the sputtering yield becomes

$$S = \frac{C S_n(E)}{U} \quad (6)$$

where C is a constant for a given primary ion and energy and target material. The simplicity of this result - that the sputtering yield is proportional to the nuclear stopping power of the solid and inversely proportional to the surface binding energy - accounts, in part, for the popularity of the Sigmund theory. In fact, it has been rather successfully applied in a number of instances as has been reviewed (60). The direct correlation between the stopping power and the yield is particularly striking as is illustrated in Figure 17 for Ar^+ on Cu (56,61). The relationship between yield and surface binding energy (or sublimation energy of the solid) has been used to explain differential sputtering (62) and variations in sputtering yield across the periodic table (55,63). The theory has also been applied to situations where it should not work, probably since it has been the only real theoretical approach available to experimentalists.

A similar theoretical model has been developed by Thompson to explain the energy distribution of ejected atoms (58). His model develops an expression for the flux of atoms inside the solid crossing any internal surface plane. For an ejecting particle of kinetic

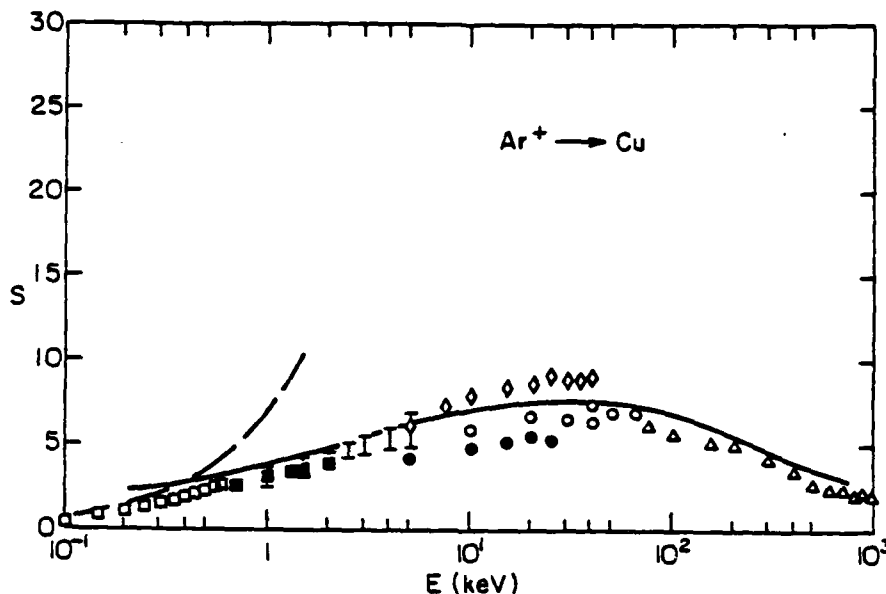


Figure 17 - Sputtering yield as a function of the primary ion energy. The lines are calculated yields from $S_n(E)$ while the points are experiment curves taken from various groups. From references 55 and 56.

energy E , this flux is given as

$$\Phi(E)d\Omega dE = [C'E \cos \theta / (E+U)^{n+1}] \cdot (2\pi \sin \theta) d\theta dE \quad (7)$$

where $\Phi(E)$ is the flux density energy distribution with units of number per unit area per unit time per unit energy. The solid angle $d\Omega = \sin \theta d\theta d\phi = 2\pi \sin \theta d\theta$; $d\phi$ is the azimuthal angle about which the flux is assumed to be isotropic. According to Thompson (58), $n=2$ and C' is a constant for a given primary ion, energy and target material. The appearance of U in Equation 7 is a consequence of the incorporation of the planar surface binding model in the theoretical development. For $E \gg U$, the energy distribution should tail off as E^{-2} . The most probable energy should occur at approximately $U/2$. There have been many experiments aimed toward testing this equation. Probably the most reliable data so far are produced from the laser induced fluorescence experiments on sputtered uranium and zirconium as shown in Figure 10 (64,65). In this case, the value of n in Equation 7 was found to be between 1.75 and 2.0 with $U = 5.2$ eV. The development of the Thompson theory was a major advance in our understanding of sputtering and stood to elucidate the differences between sputtering and simple evaporation. In the latter case, the energy distribution should appear to be Maxwell-Boltzman like in shape.

Although both of these theories were helpful, they were not well-suited to studying crystalline solids and angular anisotropies. They were forced to utilize the BCA and to employ oversimplified interaction potentials to obtain analytical results. It was not possible to explain the factors that influence cluster formation except by a clever analysis of the energy distribution formula (66-68). The theories have been no help in understanding the basic phenomena in SIMS.

2. Molecular Dynamics Calculations

Many of these difficulties can be overcome by utilizing a molecular dynamics calculation on a large ensemble of atoms to compute actual nuclear positions as they change in time subsequent to the primary ion event. Classical dynamics calculations have, of course, been very successful in explaining trajectories in atom-diatom scattering (69), properties of liquids (70) and even the solvation of large molecules like dipeptides (71). For describing the sputtering process this approach has the distinct advantage of utilizing many fewer approximations than required for the statistical theories. On the other hand, no simple equation falls out of the calculations, although important concepts may emerge from the resulting numbers. The calculations often prove very useful in testing the validity of possible analytical theories. In general, these calculations require considerable computer time. With the recent surge in computer efficiency, it would appear this is becoming less of a difficulty.

The first efforts at developing the molecular dynamics procedures were undertaken by Vineyard and co-workers during the early 1960's (72-74). These workers constructed a model microcrystallite consisting of several hundred atoms. A two-body central interatomic potential was used to describe the interaction between each pair of atoms as energy was dumped into the system. The lengthy time required for the computation restricted the application to mechanistic studies of how atoms moved in the solid and could not be compared directly to experiment. Subsequently, Harrison (75,76) was able to perform a number of more lengthy calculations for Ar^+ ions bombarding a Cu single crystal. Yields and angular distributions could be calculated that were not too far away from the experimental results. Harrison was conclusively able to show, for example, that Wehner's spot patterns were due mainly to structural effects of the top atomic layer of the metal (77), rather than from focussed collisions from deep within the solid as had been previously believed (78). Similar mechanistic studies to determine the types of scattering events observed in metals were also undertaken by Jackson (79,80).

To shorten the required computer time, Robinson and co-workers developed a model that incorporated the BCA, the same approximation as that implemented in the energy transport theory (81,82). With this approximation, these workers were able to follow a series of

collisions within the cascade by only calculating the energy transferred during each collision. The computer time was reduced by many orders of magnitude which allowed direct comparison to a number of experimental yield measurements. Although this type of calculation is well-suited to modeling keV ion scattering from solids where the BCA is applicable (83), there are serious questions as we have mentioned earlier, about the validity of using it in sputtering calculations. Robinson has recently recognized this difficulty and incorporated an adjustable parameter into his computer code which accounts for multiple collisions (84). The latest attempts to compare yields and energy distributions to experimental values of Ar^+ ions on amorphous Cu have been reasonably successful (85). In this work, the authors also incorporated both the planar surface binding model and isotropic surface binding model into their calculation. In the latter case, the ejecting particle losses energy U regardless of its ejecting direction. It is not clear yet which, if either, of these two approaches to describing the atomic trajectory as it crosses the surface is best. The calculated yields are higher by about 30% using isotropic binding, but since the value chosen for U is somewhat arbitrary, it would appear this is a meaningless difference. The angular distributions calculated for the two surface binding models should be quite different since a bending of the ejecting atom away from the surface normal occurs only for the case of the planar binding model. Unfortunately, detailed comparisons to experiment have not yet been successful in distinguishing between the two approaches. Other groups have developed similar models using the BCA (86-89), although none has been successful in explaining most sputtering experiments.

The advent of the present day computer has allowed Vineyard's original ideas to be exploited to a much greater extent. During the remainder of this chapter we shall focus on these calculations since they have been remarkably successful at predicting a wide range of experimental observables found for the sputtering of neutral atoms. In addition, there are some real possibilities for coupling these types of calculations which describe the nuclear motion of the atoms to those which describe the electronic motion as we shall see shortly.

The computation of classical trajectories using the molecular dynamics procedure rests on Newton's equation of motion. For a particle i of mass m_i , the equation of motion is

$$m_i \ddot{\vec{r}}_i = \vec{F}_i \quad (8)$$

where \vec{r}_i is the position vector, $\ddot{\vec{r}}_i$ is the acceleration and \vec{F}_i the force. For N particles there will be $3N$ coupled second order differential equations that need to be solved.

Computationally, it is more convenient to utilize Hamilton's form of the equations of motion as

$$m_i \dot{\vec{v}}_i = \vec{F}_i \quad (9)$$

$$\vec{F}_i = -\vec{\nabla}_i \quad (10)$$

where \vec{v}_1 is the particle's velocity, since there are now 6N coupled first order differential equations. These equations provide the position and the time dependence of the velocity and are easier to solve than the second order equations. For an arbitrary value of \vec{F}_1 the atomic motion can be determined using a finite difference algorithm and an incremental time step Δt (90). For example, the average force between t and $t+\Delta t$ is

$$\langle \vec{F}_1 \rangle = 1/2 [\vec{F}_1(\vec{r}_1^*(t+\Delta t) + \vec{F}_1(\vec{r}_1(t))] \quad (11)$$

where \vec{r}_1^* is the predicted position at $t+\Delta t$ and is given by

$$\vec{r}_1^*(t+\Delta t) = \vec{r}_1(t) + \vec{v}_1(t)\Delta t + \vec{F}_1(\vec{r}_1(t))\Delta t^2/2m_1 \quad (12)$$

Once $\langle \vec{F}_1 \rangle$ is known, the corrected positions and velocities at $t+\Delta t$ are then

$$\vec{r}_1(t+\Delta t) = \vec{r}_1(t) + \vec{v}_1(t)\Delta t + \langle \vec{F}_1 \rangle \Delta t^2/2m_1 \quad (13)$$

$$\text{and } \vec{v}_1(t+\Delta t) = \vec{v}_1(t) + \langle \vec{F}_1 \rangle \Delta t/m_1 \quad (14)$$

For a single component system the value of Δt is computed from the value of the most energetic particle remaining in the solid at time t . For particles of disparate mass, this is not satisfactory since lighter particles move farther than heavier ones with the same kinetic energy. A better scheme for selecting Δt is to base the determination on the largest difference between the predicted and corrected position Δr . In this case (91)

$$\Delta t_{\text{new}} = \Delta t_{\text{old}} \{\epsilon/\Delta r\}^m \quad (15)$$

where ϵ is an input parameter of order 10^{-3} to 10^{-4} chosen to yield the desired integration accuracy of the final observables. The value of m has been arbitrarily set to 0.3 for similar reasons (92). This approach allows the timestep to vary during calculation of the trajectory. At the beginning of the trajectory the timestep is typically $\sim 10^{-16}$ s and eventually increases to $\sim 10^{-14}$ s. A total of 100-200 integration steps are required. It is of interest that for these systems a low order predictor-corrector is most efficient computationally since the forces vary rapidly with distance.

In all calculations to date, the initial coordinates of the atoms are set at their equilibrium position with zero initial velocity. As shown in Figure 13, the primary ion is given a specific kinetic energy E , with polar angle θ and azimuthal angle ϕ such that

$$v = (2E/m)^{1/2} = (v_x^2 + v_y^2 + v_z^2)^{1/2} \quad (16)$$

$$v_z = -v \cos \theta \quad (17)$$

$$v_x = v \sin \theta \cos \phi \quad (18)$$

$$v_y = v \sin \theta \sin \phi \quad (19)$$

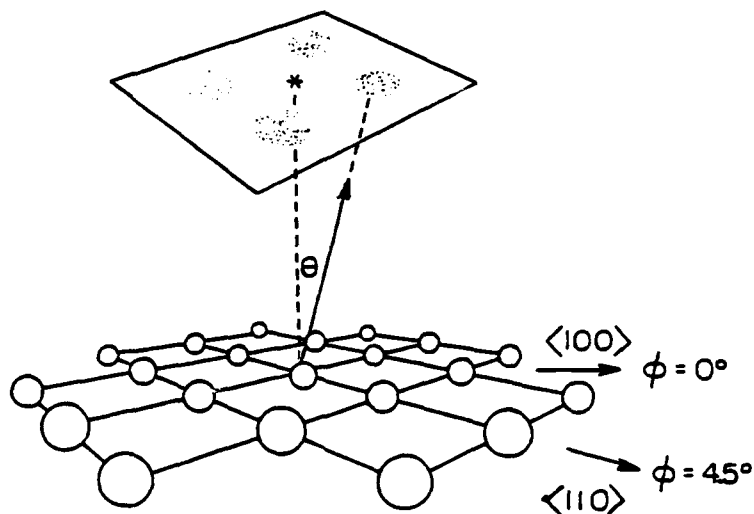


Figure 18 - Coordinate system used in determining angular distributions.

The force is calculated from the gradient of the potential energy, V ,

$$\text{as } \vec{F}_i = -\vec{\nabla}_i V(\vec{r}_1, \vec{r}_2, \dots, \vec{r}_N) \quad (20)$$

For a many-body solid, we would need a multi-dimensional potential surface that accounted for all possible positions of the particles. With our present knowledge of the solid state, this potential surface is unknown but is usually approximated using a sum of pair-wise additive potentials as

$$V = \sum_{i=1}^{N-1} \sum_{j>i}^N V_{ij}(r_{ij}) \quad (21)$$

where r_{ij} is the distance between particle i and j .

The subsequent atomic motion due to the primary ion impact is computed for enough time such that no particles have sufficient kinetic energy to escape the solid. For a metal such as copper, we have found that after the most energetic particle has less than 2 eV of kinetic energy that integration for longer times does not produce any more ejected particles.

After termination of the calculation, the particles that have ejected are tested for possible multimer formation (93,94). To check for the formation of multimers, one merely computes the relative kinetic energy E_r , plus the potential energy V_{ij} , for all pairs of ejected atoms i and j . If the total energy of the dimer

$$E_{\text{tot}}^{\text{dimer}} = E_r^{\text{dimer}} + V_{ij} \quad (22)$$

is negative, then the tested dimer is considered to be bound. Further, it is often found

that several bound dimers are formed above the surface. If some of these have common atoms, i.e. if the dimers are linked or overlapping, then higher multimers may possibly exist.

If this condition is found, $E_{\text{tot}}^{\text{cluster}}$ where

$$E_{\text{tot}}^{\text{cluster}} = E_r^{\text{cluster}} + \sum_{i=1}^{n-1} \sum_{j=i+1}^n V_{ij} \quad (23)$$

with n being the number of atoms in the cluster, is recalculated for all the atoms in the linkage. As in the dimer analysis, if $E_{\text{tot}}^{\text{cluster}}$ for the atoms in the linkages is less than zero then the atoms are considered to be a cluster.

There are other possible definitions of what constitutes a cluster. The requirement that each atom in the multimer be bound to another atom may be an overly stringent requirement for cluster stability. Rigorously, any collection of n atoms with $E_{\text{tot}}^{\text{cluster}} < 0$ is considered temporarily bound. Since, as we shall see, there are uncertainties in V_{ij} it is prudent to use the conservative definition of a cluster. Further, for $n > 2$ it is possible that the cluster will decompose before reaching the detector. For the higher clusters, then, the model really only tests to see if there are significant numbers of ejecting atoms that are in a favorable spacial position with low enough relative kinetic energy to experience binding interactions.

In addition to evaluating the possibility of cluster formation, the classical dynamics procedure allows all possible observable properties of the ejected neutral atoms to be calculated. The yield is determined by counting the number of particles which are moving away from the surface and are not bound to the solid. The kinetic energy of the ejected atoms (or clusters) is computed from the known velocities as

$$E = 1/2m (v_x^2 + v_y^2 + v_z^2) \quad (24)$$

The angular distributions are, of course, known from the velocity components since

$$\cos \theta = -v_z/v \quad (25)$$

$$\tan \phi = v_y/v_x \quad (26)$$

It is also possible to trace the path of individual atoms as they move through the cascade volume. As we shall see, this tedious job is of extreme interest in evaluating the importance of proposed ejection mechanisms. For example, it is possible to say with certainty whether multiple collisions dominate the sputtering process or whether there exists a set of experimental conditions where the linear cascades (Figure 16a) are indeed observed to occur.

The major difficulty with this model, or any model, of the ion/solid interaction is that we have only a limited knowledge of the forces acting between the atoms. Some information is available. For example, gas phase scattering experiments at a variety of energies can be used to map out the interaction potential surface (95). Extrapolating this information to the solid state is probably reasonable above energies of a few hundred eV since the solid atoms are essentially not interacting anyway at these energies. Other approaches have included attempts to fit various forms of a potential to observables such as elasticity and heat of sublimation (95,96).

Whenever the BCA is not used, pair-wise additive potentials have always been assumed. This approximation needs to be improved for two reasons. First, many solids have directional bonds - Si, GaAs or ice are examples where this correction needs to be taken into account. Second, there is a major problem in attempting to move an atom from the bulk of the solid where it may have 12 nearest-neighbors to vacuum where it exists as an isolated atom. In the calculations, this difficulty has been ignored except when analyzing for clusters where the potential used in the solid is switched to a potential more appropriate for a gas phase species. A rigorous description of the actual ejection process, then, is lacking in all models of sputtering yet proposed.

For a single component metal surface such as Cu, the Cu-Cu interaction is often represented using the interaction potential suggested by Harrison (76). This potential utilizes a Born-Mayer exponential function to approximate the high energy collisions (>20 eV) and a Morse potential with parameters determined by Anderman (96) to approximate the low energy (<5 eV) collisions. A cubic spline is used to connect the two parts. The precise form of the interaction between atoms i and j separated by distance r_{ij} is

$$V_{ij} = A e^{-B r_{ij}} \quad r_{ij} < r_a \quad (27)$$

$$V_{ij} = C_0 + C_1 r_{ij} + C_2 r_{ij}^2 + C_3 r_{ij}^3 \quad r_a < r_{ij} < r_b \quad (28)$$

$$V_{ij} = D_e \exp[-8(r_{ij}-r_e)] [\exp(-8(r_{ij}-r_e))-2] \quad r_b < r_{ij} < r_c \quad (29)$$

$$V_{ij} = 0 \quad r_{ij} > r_c \quad (30)$$

where D_e is the well-depth of the potential and r_e is the equilibrium separation distance. The incorporation of an attractive interaction helps to alleviate a number of the ambiguities of describing the atom trajectory as it crosses the surface. For example, in the "isotropic" and "planar" surface binding model, a purely repulsive potential is used even during the ejection process. Then, the kinetic energy needed to overcome the surface binding is subtracted at the end of the calculation. In the full dynamics calculations these interactions are calculated during the ejection process obviating the need for either the planar or isotropic binding models.

There are several approaches to describe the interaction between the primary ion and the solid. An accurate description of this interaction is important only at fairly high energies since most of the momentum is imparted to the solid after only a few collisions. Probably the most popular form of this interaction is the Moliere potential (85)

$$V_{ij} = Z_1 Z_2 e^2 / r_{ij} \sum_{n=1}^3 \alpha_n \exp(-B_n r_{ij}/a) \quad (31)$$

where Z_1e , Z_2e are the nuclear charges of the projectile and target atoms, a is a screening length, $\alpha = (0.35, 0.55, 0.10)$ and $B = (0.3, 1.2, 6.0)$. This sum of three exponentials is a fit to the Thomas-Fermi potential. Values of the screening length are calculated from the Firsov formula

$$a = (9\pi^2/128)^{1/3} a_0 (Z_1^{1/2} + Z_2^{1/2})^{-2/3} \quad (32)$$

where a_0 is the Bohr radius. It has been proposed that a value of a which is 20% of the value calculated in Equation 32 gives slightly better agreement with experiment. In his early work, Harrison (76) employed the Born-Mayer form of the ion-metal interaction as

$$V_{ij} = A e^{-Br_{ij}} \quad r_{ij} < r_a \quad (33)$$

$$V_{ij} = 0 \quad r_{ij} > r_a \quad (34)$$

This form apparently works well below Ar^+ energies of ~ 1 KeV but becomes much too large at energies above this value. Two forms of the interaction potential for the Ar^+ -Ni system are plotted in Figure 19.

It is important to be sure that there are a sufficient number of atoms in the microcrystallite such that the calculated observable quantity does not change as the microcrystallite size is increased further. In practice, considerable testing with various size models is important to verify this condition. For 600 eV Ar^+ ion bombarding Cu(001) at normal incidence approximately 4 layers of atoms with 60 atoms/layer are required for convergence of most of the desired quantities. As the kinetic energy of the Ar^+ ion is increased further, however, the number of atoms that are needed increases proportionately such that approximately 2000 atoms must be included to obtain convergence at 5 keV Ar^+ ion energies. The calculated yields for some different sized crystals at 1000 and 2000 eV are shown in Table I. Slightly larger crystals are also required for oblique incident angles. Much smaller crystals may be employed if only the higher energy ejected particles are of interest (97).

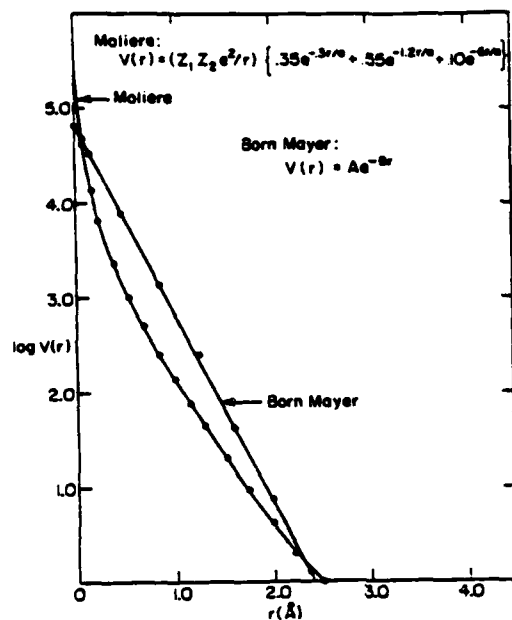


Figure 19 - Two possible Ar^+ -Ni interaction potentials.

Table I

Effect of Crystal Size on Calculated Yield for
 1000 and 2000 eV Ar^+ Ion Bombardment of Cu(001)

1000 eV		
Crystal Size # of Atoms/Layer	# Layers	Relative Yield(a)
84	4	0.84
112	4	0.96
84	5	0.90
112	5	0.95
84	6	0.93
112	6	1.00
144	6	0.92
2000 eV		
84	5	0.73
112	5	0.81
144	6	0.97
180	6	1.00

(a) Obtained using a Moliere potential for the Ar^+ -Cu interaction and a Born-Mayer and Morse potential for the Cu-Cu interaction. Yields are normalized to the maximum value in each set.

In this calculation, the only mechanism by which the crystal can lose energy is by ejection of particles either from the surface or at the sides. In Harrison's original model, considerable testing showed that it was most desirable that any particle ejected from the

side or the bottom be allowed to carry away its momentum, preventing it from further contributing to the action. If boundary conditions are employed which artificially keep the energy within the crystal, the only mechanism for energy loss is by the ejection of material through the surface. Similar difficulties exist if periodic boundary conditions are employed. The "edge" effects, then, are controlled by making the microcrystallite large enough so that its size does not influence the observable and by allowing energetic atoms moving through the sides or the bottom to simply carry away their excess energy.

The details of the trajectory are strongly influenced by the point at which the primary projectile strikes the target atom. For example, if the primary ion impacts the target atom head on, it is driven into the solid and no particle ejection is observed. For certain impact points away from this condition, however, tremendous motion is observed throughout the crystallite producing a large number of ejected atoms. This distribution, sometimes termed the number of atoms sputtered per incident ion (ASI) (98) for 600 eV Ar^+ on Cu(001) can vary from zero to greater than 20.

The fact that the yield is a sensitive function of the impact point coordinates requires sampling of all symmetrically inequivalent surface sites. In Figure 20, for example, are shown parts of the (001), (110) and (111) surfaces of an fcc metal such as Cu. The zone of irreducible symmetry is illustrated for each case. In practice somewhere between 100 and 1000 trajectories are computed at impact points over this zone to obtain the macroscopic yield of particles and other observables. The higher number of trajectories are required if the yield at a particular angle or energy is required. Detailed analysis of

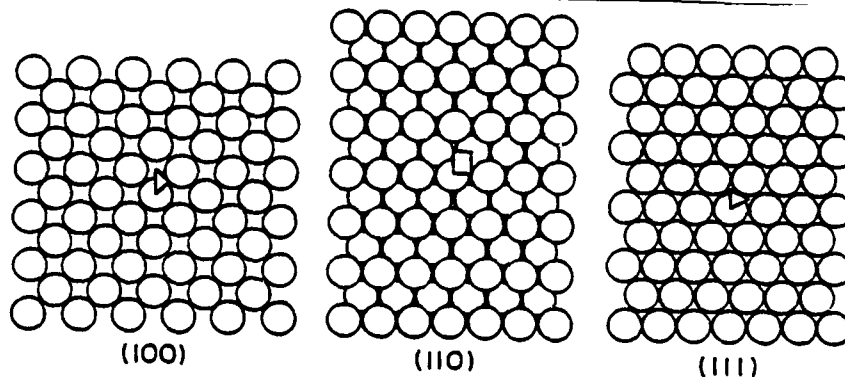


Figure 20 - Crystal surface and impact zone for the three low index faces of an fcc metal.

ejected clusters also demands a higher number of trajectories since their yield is usually only a few percent of that of the monomer. The statistical reliability of any result may be estimated as $n_{\text{obs}} \pm 2 (n_{\text{obs}})^{1/2}$ where n_{obs} is the total number of observed events summed over all the computed impact points.

The dynamics of more complex model microcrystallites is also feasible to study using the computer model. For example, chemisorbed atoms on metals (99), chemisorbed molecules (100,101) on metals, alkali halides (102) and alloys (103) have all been investigated with varying degrees of detail. For the case of atomic adsorbates, the effect of their coverage and bonding geometry can be examined to determine ejection mechanisms and the usual experimentally measurable quantities. The placement of atoms on a clean surface, however, alters the impact zone of irreducible symmetry. For example, a single atom may be placed in a linear bonded or atop geometry on the center substrate atom. This configuration approximates the zero coverage limit in that the adsorbate-adsorbate scattering mechanisms cannot occur. The impact zone, however, grows to 1/8 of the entire surface. Other configurations such as the p(2x2) (25% of a monolayer) and the c(2x2) (50% of a monolayer) ordered overlayer structures for three different adsorption site geometries are shown in Figure 21. No adsorbate atoms have been placed on the edge of the microcrystallite since these positions exhibit unrealistically weak binding forces. The impact zones for all of the cases are also shown in Figure 21; note as the symmetry decreases, the size of the impact zone increases.

The interaction potentials are formulated in much the same manner as for the clean metal case. If atomic locations are known from low energy electron diffraction or other methods sensitive to surface structure then the value of r_e in Equation 29 is known. Also, the value of D_e can be estimated from the heat of adsorption. The parameters used to construct the repulsive potential wall should only be a function of the atomic number and not of the electronic nature of the bonding since the energies are much larger than typical bond strengths. Many of the predictions of the classical dynamics calculations for these systems will be discussed in future sections.

B. Ionization of the Ejected Atoms

There is clearly a great deal of information concerning the ejection of neutral atoms from solids. The theory is in reasonably good shape, especially since many of the observables can be quantitatively predicted using the molecular dynamics calculations. All that is needed is a reasonably reliable interaction potential which can usually be constructed from fairly simply determined physical properties. The question of ionization at surfaces is an entirely different matter. For this situation, there have been literally dozens of models proposed with agreement to experiment usually no better than a couple of orders of magnitude. There has been, therefore, a focus on developing rather empirical experiments and correlations to try to get this aspect of the sputtering phenomenon under control.

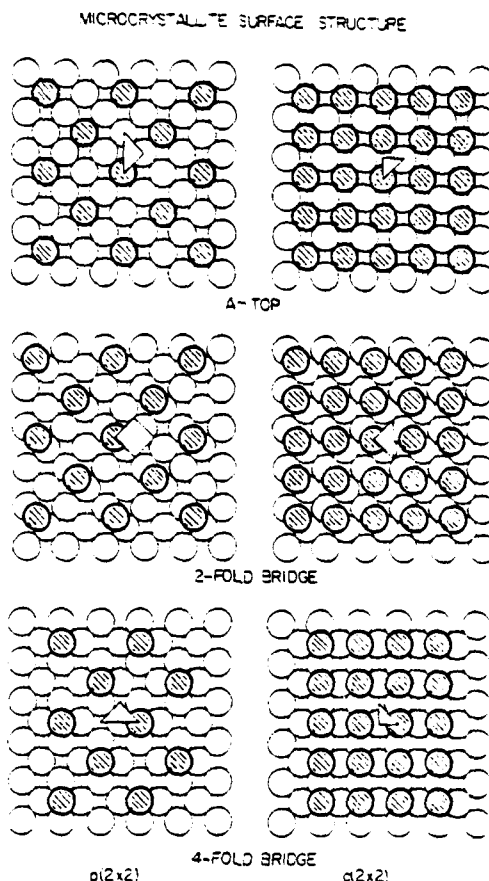


Figure 21 - Possible placements of the oxygen atoms on the microcrystallite. The shaded circles represent oxygen atoms and the open circles represent substrate atoms. The impact zones are also shown.

To provide some justification for the development of the existing theories which attempt to explain surface ionization, it is useful to lay out the important differences between atom yields and ion yields from the same substrate. In the most general sense, the neutral yields vary only by as much as a factor of 10 for a given primary ion energy for virtually all elements of the periodic table. As shown in Figure 22 for both positive and negative ions, however, it is seen that R^+ may vary by over 5 orders of magnitude (104). Next, there appears to be a rough inverse correlation between ionization efficiency and increasing ionization potential for positive ions and increasing electron affinity for negative ions (105). The neutral yields exhibit no such correlation. And finally, there has been a strong dependency noted between the electronic properties of the surface (i.e. work function) and the magnitude of R^+ for a given element. For example, the yield of Ni^+ (as well as Ni_2^+ and Ni_3^+) from a clean Ni surface bombarded by 1 keV Ar^+ is near zero (106), whereas the yield of Ni atoms is approximately 4 (1). Upon formation of 50% of a

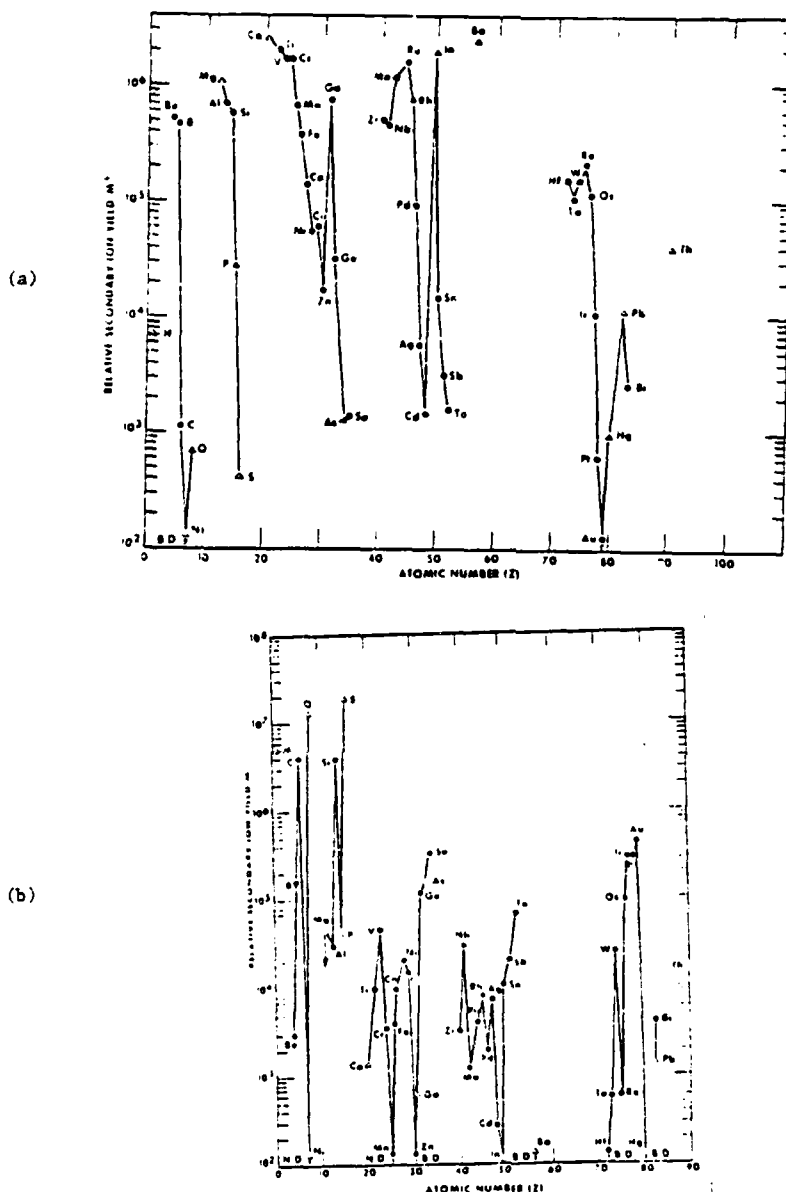


Figure 22 - (a) Relative secondary positive ion yield (M^+) due to O^- bombardment vs. atomic number of secondary ion. (●) Pure element. (Δ) Compound. (b) Relative secondary negative ion yield (M^-) from Cs^+ bombardment vs. atomic number of secondary ion. Relative intensity is given in units counts/second/ 10^{-9} A. (●) Pure element. (Δ) Compound. B.D. = Barely Detectable. N.D. = Not Detected. From reference 105.

monolayer of oxygen, however, the Ni^+ yield increases by several orders of magnitude such that $R^+ \sim 0.1$ (106). The sensitivity of the intensity of the Ni^+ signal to oxygen coverage is illustrated in Figure 23. It is this tremendous variation which causes so much difficulty in attempting to obtain quantitative SIMS data. From calculations, and by comparison to

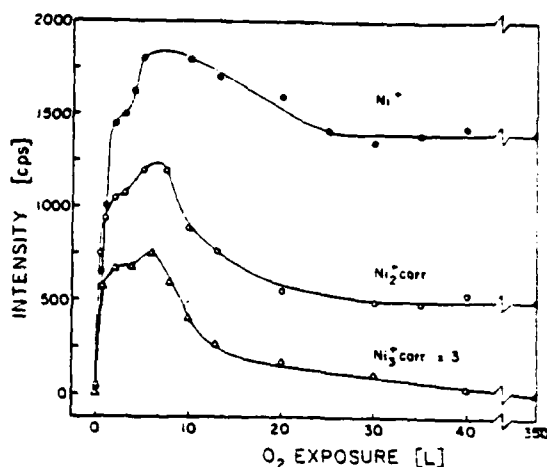


Figure 23 - Dependence of the Ni^+ , Ni_2^+ , and Ni_3^+ ion yield (most intense isotope peaks at $m/e = 58, 116, 174$) on O_2 exposure. Ni_2^+ and Ni_3^+ intensities are corrected for isotope distribution and quadrupole transmission. The corrected Ni_3^+ intensity is magnified by a factor of 3. From reference 106.

similar studies by Oechaner on oxidized Ce and Ta (107,108), we anticipate that the Ni neutral yield would decrease by at most a factor of 2 when the oxygen is adsorbed. Similar observations for negative ion enhancements have been made by Yu for Cs adsorption on various metals (109). Thus, oxygen which often increases the the surface work function enhances positive ions, while Cs which usually decreases the work function, enhances negative ions. Neither of these atoms has a major effect on neutral yields. This observation has been used for many years with the ion microprobe since sensitivities (110,111) could be greatly increased by bombarding with O_2^+ or Cs^+ , presumably since the primary ions subsequently reacted with atoms in the near surface region to form new molecular species. So as not to present a completely consistent picture, however, it should also be pointed out that O_2^+ bombardment has been observed to enhance negative ions (112).

For a given single crystal matrix, the ionization probability has been found to be reasonably independent of the azimuthal ejection angle. For Cu single crystals Yurasova and co-workers (113) found intensity variations with crystal rotation nearly identical to those reported by Wehner for Cu neutrals (15). Similar observations have been reported for Ni (114). The polar angle distributions for Ni^+ are also quite similar to those calculated for Ni atoms if an image force of 3.6 eV is allowed to bend the neutral trajectories away from the surface normal (115). These effects will be discussed in more detail later. We should also note that rather strong variations in neutralization probability with angle have been

noted when the primary ion directly scatters from the surface. For example, by comparing the scattered He^+ intensity to the scattered Li^+ intensity at 600 eV, Taglauer and co-workers found that azimuthal rotation of a $\text{Ni}(110)$ crystal did not alter the He^+ intensity (116). The Li^+ beam, which is never neutralized, exhibited large fluctuations due to second layer scattering. Thus they concluded that when the He^+ penetrated below the first layer, it was effectively neutralized but during surface collisions, neighboring atoms did not influence the ion yield. Woodruff and co-workers have studied angular variations of He^+ from $\text{Ni}(001)$ covered with 25% of a monolayer of oxygen ($p(2 \times 2)$ overlayer) (117,118). They found that when the He^+ beam scattered near a protruding surface atom adjacent to the impact point that it experienced a higher neutralization probability. At this point, then, there is conflicting evidence as to how similar atom yields and ion yields are as a function of angle.

The last observable property of importance is the secondary particle energy distribution. Qualitatively, the ions and neutrals have similar energy distributions in that ions with energy ranging from nearly zero to several hundred eV have been observed. More specifically, the ion distribution tends to be somewhat broader than the neutral distribution and tails off as $E^{-0.5}$ rather than as $E^{-2.0}$ as for neutrals. A detailed comparison has been made between Cu^+ ions and Cu atoms ejected from a polycrystalline Cu surface (24) as shown in Figure 24. Similar trends have been observed for many systems. One known exception to this observation is that low ionization potential elements like Na^+ and K^+ appear to have energy distributions either identical to, or narrower than, the corresponding neutrals. This has been observed for Na^+ in silica (119) and for K^+ on Ni (120). In any case, however, there does not appear to be a strong dependence of R^+ on particle velocity since the energy distributions of ions and neutrals are at least qualitatively similar.

As indicated above, there have been many attempts to explain some or all of the above differences between ions and neutrals. In this review, all of these models will not be recalled, rather we will focus on some important historical developments and comment on some of the most promising new approaches to straightening out the mess. Of particular interest will be those models that take into account the complexity of the sputtering event and attempt to understand ionization from a microscopic point of view.

Probably the most significant initial observation regarding the ionization probability was that the value of R^+ depends exponentially on ionization potential I as

$$R^+ \propto \exp(-I/K) \quad (35)$$

where K is a fitting parameter (105,121). The approximate nature of this relationship is illustrated in Figure 25 for a number of the elements (121). Although the form of Equation

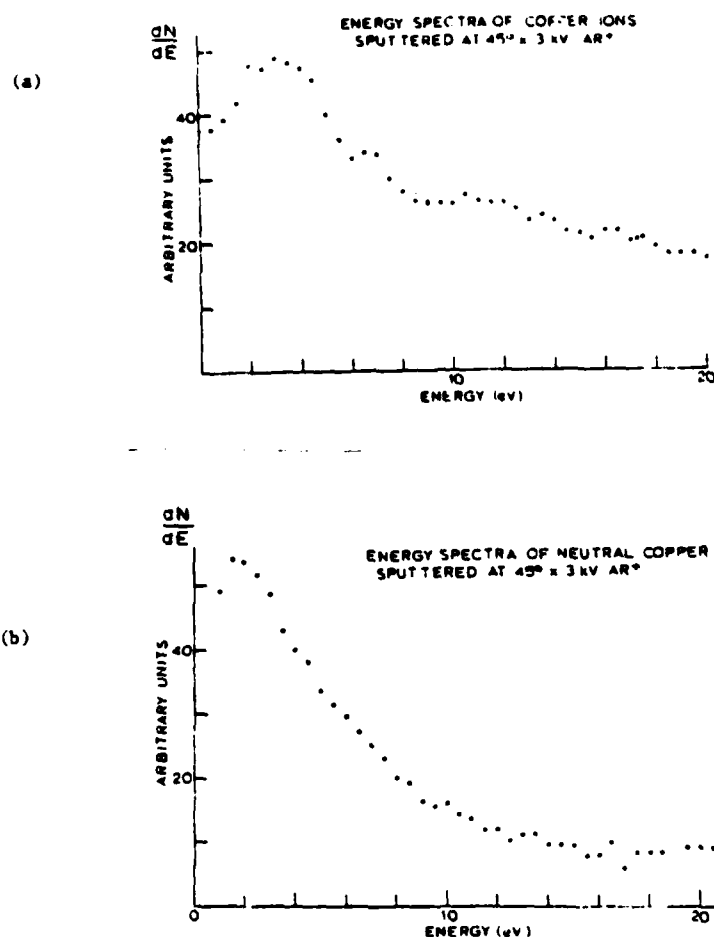


Figure 24 - (a) Typical energy spectra of sputtered Cu neutrals, obtained by electron bombardment ionization. (b) Typical energy spectra of sputtered Cu ions, showing a broader peak than that of the neutrals in (a). From reference 24.

35 seems as good as any considering the experimental difficulties in measuring R^+ , it has been a major chore to relate the result to a physically reasonable model. In a widely criticized report, Andersen and Hinthorne (121) utilized the Saha equations which are derived from Boltzmann statistics applied to a plasma equilibrium of element M with its ionized species as



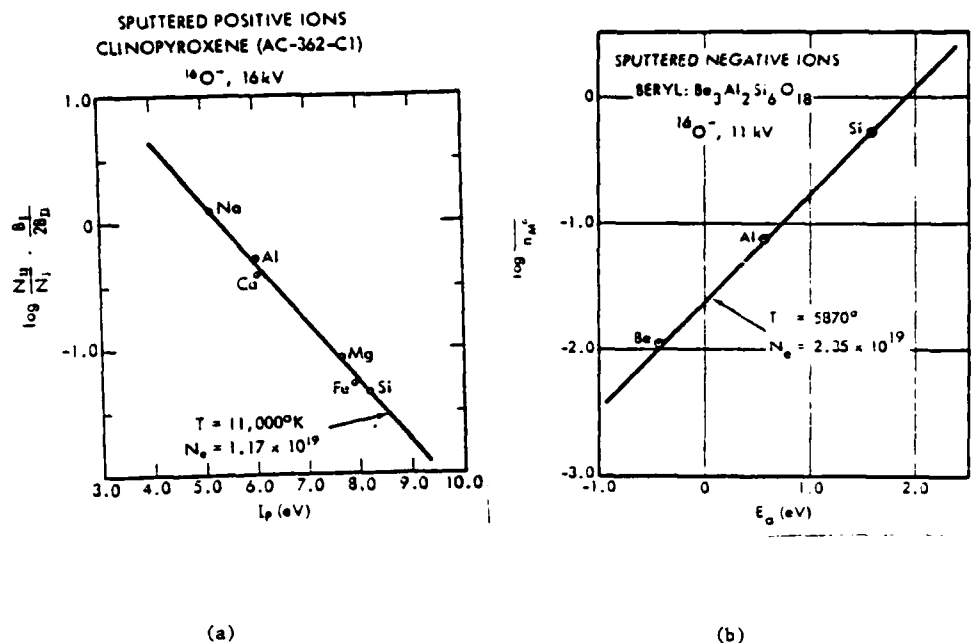


Figure 25 - (a) Saha-Eggert ionization equation applied to sputtered positive ion data from a mineral standard bombarded with $^{16}\text{O}^-$ at 16 kV. (b) Saha equation applied to sputtered negative ion data from a mineral standard bombarded with $^{16}\text{O}^-$ at 11 kV. From reference 121.

The resulting equilibrium expression is then

$$C_{\text{M}}^+ C_{\text{e}}^- / C_{\text{M}}^0 = [(2\pi m_{\text{e}} kT)^{3/2} / h m_0] \cdot (B_{\text{I}} B_{\text{e}} / B_0) \exp(-I/kT) \quad (37)$$

where the B 's are the appropriate partition functions, and the C 's represent the concentration of the indicated species. The temperature, T , is essentially a fitting parameter for a series of elements ejected from a common matrix. Typical values of T range from 2000 to 15000 K. There are many reasons why this explanation of Equation 35 is unphysical but perhaps the most persuasive is from results of the molecular dynamics calculations. These calculations show that equilibrium is not attained anywhere near the target atom during particle ejection, a result graphically depicted in Figure 1. Further, the energy distribution of the ejected particles should have a Maxwell-Boltzmann shape, a result not predicted by collision cascade models or by experimental results.

A better explanation of Equation 35 as proposed by Williams (122,123) is that the sputtered atom interacts electronically with the atoms near the ejection site via resonant electron exchange processes. Thus, if an energy level in the surface is occupied by an

electron and an equivalent energy level is unoccupied in the ejecting atom, electron exchange may occur. This situation can be approximated by Equation 35 assuming that the excited electrons are at equilibrium and may be described using Fermi-Dirac statistics. Specifically, the model assumes that the yield of positive ions, Y^+ is

$$Y^+ = YP_e \quad (38)$$

where P_e is the probability that the electronic level in the surface at energy I is vacant. The value of P_e may be defined as

$$P_e = \{1 + \exp[(I - E_c)/kT_e]\}^{-1} \quad (39)$$

where E_c is the highest occupied state in the quiescent surface and T_e is the equilibrium temperature of the electrons. In a metal E_c corresponds roughly to the work function of the surface and in an insulator or semiconductor to the valence band edge. Since the yield of atoms ejecting in a neutral state is

$$Y^0 = YP_f \quad (40)$$

$$\text{and} \quad P_e + P_f = 1 \quad (41)$$

$$\text{then} \quad R^+ = Y^+/Y^0 = \exp[-(I - E_c)/kT_e] \quad (42)$$

The schematic electronic density of states and the potential energy diagram are illustrated in Figure 26.

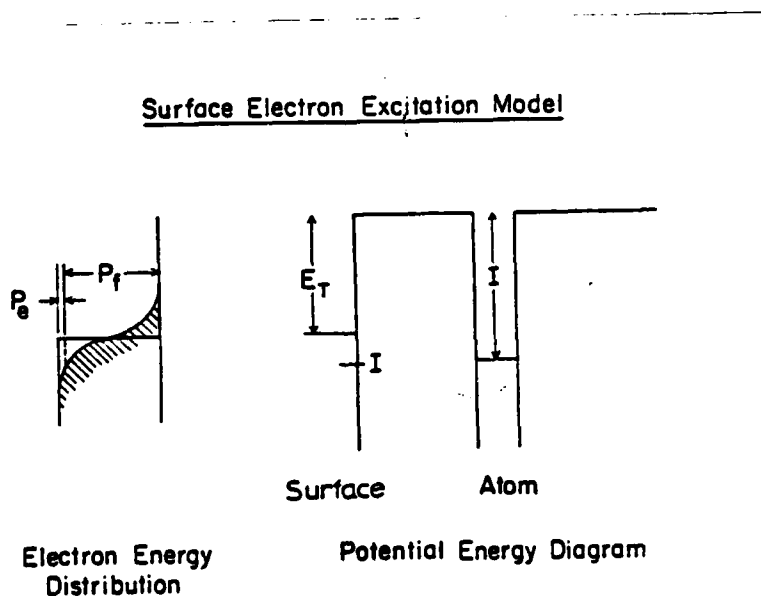


Figure 26 - Surface electron excitation model. From reference 122.

Although this model removes many of the objections noted for the Andersen-Hinshelwood rationalization, it is not readily expanded to include an explicit representation of the bulk (or surface) density of electronic states nor to include the dependence of R^+ on angle or energy. (There is an implicit approximate $\exp(-\text{const}/v^2)$ dependence of R^+ on ion velocity in Equation 42 as discussed in Reference 122). To incorporate these aspects of the problem it is necessary to know something about the wavefunctions of the atoms in the solid and to relate these wavefunctions to electron exchange probabilities between two interacting systems.

Strubek and co-workers have made considerable progress along these lines (124). Their first approach is to consider a single time independent level of an adsorbate atom ϕ_a of energy ϵ_a that interacts with a single time independent metal substrate level ϕ_1 of energy ϵ_1 . The electron is assumed to reside initially in ϕ_a on the adatom with level ϵ_1 unoccupied. If the time dependent coupling (hopping integral) between the levels $V(t)$ is slowly turned on, then the R^+ can be calculated from perturbation theory as (125,126)

$$R^+ = \left| \frac{1}{h} \int_{-\infty}^{\infty} V(t) \exp[i(\epsilon_1 - \epsilon_a)t/\hbar] dt \right|^2 \quad (43)$$

Many functional dependences for $V(t)$ have been tested although

$$V(t) = V_0 \exp(-\lambda vt), \quad t > 0 \quad (44)$$

gives the most physically realistic values of R^+ . Here, λ is a constant which describes the overlap of wavefunctions and is approximately 2 \AA^{-1} . It is of interest that if the two atoms move apart with constant velocity v from a starting separation r^0 , the coupling can be rewritten as

$$V(t) = V_0 \exp\{-\lambda[r(t) - r^0]\} \quad (45)$$

Solving Equation 43 using $V(t)$ from Equation 44 yields for the ionization probability

$$R^+ = \pi^2 V_0^2 v^2 \lambda^2 / (\epsilon_1 - \epsilon_a)^4 \quad (46)$$

Note that R^+ depends on the square of the particle velocity. The model also predicts strong dependence on the coupling between the adatom and the surface atom, both the strength V_0 and range λ , and even stronger sensitivity to the relative position of the electronic levels.

Although this approach accounts for the detailed electronic structure of the relevant atoms, it clearly is unrealistic because only two levels are involved in the collision. It

is possible, however, to generalize Equation 43 such that it includes a continuum of levels and allows for the tunneling of electrons from occupied states below the Fermi level or from Auger processes (127). This expression for R^+ may be obtained as

$$R^+ = 2/\pi \{ \exp[-C_1 \pi (I - \phi) / h \lambda v] \} \quad (47)$$

using the coupling integral given in Equation 44. Here, C_1 is a constant and ϕ is the work function of the surface. Note that this result very closely resembles the original Andersen-Hinshelwood observation. The result differs quite dramatically from Equation 46 in that it exhibits no dependence on the coupling strength V_0 and has a very strong dependence on velocity $\{\exp(-\text{const}/v)\}$. A major difficulty, however, is that the effective temperature

$$T_{\text{eff}} = \lambda v^2 / \pi k \quad (48)$$

is much smaller than experimentally observed (127,128) and calculated values of R^+ are many orders of magnitude too small.

It is of interest that a still different velocity dependence may be predicted by assuming that the adatom level ϵ_a changes in time (or distance) as the particle leaves the influence of the band of levels in the metal (125). This corrected expression is

$$R^+ \propto [(\epsilon_a - E_F) \lambda v]^{1/2} / \Delta E \quad (49)$$

where E_F is the Fermi energy and ΔE is the width of the conduction band. Thus, there are a range of models which predict the dependence of R^+ on velocity to vary from $v^{1/2}$ to v^2 to $\exp(-\text{const}/v)$ to $\exp(-\text{const}/v^2)$.

In both the two level model and the model where a continuum of energy levels are included, the explicit electronic structure of the ejecting atom and the solid are still not considered in any detail. Another difficulty - and one which is inherent in virtually every model discussed so far - is that the electronic structure of the solid must surely change as the collision cascade evolves in time. For example, the electronic structure of a metal crystal consisting of a periodic array of atoms can be described quantum mechanically using the appropriate Bloch wavefunctions and eigenstates. After the impact of the primary ion, however, this periodicity is removed completely as the atoms more closely resemble a liquid. In fact as has been pointed out by Williams (122), since the atoms are moving with energies of several eV per atom, atom-atom distances can vary over a much wider range than normally found in amorphous materials. This disorder may have the effect of localizing the itinerant electrons of a metal or of creating new states with energies within the bandgap of semiconductors or insulators. This effect is illustrated in Figure 27. Thus, it may turn out that any model which relies on the band structure of the unperturbed solid to calculate

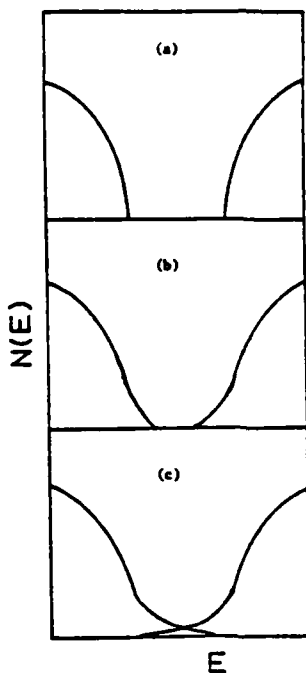


Figure 27 - Density of states $N(E)$ in crystalline and amorphous semiconductors as a function of energy. (a) crystalline semiconductor, (b) amorphous but stoichiometric semiconductor, (c) probable density of state for highly disordered semiconductor. From reference 122.

R^+ already has inherently gross errors. What is really required is a formalism where electronic motion and nuclear motion are determined in time together. This approach has been attempted for a few simple situations and offers considerable promise, not necessarily to generate quantitative predictions of R^+ , but to provide insight into the important factors which influence surface ionization.

To consider both electronic and nuclear motion, we begin using a Hamiltonian which is separated into a part that describes the motion of the atomic nuclei and a part that describes the motion of the electrons. The nuclear positions are determined using the procedure outlined earlier in this section and provide the appropriate time dependent coordinates for solution of the electronic part of the problem. This approach presumes that there is no coupling between electronic and nuclear motion and that the classical trajectory is unaffected by the electronic transitions that occur during the trajectory. The conditions where this assumption is valid have been outlined in some detail by Tully (129).

To determine R^+ for an adatom ejected from a surface, it is necessary to solve the time dependent Schrodinger equation for the system using the time dependent electronic Hamiltonian

$$H = H_{\text{el}} + U(r(t)) \quad (50)$$

Here, H_{at} is an atomic Hamiltonian, and U is a time or position dependent inter-atomic electronic interaction integral. The coupling interaction neglects electron-electron interactions so no two electron or Auger type processes are considered. The solutions to H_{at} are given by

$$H_{at}\phi_k = \epsilon_k \phi_k \quad (51)$$

where the ϕ_k 's are the orthonormal, atomic wavefunctions for the atoms in the solid.

To solve the Schrodinger equation using the Hamiltonian in Equation 50 we then seek time dependent molecular wavefunctions ψ_1 where

$$H\psi_1 = i\hbar \frac{\partial \psi_1}{\partial t} \quad (52)$$

Although there are number of possible approaches to representing ψ_1 , the efforts so far have focussed on utilizing the tight binding approximation. In this case, the electronic levels in the solid may be expressed as a linear combination of atomic orbitals ϕ_k as

$$\psi_1 = \sum_k \phi_k c_{k1}(t) \exp(-iE_1 t/\hbar) \quad (53)$$

where an arbitrary phase factor has been included. The expansion coefficients are time dependent since the position of the nuclei will be changing during the evolution of the collision cascade. Combining Equations 52 and 53 integrating over the electronic coordinates yields the following set of coupled equations:

$$i\hbar [dc_{k1}(t)/dt] = \sum_{j \neq k} \langle \phi_k | U | \phi_j \rangle c_{j1}(t) + (\epsilon_k - E_1) c_{k1}(t) \quad (54)$$

These equations of motion for the $c_{k1}(t)$'s can be integrated simultaneously with the classical equations for the nuclear motion. As was used in the two level case, the coupling matrix element or hopping integral is given by

$$\langle \phi_k | U | \phi_j \rangle = V[r(t)] = V_{kj} \exp[-\lambda_{kj}(r_{kj} - r_{kj}^e)] ; r_{kj} \neq 0, k \neq j \quad (55)$$

$$= 0 ; r_{kj} = 0, k \neq j \quad (56)$$

The value of R^* may be calculated from the coupling coefficients in the following manner:

- 1) Choose some atomic energies ϵ_k and parameters for $V[r(t)]$.
- 2) Solve for the molecular energies E_1 at time $t=0$ by setting Equation 54 equal to zero.

- 3) Determine the nuclear motion of the total system by the molecular dynamics method. At each timestep, the new nuclear positions serve as input to the coupling matrix element. The coupled equations of motion for the $c_{ki}(t)$'s are simultaneously integrated with the nuclear positions and velocities.
- 4) Evaluate R^+ at the end of the collision process by projecting the adatom state ϕ_a on all states that were originally unoccupied. R^+ is thus given by

$$R^+ = \sum_i^{\text{unocc}} |c_{ai}(t=\infty)|^2 \quad (57)$$

The numerical analysis for this prescription is currently beyond the realm of most present day computers. Currently, the solid has been approximated using a linear chain of atoms (130) and by a cluster of five atoms with the adsorbate atom placed on the surface (128) as shown in Figure 28. Another approach involves monitoring the nuclear motion of a large collection of particles (~300 or more) while only selecting a few (5-10) to follow electronically (131).

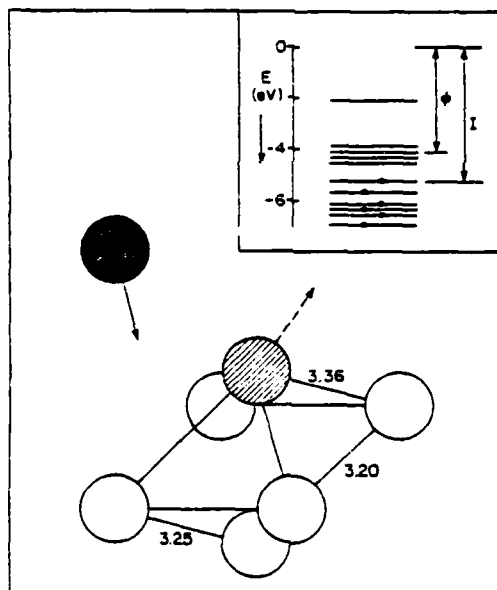


Figure 28 - The atomic model used in the computer simulation. The model consists of the atomic substrate (white spheres), the particle which is sputtered (shaded sphere), and the bombarding particle (black sphere). The interatomic distances are marked in Å. The electronic structure of the model is shown in the inset with electrons depicted by black dots. I is the ionization energy of the sputtered particle and is assumed to be 5.25 eV in this case. † marked the highest density of the empty electronic states. From reference 128.

The incorporation of the nuclear motion into the ionization theory is critical to obtain physically reasonable results. In Sroubek's model study, he found that by varying

the ionization energy of the ejecting adsorbate atom, he could produce values of R^+ which could be fit to Equation 47 with effective temperatures between 1800 and 3300 K. He could also obtain R^+ values that ranged from 10^{-1} to 10^{-5} , much more reasonable values than are obtained from lattices that are not allowed to move (128,130). Also, of interest is that for his initial studies, R^+ exhibited a very weak dependence on particle velocity. Although the development of this procedure is in its very early stages, it appears that all of the fundamental ingredients are available to construct a general understanding of the ionization phenomenon.

There are many other theories that have been set forth to try to predict R^+ , although virtually all of these are qualitative in nature. For example, in the "bond-breaking" model (132) it is proposed that if a molecule is already charged in the original solid that the atomic component may be ejected with its charge state intact. The high yield of Na^+ and Cl^- from NaCl illustrates this point nicely. Other models that incorporate surface work functions (133) or bulk band structure (134) to predict R^+ suffer from the fact that these parameters have little meaning during the collision cascade.

Another important theoretical approach focusses on the fact that once the ion is formed during the excitation process, it will undergo de-excitation as long as it is close to the surface (135). Two types of neutralization have been proposed for ions approaching a metal surface. The first type involves resonance tunneling of an electron from the filled levels of the metal to an excited level of the ion. The second type involves two electron processes where an electron from the metal fills a lower energy level of the ion. The excess energy is lost via emission of an Auger electron from either the metal or the ion. The transitions are illustrated schematically in Figure 29. The probability of a particle escaping de-excitation is given as

$$P(s=) = \exp(-A/av) \quad (58)$$

where s is the distance from the surface, A is the transition rate of an electron from the surface to the ion, a is a critical distance and v is the particle velocity normal to the surface.

The energy distribution of sputtered ions should have a similar velocity dependence as

$$y^+(v) = y^*(v)\exp(-A/av) \quad (59)$$

where $y^*(v)$ may be estimated from Equation 7 or other models available for predicting the velocity dependence of the neutrals. When Equation 59 is fit to the energy distribution of Cu atoms (136) a value of A/a of 2.5×10^5 to 1.7×10^6 cm/s is obtained which is comparable to values of A/a used to explain photon emission data (137).

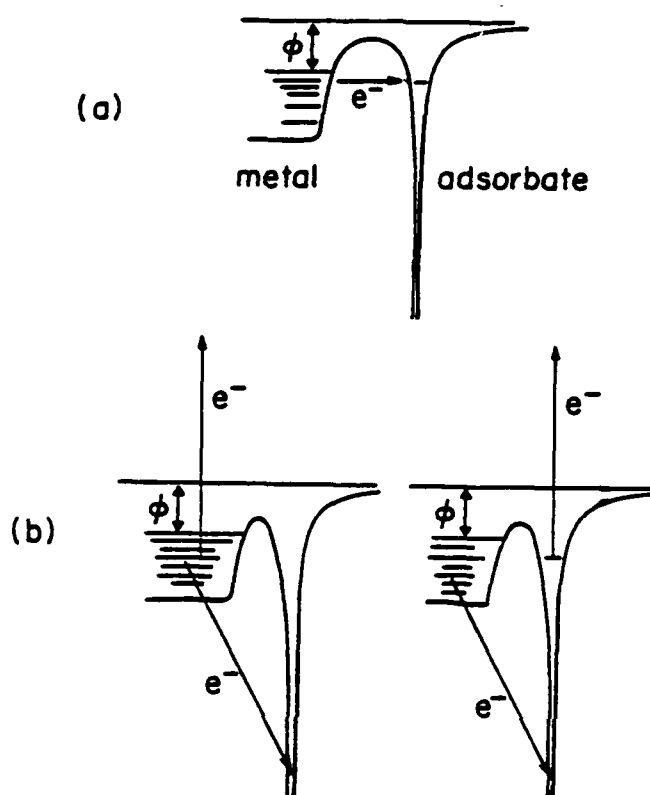


Figure 29 - De-excitation processes. Adapted from reference 135.

Although this development seems physically reasonable from a number of viewpoints, there is a major difficulty in applying Equation 59 to any real situations. The treatment assumes that the lattice effectively remains static during sputtering. As discussed earlier, Sroubek has shown that the lattice motion may effect both the total yield Y^+ and the velocity dependence of Y^+ in a major fashion. In fact, it appears that by using the coupling integral given in Equation 44 that Sroubek's approach and the ion neutralization approach will yield similar results in the limit of a static lattice. Thus, Sroubek has noted that Equation 59 predicts a velocity dependence that is much too strong (128).

There are very few experimental studies which have been capable of helping to decide which theories of the ionization process are indeed the most reliable. From a quantitative point of view, however, the velocity dependence of R^+ varies considerably from model to model and would therefore be a valuable functionality to obtain experimentally. There have been two quite detailed studies that have recently been completed that qualitatively support Sroubek's contention that the velocity dependence of R^+ should not be particularly strong. The first study focusses on the adsorption of CO on Ni(001) since this system produces intense Ni^+ signals and since the surface adsorbate structure has been well characterized by

other techniques (115). The measurements were performed using a new SIMS apparatus aimed at determining ion yields at all θ and ϕ ejection angles for a normally incident beam (120). As shown in Figure 30 this measurement was carried out by utilizing a quadrupole mass spectrometer that could be rotated under UHV conditions with respect to the incident ion beam. In addition, a medium resolution energy selector consisting of a 90° spherical sector provided the capability of examining how the angular distributions changed with secondary ion energy. The idea behind designing this apparatus was that the ion trajectories could be directly compared to those calculated for the neutrals using the molecular dynamics treatment.

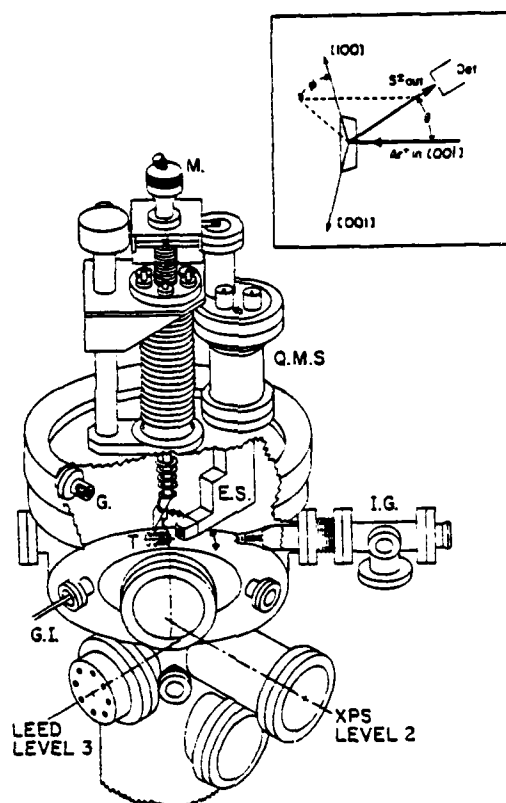


Figure 30 - Schematic view of the spectrometer. The components illustrated include M, crystal manipulator; Q.M.S., quadrupole mass spectrometer; I.G., primary ion source; E.S., energy spectrometer; G, Bayard-Alpert gauge; T, crystal target; and G.I., gas inlet. Auxiliary components are omitted for graphical clarity. The SIMS experimental geometry and coordinate system are defined in the inset. From reference 120.

The results of the measurements have so far only been analyzed for the Ni species due to the difficulty in obtaining enough particles in the calculation that are ejected at

specific angles and energies. There have been, however, several important consequences of the experiments. First, if the CO is assumed to bond in the atop site, the polar angle distributions of Ni^+ that are measured experimentally do not agree well with those calculated for a $\text{Ni}(001)$ surface covered with 50% of a monolayer of CO. As shown in Figure 31, for example, calculated polar plots peak at an angle of about 10° closer to the normal than the measured ones (115). Thus, if it is assumed that the calculations are correct, there must be a fundamental difference between ion trajectories and neutral trajectories. This discrepancy has been resolved by incorporating the presence of the classical image force into the computational model. If it is assumed that the particle instantaneously becomes an ion, E_{image} is given by

$$E_{\text{image}} = e^2/4z = 3.6 \text{ eV}/a_0 \quad (60)$$

where a_0 is the height in Å of the particle above the jellium step-edge at the instant of ionization. If θ_n is the angle of the atom's velocity vector at this point, the ion emerges with a final direction given by

$$\theta_1 = \tan^{-1}[(E_0 \sin^2 \theta_n)/(E_0 \cos^2 \theta_n - E_{\text{image}})]^{1/2} \quad (61)$$

where θ_1 is the corrected polar ejection angle as measured from the surface normal of the leaving ion, and E_0 is the kinetic energy of the neutral particle ejected at a polar angle θ_n . The corrected theoretical energy distributions using $E_{\text{image}} = 3.6 \text{ eV}$ are also shown in Figure 31. The agreement with experiment over all polar angles is now quite good. Note also that the width of the polar angle distribution is much sharper at higher kinetic energies. This expected result occurs since the particles ejected early in the collision cascade see more surface order than those ejected late, after the crystal structure is nearly destroyed.

To check that the success of this simple correction is not just coincidence, it is possible to compare both the azimuthal distributions and the energy distributions of the measured Ni^+ intensity to calculated values. For each comparison, the agreement has been very good using the same value of E_{image} (115). In fact, it has been proposed that the reason that the energy distribution for ions is usually broader than for neutrals is due solely to the presence of E_{image} (138). In relation to Thompson's energy distributions, the image potential acts as an additional surface binding force such that Equation 7 becomes

$$Y^+(E) \propto CE/(E + E_b + E_{\text{image}})^2 \quad (62)$$

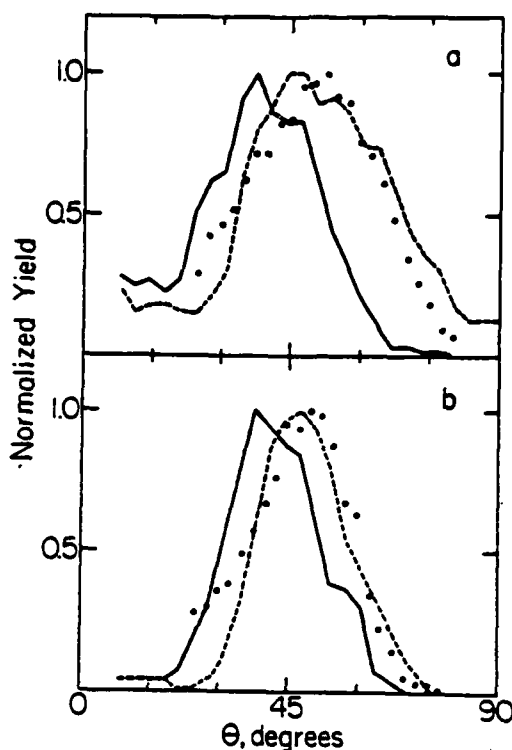


Figure 31 - Polar angle distributions for Ni ejected from Ni(001)c(2x2)-CO. The upper set of curves is recorded for a secondary ion energy of 7 ± 2 eV while the lower set of curves is taken at 22 ± 2 eV. From reference 115.

A further point is that the classical dynamics model assumes that there is no velocity dependence or azimuthal dependence to R^+ . Since this model can accurately describe the experimental situation, it must be concluded that in this case these properties of R^+ are at least approximately valid.

In a completely different approach, Yu (139) has investigated the velocity dependence of R^+ by assuming that the functional form of the Norskov and Lundquist prediction is indeed correct. By rewriting Equation 47 as

$$R^+ = (2/\pi) \exp[(\phi - I)/\epsilon_0] \quad (63)$$

where $\epsilon_0 = h\lambda v_L / C_1 \pi$, Yu reasoned that at constant v_L , a plot of $\log R^+$ vs $(\phi - I)$ should yield a straight line with slope $1/\epsilon_0$. At different v_L , however, the slope should vary according to the definition of ϵ_0 . He was able to vary ϕ by a sufficient amount by evaporating very small quantities of Li onto the sample surface. The results for O^- emission from ion bombarded oxidized vanadium are shown in Figure 32. The slope of each line should give the value of ϵ_0 . When the ϵ_0 values are then plotted vs $v \cos \theta$ as shown in Figure 33, the values

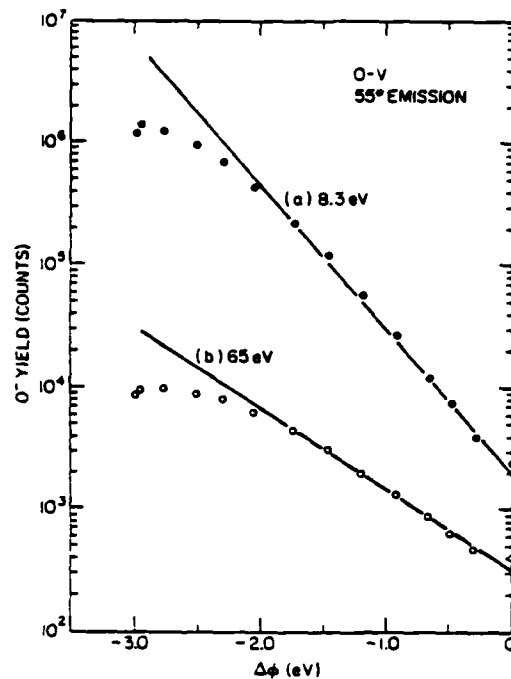


Figure 32 - The work function dependence of the O^- yield at two different emission energies 8.3 and 65 eV but for the same angle of emission 55° . Notice the exponential dependence on $\Delta\phi$ for $-\Delta\phi < 2$ eV. From reference 139.

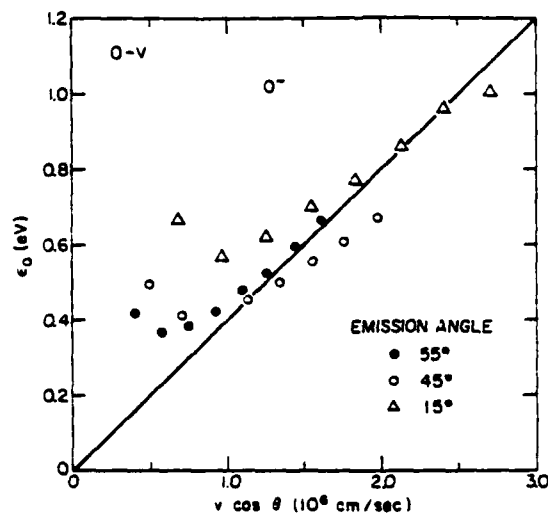


Figure 33 - The dependence of ϵ_0 for O^- sputtered from oxygenated (11) vanadium surfaces on the normal component v of the emission velocity. The approximate proportionality between ϵ_0 and v for $v_{\perp} > 1 \times 10^6$ cm/sec is in agreement with theory. From reference 139.

should fall on a straight line as predicted by Equation 47. The results show that at kinetic energies less than about 20 eV that c_0 shows almost no velocity dependence but that at energies greater than 20 eV, Equation 47 becomes valid. Since the peak in the energy distribution occurs at less than 10 eV, these experiments clearly indicate that Y^+ also exhibits a weak velocity dependence.

We have concentrated in this discussion on mechanisms of ionization that occur in concert with the development of the collision cascade. Other possible processes are thought to exist which lead to ion ejection. For example, Williams has proposed that since positive halogen ions eject with an energy distribution which is only about 15 eV wide and peaks at 6-8 eV, the ion is not produced by direct collisional events (140). The ionization is proposed to proceed via interatomic Auger decay followed by coulombic ejection of the ion in a mechanism similar to that proposed by Knotek and Feibelman to explain electron and photon stimulated desorption (141). Clearly, none of the above models would be appropriate for this situation.

To conclude this section, then, it is clear that much work has been devoted to understanding the ejection of neutrals and ions from ion bombarded surfaces. Our understanding of the neutral ejection process is somewhat more advanced than for the ions. However, there is now a formalism available for coupling the microscopic nuclear motion surrounding the ejection site to the possible electron transfer processes that can occur in the solid. For all of the theories, there are many predictions that can be experimentally tested. In the next sections we will attempt to build upon the ideas developed by the theorists to attempt to more fully understand the resulting mass spectra and to see if we can learn something about the structure and chemistry of the sample itself.

IV. Structure-Sensitive Factors

In previous sections, there has been a qualitative description of a variety of sputtering experiments that clearly contain information about the crystallography of the solid. Wehner's spots are probably the most spectacular examples of this fact. In addition, it appears that the state of the theory which describes the ion impact event is sufficiently advanced such that a more quantitative understanding of the structure-sensitive factors in sputtering should be forthcoming. Through these comparisons, it may also be possible to use ion beam methods to learn something new about the surface structure of previously uncharacterized materials. In this section, then, we will examine these structure sensitive factors for the ejection of atoms (or ions) from single crystal samples and see how well the measured observables agree with the chosen theory.

A. Yields

Recall first that the total yield of particles ejected from a copper single crystal surface is a function of crystal orientation with $Y(111) > Y(001) > Y(110)$. The experiments to determine this relation (18) were performed using the weight-loss technique and are therefore subject to a certain degree of uncertainty because of surface damage by the primary ion. In addition, the vacuum conditions were rather poor by today's standards. Yet, these observations have never been contradicted, although it would be extremely helpful to repeat many of them using as low a primary dose as possible and using simultaneous LEED monitoring. It is possible to examine the reasons for these yield differences using the molecular dynamics calculations. These calculations were first performed only recently on Cu since large model crystals are needed in order to sufficiently contain the nuclear motion that leads to particle ejection. The required computer time is rather lengthy, even for the fastest computer systems. The results of these calculations are given in Table II (142). Note that the relative order of the calculated yields agree with that obtained from the early experiments. A detailed analysis of the individual trajectories provides some insight into why this order is observed. In general, the momentum resulting from the

Table II

Sputtering Yield of 600 eV Argon on Copper(100), (110) and (111)

Crystal face	Total Number of trajectories	Total Number of atoms ejected	Sputtering Yield	Relative Yield	
				Calculated ^a	Experimental ^b
(100)	111	436	3.93	1.00	1.0
(110)	121	429	3.54	0.90	0.5
(111)	108	700	6.48	1.65	1.3

^aNormalized to the (100) face.

^bMeasured at 1 keV by weight loss, normalized to the (100) face (18).

primary ion is kept close to the surface if the density of atoms is high as in the case for the (111) orientation. For much more open configurations such as the (110) orientation the momentum more readily penetrates through holes in the surface and is lost into the bulk of the material. In fact, when examined in this way, the importance of surface morphology is most striking in that the same relative yields are also found for the low index faces of Ag (18) and Au (19). The placement of atoms in a lattice is clearly an important feature that influences the yield. This notion is also consistent with the early transparency theories of sputtering (123) which could be qualitatively used to explain the relative yields for the above situation.

This set of calculations also provided considerable insight into the mechanism of ejection of the particles from each face. The most common ejection mechanism found in these calculations is the "up-down" mechanism where the primary ion drives the target atom down into the second layer, while at the same time forcing its nearest-neighbor to eject. The momentum can be transmitted through several atoms along a close-packed row by this process as illustrated in Figure 34. Thus, it is clearly sensitive to the arrangement of surface atoms.

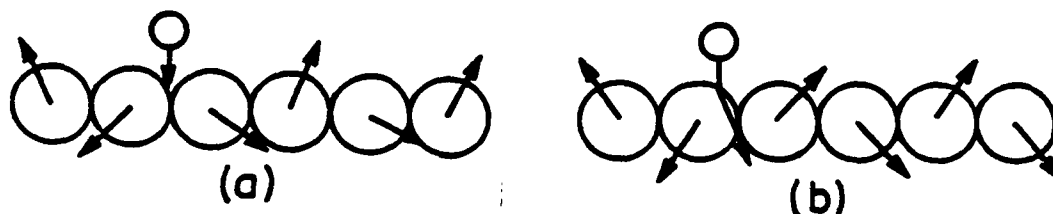


Figure 34 - Two forms of surface a layer sputtering mechanism. They occur for impact points which lie close to the axis of a close-packed chain of surface atoms. From reference 93.

For all three target orientations, most of the ejected atoms are found to originate from the surface layer as shown in Table III (142). Note that from (001), virtually every atom originates from the first layer, even though there is significant movement of atoms 4 layers below the surface. On (110), a fairly large fraction (~25%) of the atoms are ejected from the second layer, which, because of the open structure of the top layer, is also exposed. For (111) approximately 95% of the atoms originate from the first layer. These results indicate that information obtained from the ejected atoms will be highly surface specific.

Table III

Origin of Ejected Copper Atoms Resulting From
600 eV Normal Incidence Ar^+ Ion Impact

Origin of Ejected Atom (Atomic Layer Number)	Number of Ejected Atoms		
	(100)	(110)	(111)
1	435	348	672
2	1	79	28
3	0	2	0
4	0	0	0

B. Angular Distributions of Atoms Ejected from Clean Single-Crystals

A second structure-sensitive factor arises from an analysis of the angular distributions of the secondary particles. As Wehner showed many years ago, these distributions are highly anisotropic and very clearly reflect the surface symmetry. There have been many attempts to explain these distributions. One such explanation is that the ejection occurs along close-packed lattice directions which extend deep within the crystal (78). This idea nicely explained the peaks in the angular distributions but required that there be quite a bit of long range order in the solid even during the impact event. As shown in Figure 1, that requirement seems a bit hard to swallow. Although controversy existed concerning these "focusons" for many years, the molecular dynamics calculations of Harrison clearly showed that the ejection was dominated by near surface collisions rather than those from beneath the surface (76). Similarly, Lehmann and Sigmund (143) proposed that the spot patterns could be formed by the symmetry of the surface layer by a kind of blocking effect. This was a qualitative model and was never extended or applied in a predictive fashion.

Recent molecular dynamics studies have provided the most detailed explanations of the Wehner spots and have suggested a number of new experiments aimed at elucidating surface structure. Using the large micro-crystallite, the angular distributions have been determined with sufficient statistical accuracy to compare directly with the appropriate equipment. These distributions are shown in Figure 35a-c Cu(001), Cu(110) and Cu (111) (144) where each ejected atom is plotted on a flat-plate collector an arbitrary distance above the crystal. For this representation, the polar angle is determined by the radial distance from the center of the plate to the plotted point and the azimuthal angle is determined by the position of the point on a circle drawn about the origin with a radius corresponding to the appropriate polar angle. For each picture the complete angular distributions are determined after the impact zone of irreducible symmetry (Figure 20) is unfolded to completely encompass the target atom (77). Note that for the Cu(001) surface, there is a general similarity to Wehner's original experiments and near quantitative agreement to studies by Muscat and Smith (145) who found the peak in the polar angle spectra to occur at 44° . The nearly six-fold symmetry found on the (111) face and the diffuse rectangular pattern found on the (110) face are in qualitative agreement with experimental results (1,18,23). It is still dangerous, however, to make quantitative comparisons to the early experiments for the reasons already discussed.

Of particular interest is that the features in the calculated angular distributions change rather dramatically when only those particles with rather high kinetic energy, >20 eV, are selected. As shown in Figure 35d-f the fraction of particles ejected along

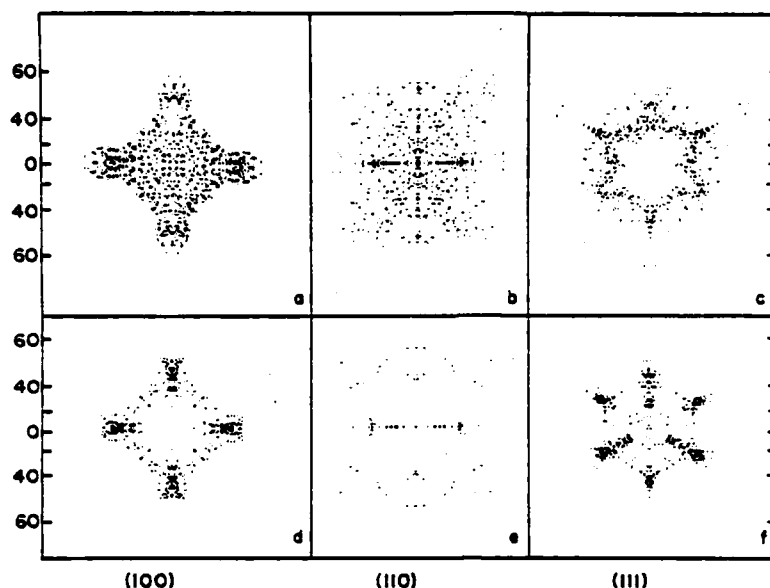


Figure 35 - Angular distributions of ejected particles for the (100), (110), (111) orientations. Each ejected atom is plotted on a flat-plate collector an arbitrary distance above the crystal. (a)-(c) All ejected particles; (d)-(f) only those atoms whose kinetic energy is greater than 20 eV. The numbers on the ordinate refer to the polar deflection angle given in degrees. From reference 144.

preferred crystallographic directions is considerably enhanced. The lower energy particles tend to have a diffuse angular distribution since they are ejected late in the collision cascade when much of the surface order is no longer present. This is a general observation and one which can be applied to enhance the structure sensitivity of any angle-resolved measurement.

Tracing individual atomic trajectories yields a clear picture of the important scattering mechanisms in the high kinetic energy regime. First, most of the ejected particles plotted in Figure 35d-f arise from within two or three lattice spacings from the impact point and suffer only a few scattering events. Second, the spacings between the surface atoms exert a strong directional effect during ejection. The fourfold holes on the (001) face, for example, constrain the path of the ejected atoms, and their trajectories proceed, on the average, in the (001) plane perpendicular to the surface. The same mechanism is applicable to the (111) face; the three elongated lobes arise from scattering through the threefold holes on the crystal surface that do not have second-layer atoms directly under them. In all cases, the atoms ejected from the microcrystallite originate from the top layer. Less angle-resolved structure is observed for the (110) orientation

since the rows in the [100] direction are sufficiently far apart to allow the atom to escape at virtually any angle.

This energy selection process also simplifies dramatically the number of operative ejection mechanisms, as the spot is composed nearly entirely from the atoms near the target atom which eject frequently. Since these particles are found to originate near the target atom, long-range surface order should not be required to produce the spot. A further consequence of examining only the higher energy particles is that the trajectory can be stopped after a shorter number of time steps and accurate trajectories can be obtained by using much smaller microcrystallites.

C. Angular Distributions for Adsorbate-Covered Single Crystals

The channeling phenomena observed from clean surfaces should also be found in more complex systems such as for metals covered with a chemisorbed layer. Only a few attempts have been made, however, to develop a comprehensive theory for the ejection of atoms or molecules from reacted surfaces. The specific case of low-energy He^+ ion bombardment of nitrogen adsorbed on tungsten has been treated using the BCA. In this case it was postulated that the nitrogen atoms could only be desorbed by direct collisions with the primary ion (146). Several desorption cross-sections for atoms on ion bombarded surfaces have also been calculated using the BCA via the computer program MORLAY (147) but agreement with experiment has been poor.

Considerable progress in quantitatively describing the ejection of chemisorbed atoms from metals has been made using molecular dynamics calculations. The first model system to be explored in detail was oxygen atomically adsorbed onto $\text{Cu}(001)$ (99). The main difficulty in describing any situation like this is to develop appropriate interaction potentials which describe the scattering events. Since little is known about these potentials, early calculations have utilized pair-wise additive potentials for adsorbates which have the same form as for the substrate, but with different mass. As we shall see, the exact form of the potential is not as critical as the atomic placement of the adsorbate atom. Thus, in the calculation, the geometry and coverage of the adsorbate may be varied over a wide range to test how these quantities influence ejection mechanisms and ultimately the angular distributions.

The calculated mechanisms for oxygen ejection in this case are quite interesting. There are two common pathways for oxygen atom ejection which involve direct collisions with the primary ion. The Ar^+ ion can strike the target oxygen atom, which subsequently reflects off a neighboring Cu atom and ejects. Alternately, the Ar^+ ion can initially reflect from the target copper atom, strike a nearby oxygen atom, and cause it to eject. Both of these processes are illustrated in Figure 36a.

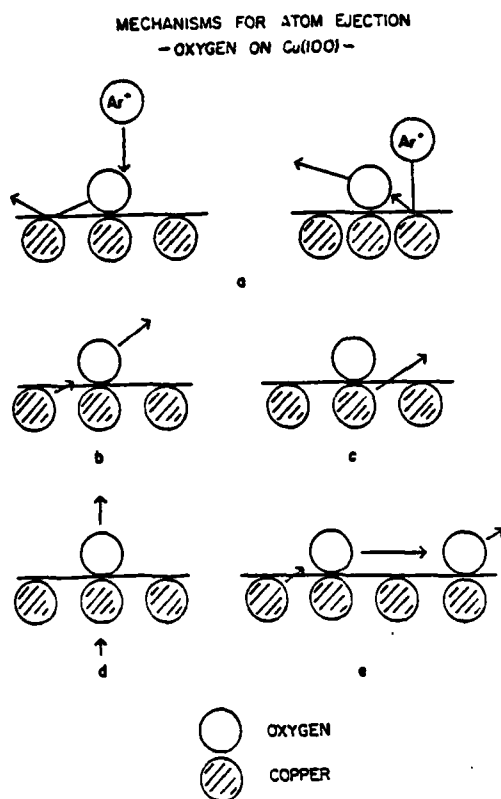


Figure 36 - Mechanisms for oxygen atom ejection on Cu(100). From reference 99.

Other more complicated collision sequences can be identified as important contributors to oxygen atom ejection. For example, in Figure 36b, the copper atom adjacent to the adsorbate starts to leave the solid, but finds an oxygen atom sticking up in its path. Depending on their collision angles and the kinetic energy of the copper atom, both particles may or may not eject. An oxygen atom can also be desorbed by the copper atom directly beneath it, as shown in Figure 36d, although it is more common for the copper atom to escape the solid from underneath the oxygen without ejecting it, as shown in Figure 36c. The reason for this phenomenon is that only a small percentage of the energetic copper atoms eject normally to the surface.

Since the lattice surface structure dominates the ejection angle of the faster-moving particles on a clean surface, it appears logical that blocking the preferred ejection directions with adsorbed atoms should have a strong effect on the angular distributions. Using the configurations given in Figure 21, for example, the calculations have been performed for a $c(2 \times 2)$ overlayer of oxygen on Cu(001) where the oxygen is placed in an atop,

2-fold bridge and 4-fold bridge bonding geometry. In Figure 37 are shown the relevant oxygen distributions for the atop and fourfold bridge site (144,148). As it turns out, the angular distributions for the Cu substrate atoms are only slightly affected by the lighter oxygen atom and look very much like those shown in Figure 35 for clean Cu. For oxygen in the atop site, the pattern also exhibits ejection angles with mainly the same symmetry as the substrate. For the bridged configuration, however, the pattern is rotated 45° with respect to the substrate and is easily distinguishable from the other geometry.

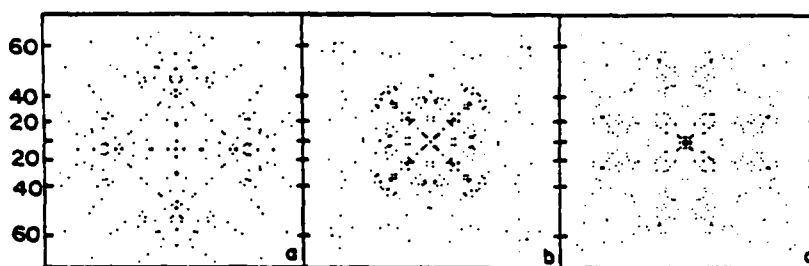


Figure 37 - Calculated angular distributions of oxygen atoms ejected due to Ar^+ ion bombardment at 600 eV. The oxygen originated in a $c(2 \times 2)$ coverage on $\text{Cu}(001)$ in various site symmetries and heights above the surface, h . The numbers refer to the polar deflection angle. (a) A-top or linearly bonded site, $h = 1.9 \text{ \AA}$. (b) Fourfold bridge site, $h = 1.2 \text{ \AA}$. (c) Fourfold bridge site, $h = 0.9 \text{ \AA}$. From reference 148.

The scattering mechanisms that give rise to these angular distributions can be discerned on an atomic level from an analysis of the trajectories. It is sufficient to note here that the ejecting substrate atoms most strongly influence the directions of the ejecting adsorbate atoms and that multiple scattering in the overlayer is of secondary importance. This result portends that the angular distributions of the oxygen atom might even be sensitive to its height above the surface when placed in a given geometry. This hypothesis is borne out in Figure 37c where the oxygen height is reduced from 1.2 \AA to 0.9 \AA above the Cu plane. The theory suggest that with sufficiently accurate measurements atomic positions should be determinable to better than $\pm 0.1 \text{ \AA}$.

It would be delightful if experimental methods existed to test the very exciting predictions regarding these angular distributions. With the possible exception of the laser fluorescence method, however, none of the methods discussed in Section II have anywhere near the sensitivity to detect oxygen atoms from an oxygen monolayer before destroying the sample itself. The static SIMS method, however, provides plenty of sensitivity if the angular distribution of the ions, rather than the neutrals, are measured. This approach assumes

that the trajectories of the ions and neutrals have a certain correspondence - a point which appears reasonably valid from the data given in Section III B. for the CO/Ni system (115).

Attempts to verify the predictions of the molecular dynamics calculations have been carried out to a limited extent using an angle-resolved SIMS technique (149). To measure the angular distributions of ejected oxygen and copper atoms, a cylindrical shield was placed above the crystal surface as shown in Figure 38. The polar angle, θ , for ejected species was fixed at 45° with two appropriately placed apertures while the azimuthal angle, ϕ , could be varied over 360° by rotation of the crystal. When the 45° electrostatic sector in front of the mass spectrometer was utilized, the kinetic energies of the ejected particles could be roughly selected while maintaining a large enough bandpass necessary to maintain sensitivity. This experimental configuration will produce results equivalent to making a circular cut of the spot pattern at a radius corresponding to the 45° polar deflection but does not allow the entire pattern to be reproduced. It is possible to prepare a $c(2 \times 2)$ overlayer of oxygen on Cu(001) by exposure of the crystal to 1200 L (1 L = 10^{-6} torr s) of O_2 at 25°C .

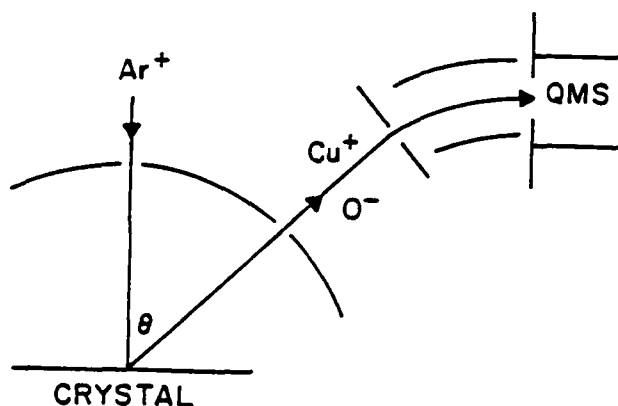


Figure 38 - Schematic representation of the angle-resolved SIMS experiment. From reference 149.

The observed azimuthal plots for Cu^+ and O^- ejection from these samples are shown in Figure 39a. The fourfold symmetry of the (001) orientation is clearly evident for both species, although their maxima in intensity are out of phase by 45° . This result is only consistent with the calculated results if the oxygen has adsorbed in the fourfold bridge site. The detailed comparison taken using a fourfold averaging and background subtraction procedure is shown in Figure 39b, assuming the oxygen is 1.2 Å above the surface. If the calculation had been performed for oxygen placed only 0.9 Å above the surface, the predicted curve would be considerably different (114).

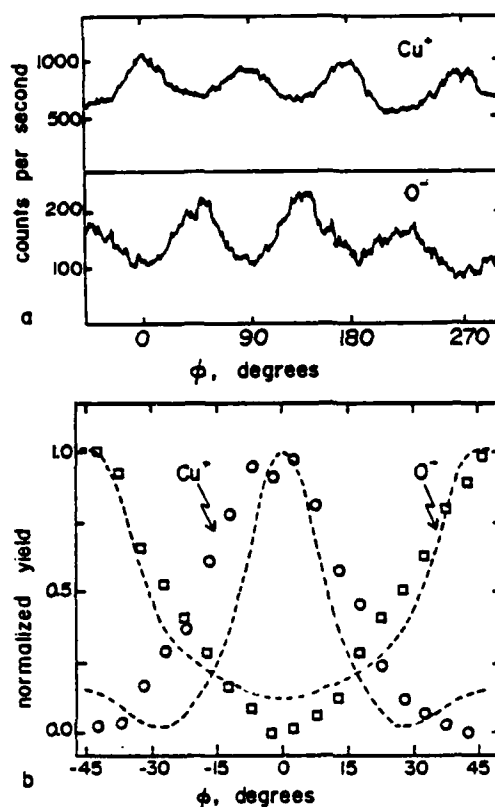


Figure 39 - (a) The Cu^+ and O^- azimuthal plots as recorded from the spectrometer. (b) A fourfold average of the data in (a) with the minimum intensity subtracted from each curve. The dashed lines represent the calculated curve for O placed in a fourfold hole 1.2 Å above the Cu plane. The circles represent the Cu^+ intensities and the squares represent the O^- intensities. The primary ion is 1500 eV Ar^+ at a total dose of 1-3 ions/ cm^2 . From reference 149.

Of crucial importance to the interpretation of these spectra is to determine how sensitive the calculated patterns are to the vagaries of the input potential parameters. This question has been examined in some detail for the O_2 on $\text{Ni}(001)$ system by Kapur and Garrison (97,150). These workers found that it should be reasonably safe to assign the type of adsorption site (e.g. atop or bridge-bonding) even if the potential parameters are uncertain since the channeling directions are basically unaffected by changes in the atomic sizes. If the adsorbate height is of interest, however, they found that it was important to know the effective size of the adsorbed atom at the scattering energy. Otherwise, there could be a large uncertainty in the determined crystallographic coordinates.

Although these types of measurements and calculations are only in their very early stages, the preliminary results have important implications. First, the experiment itself

provides a unique situation which allows detailed comparison between experiment and theory. The level of agreement between ion yield measurements and calculated neutral yields suggests that there is a close correspondence between the trajectories of the two types of species. This observation has important implications in distinguishing the various ionization mechanisms proposed in Section III. And finally, if details of the experiment and the theory can be further refined, the approach may prove to be a powerful new method for determining the positions of atoms on surfaces.

V. Cluster Formation Processes

A second critical aspect of the ion bombardment process involves the fact that molecular cluster species are often observed to be ejected from the surface. As discussed in section II, a variety of different types of cluster have been observed from a wide variety of sample substrates. For adsorbates on clean metals, the simplest types are composed of the metal atoms themselves as M_n^+ where n can be as large as 12 or more (46). In addition, there can be combinations of adsorbate atoms with the metal atoms to form a myriad of mixed clusters. The family $M_nO_m^z$ for oxygen covered Ni where $n=0-4$ and $m=0-3$ represents an example of this type (151). In addition, there have been many cases where a molecular adsorbate has been observed to eject intact, as is the case for fairly large organic molecules such as for *p*-aminobenzoic acid adsorbed onto silver (152).

There are many fascinating questions regarding the formation of these clusters. For example, does the presence of a given molecular fragment indicate that species actually existed on the surface? Or is the bombardment process too catastrophic to preserve the fragile information carried through chemical bonds? If the clusters do arise from contiguous surface atoms, can their presence provide key information regarding the local atomic structure of surfaces of alloys and supported metal catalysts? The association of Ni_2CO^+ and $NiCO^+$ to bridged and linear bound CO (Figure 15) is an application of this concept. Further, is there any point to measuring the angular distributions of ejected clusters and can they be used to probe surface structure? And finally, how does the charge on the cluster influence its formation probability? Will there be a difference in cluster formation mechanisms for positive ions, negative ions or neutrals? In this section, we shall probe the mechanism of cluster formation and examine some of the past and future uses of the clusters in the ion bombardment experiment.

A. Theoretical Aspects of Molecular Ejection

Ever since the initial discovery (44) that molecules could be ejected from ion bombarded solids, the genesis of cluster formation has been the subject of numerous investigations. The first major effort arose after the development of a time-of-flight technique aimed at measuring the energy distribution of ejected neutral dimers (153)

provided the energy distribution of K_2 sputtered from K. With this data, Konnen, Tip and DeVries were able to apply the results of the transport theory to obtain a theoretical dimer energy distribution (48). By assuming that the atoms in the dimer arose from neighboring atoms on the surface and by utilizing Thompson's expression for the energy distribution of the monomer, they computed the normalized probability density for two particles which have a given relative energy and center of mass velocity. The resulting energy distributions were then compared to the experimental data for K_2 and K sputtered from a polycrystalline K target with satisfactory agreement between experiment and theory. The theory has also been extended to include the formation of larger clusters (67) such as those observed by Staudenmaier (46). The success of their predictions led these workers to propose that the clusters are formed by recombination of independently sputtered atoms and that their energy distributions are determined by the E^{-n} power laws of the monomer distributions. The concepts have never been fully exploited, probably since the energy distribution formulas that serve as the basis of the development are in themselves rather crude approximations and are not easily generalized.

The molecular dynamics calculations have been extremely successful in enhancing our microscopic understanding of how the clusters form and in helping to evolve a number of general considerations in developing cluster formation theories. The first study regarding this subject was completed by Harrison and Delaplain (93) who investigated the bombardment of Cu single crystals by 600 eV Ar^+ using the classical equations of motion given in section II. Although they utilized a small microcrystallite and were only able to sample a few impact points on the surface, using Equation 22, they were able to find a number of examples where two atoms were above the surface with negative total energy. This condition means, of course, that in the absence of other energy transfer processes that the atoms are bound onto a stable dimer. Of primary interest in this study was that the atoms that formed the dimer were not atoms that were contiguous on the Cu surface. In fact, they found that most dimers form from next-nearest neighbors since the up-down mechanism (Figure 33) reduced the probability that neighboring atoms would have low relative kinetic energies. Thus, the study supported the work of Konnen, Tip and DeVries (48) who believed that the dimers formed over the surface, but questioned their assumption about the proximity of atoms that form a dimer.

Harrison's early landmark calculations were mechanistically very important but they failed to provide any real guides for the experimentalists. More recently, however, the extent of the calculations have been sufficiently expanded and refined such that a number of additional aspects of the problem can be examined in detail. One refinement involves the appropriate choice of interaction potential used to test for dimer formation. The solid pair-potentials account for many body interactions but do not have the correct dissociation

limits. For example, Cu_2 has a gas phase well depth of 2.05 eV (154) whereas the ⁶²bulk pair potential has a well depth of only 0.48 eV (93). Since the tested interactions occur above the solid, then the dimer pair potential should be more appropriate to use in determining cluster stability than the solid pair potential. Other improvements in the calculation relate to the increase in computer speed available from the latest computer systems. With this technical advance, it is feasible to generate a set of trajectories with statistically reliable yields for many types of clusters using microcrystallites that are large enough to contain the ion impact event (155).

In general, the calculations indicate that there are a surprisingly large number of clusters that would be expected to form by this mechanism as has been indicated qualitatively by a number of experiments. Although there are no experiments which provide dimer yields from single crystals, Oechsner has measured the Cu_2/Cu and Cu_3/Cu ratio from polycrystalline Cu using his SNMS technique (29), which are compared to calculated values for Cu(001) in Table IV. The comparison of the actual yields are in excellent agreement for the dimers and in poor agreement for the trimers. The calculated number could be too high either from the use of an overly strong potential to describe Cu_3 or from the fact that some of the Cu_3 molecules could dissociate before reaching the detector. The experimental number might be somewhat low since fragmentation of Cu_3 during ionization was assumed to be negligible.

Table IV
Theoretical and Experimental Comparison of Cu_2/Cu and Cu_3/Cu Ratio

	(001) ^a	Polycrystalline ^b
Cu_2/Cu	.077	0.104
Cu_3/Cu	.014	0.001

^aCalculations performed at 1000 eV Ar^+ ion incident at $\theta=0^\circ$ using a Moliere potential to describe the Ar^+-Cu interaction.

^bExperimental data taken for 1000 eV Ar^+ ion incident at $\theta=0^\circ$ (29).

There has also been found to be a strong dependence of the cluster yields on surface morphology. Recent experimental studies have been completed on Ni(001), (110) and (111) where the relative yields of $\text{Ni}_2^+/\text{Ni}^+$ and $\text{Ni}_3^+/\text{Ni}^+$ have been determined to be in the same relative order as the monomer yields (156). The experiments were fortunately completed under conditions appropriate for comparison to the dynamics calculation, i.e. ultrahigh vacuum with low Ar^+ ion doses to avoid surface damage. Even though the calculations utilized attractive potentials for Cu_2 rather than for Ni_2 and they considered only neutral dimers and not the ionic species, the same trends in the calculations were observed as for the experiment (155). Apparently these other effects are not as important in influencing

relative cluster yields as are relative positions of surface atoms.

These ideas can be qualitatively extended to explain the presence of even larger clusters. The atomic motion that leads to the formation of a pentamer from Cu(111) has been examined in detail (94). In this case, as shown in Figure 40, there are three collision sequences interacting in a concerted fashion which produce 5 atoms moving in parallel above the surface. Note that the atoms that comprise the Cu_5 molecule (atoms #2,3,4,5 and 6) do not consist of contiguous atoms but do arise from a highly localized region of the crystal surface.

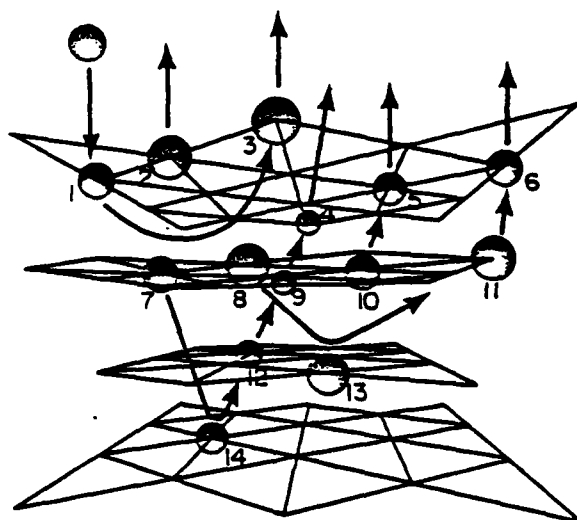


Figure 40 - Schematic representation of the pentamer formation. Only the atoms involved in the ejection of the indicated atoms are drawn. Other atoms are located at the intersection of the grid lines but are not shown. The actual size of the crystallite used in the calculation is considerably larger but is not shown for graphical clarity. The sizes of the atoms are arbitrary to allow maximum viewing through the crystal. The arrows indicate the approximate direction of motion of each atom during the trajectory. The numbers near the atoms are simply used as labels (see text). From reference 94.

For clean metals, then, it appears that the clusters form by a recombination of atoms over the surface of the crystal while the atoms are still within interaction range of the solid. Since the mechanisms by which certain correlated collision sequences lead to cluster formation appear to be crystal structure dependent, it makes sense to examine the angular distributions of ejected clusters. The fact that there were strong angular effects was first noted by Staudenmaier (137) for W_2^+ ejected from W(110). In that case, he found that the W_2^+ intensity maximized at similar angles as the W^+ intensity. Those experiments,

however, were performed with 150 keV Ar^+ ions under heavy dose conditions making quantitative comparisons to calculations difficult.

A more recent study on Ni(001) using static SIMS with 2 keV Ar^+ ions produced qualitatively similar results as shown in Figure 41 (114). The azimuthal distributions for Ni^+ and Ni_2^+ peak in the $\langle 100 \rangle$ directions ($\theta=0^\circ$) although the Ni_2^+ distribution is more anisotropic than the Ni^+ distribution. As it turns out, the molecular dynamics calculations

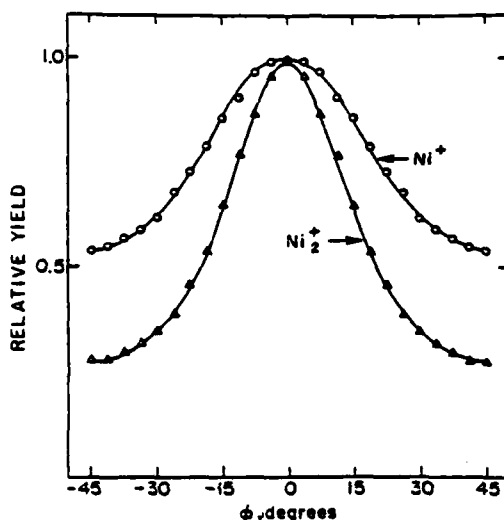


Figure 41 - Experimental angular distributions of Ni^+ and Ni_2^+ ejected from Ni(001) at a polar angle of $45^\circ \pm 5^\circ$. The center-of-mass kinetic energy of the particles is between 10 and 50 eV. Both curves are fourfold averages of the original data. The incident Ar^+ ion has 2 keV of kinetic energy and is at normal incidence. The solid is at room temperature. The peak counts are ~900 and ~500 counts/sec for the Ni^+ and Ni_2^+ distributions, respectively. The $\langle 100 \rangle$ azimuthal directions correspond to $\phi=0^\circ$. From reference 114.

provide very similar angular distributions for Ni and Ni_2 if only the higher kinetic energy particles are considered. The results of over 1000 trajectories are shown in Figure 42. For the higher energy dimers, the calculations predict that at $\theta=0^\circ$ nearly all are formed from the specific mechanism illustrated in Figure 43. With this process, then, the observed dimers should originate from next-nearest neighbors along the close-packed row.

In a similar vein, it is also conceptually possible to envision certain mechanisms that dominate the ejection process when the Ar^+ ion is incident on the crystal at non-normal angles. Foley and Garrison have predicted that the next-nearest neighbor dimers predominate if the Ar^+ ion is incident at $\theta=0^\circ$ but that nearest neighbor dimers become more important at $\theta=45^\circ$ and $\phi=45^\circ$. This effect is shown quantitatively in Figure 44. Similar calculations on a two dimensional slab of NaCl suggest that it is possible to peel fairly long chains of

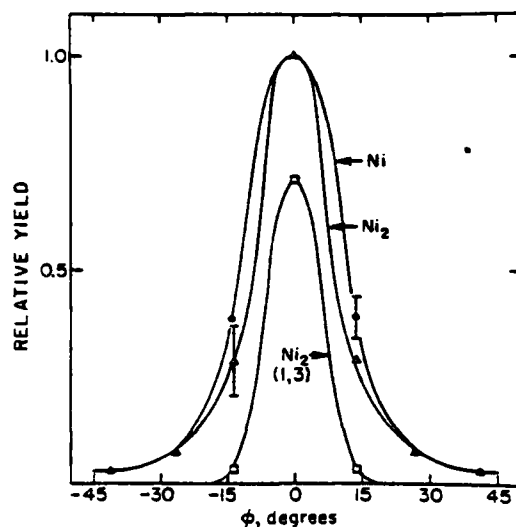


Figure 42 - Calculated angular distributions of Ni and Ni₂ at a polar angle of 45° ± 5°. The center-of-mass kinetic energy is between 10 and 50 eV. Also shown is the contribution to the Ni₂ distributions from dimers formed on atoms No. 1 and No. 3 of Figure 43. The peak intensity is 110 and 12 particles for the Ni and Ni₂ distributions, respectively. From reference 114.

contiguous atoms from the surface at certain incident angles of the primary ion (102). Thus, although rearrangement clearly occurs as the atoms that form the clusters leave the solid, it may be possible to evaluate the degree of rearrangement by selection of the appropriate angles. If this concept were extrapolated to alloy surfaces such as CuNi, the relative placement of the alloy components should be able to be determined from the angular distributions of the Ni₂, Cu₂ and NiCu species.

The next level of chemical complexity involves cluster formation from ion bombarded metal surfaces that have reacted with simple atoms or molecules to form an adsorbed layer. We examined the mechanisms of ejection of the atoms for the oxygen/Cu situation in Section IV, but it was not clear whether or how clusters could form. We now consider what factors are important in influencing cluster formation for two different situations; that is oxygen adsorption which often produces atomic oxygen, and carbon monoxide adsorption where the CO attaches to the surface in a molecular state.

For the case of atomic oxygen adsorption, we consider first the possibility of forming the O₂ molecule via the recombination mechanism proposed to exist for cluster formation from clean surfaces. It is possible to test for O₂ formation in the calculation by computing all O-O interactions between ejected oxygen atoms using the interaction potential for gas phase O₂ (99). The results clearly show that the coverage and adsorption site symmetry are major factors in determining which clusters are likely to form. The most spectacular example

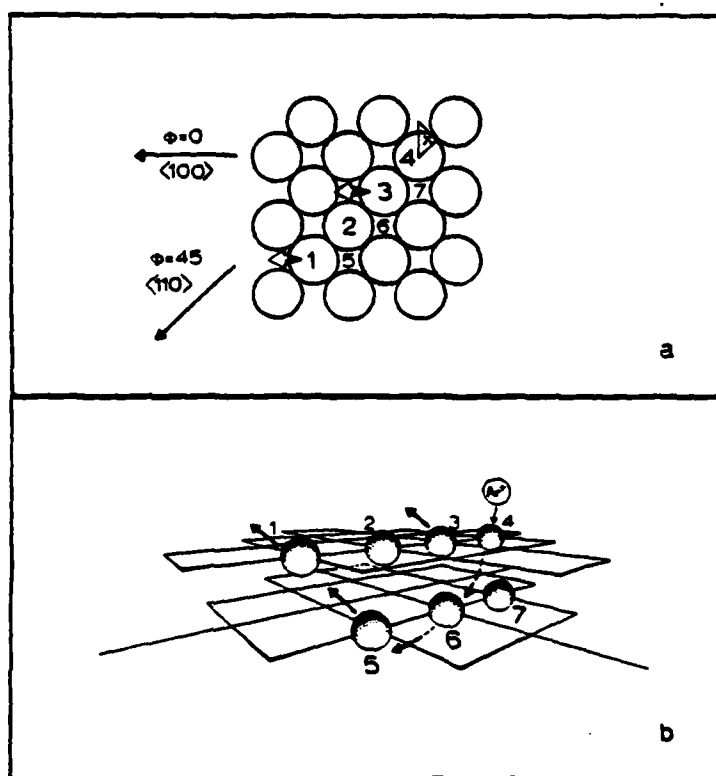


Figure 43 - Mechanism of formation of the Ni_2 dimer which preferentially ejects in the $\langle 100 \rangle$ directions, contributing the majority of intensity to the peak in the angular distribution. (a) $\text{Ni}(001)$ showing the surface arrangements of atoms. The numbers are labels while the X denotes the Ar^+ ion impact point for the mechanism shown in Figure 43b. Atoms 1 and 3 eject as indicated by the arrows forming a dimer, which is preferentially moving in a $\langle 100 \rangle$ direction. (b) Three dimensional representation of a Ni_2 dimer formation process. The thin grid lines are drawn between the nearest-neighbor Ni atoms in a given layer. For graphical clarity, only the atoms directly involved in the mechanism are shown. From reference 114.

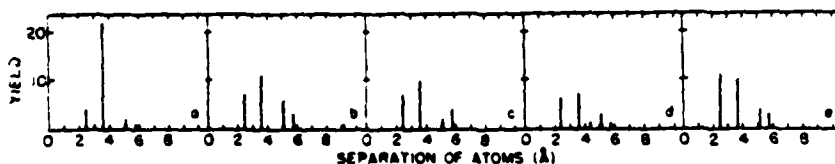


Figure 44 - Yield of dimers versus original separation of constituent atoms on the surface. The nearest neighbor separation on copper is 2.56 Å. The positions of the lines are the separation distances of the atoms in the surface. (a) $\theta=45^\circ$, $\phi=0^\circ$; (b) $\theta=45^\circ$, $\phi=11.25^\circ$; (c) $\theta=45^\circ$, $\phi=22.50^\circ$; (d) $\theta=45^\circ$, $\phi=33.75^\circ$; (e) $\theta=45^\circ$, $\phi=45^\circ$. From reference 92.

involves the effect of coverage on the O_2 formation probability. For a $p(2 \times 2)$ coverage (0.25 monolayer) the calculations show that the oxygen atoms are simply too far apart to have a significant opportunity to collide within interaction range of the solid. For a $c(2 \times 2)$ coverage (0.5 monolayer), however, the probability of O_2 formation is enhanced by about a factor of 4.

This effect has also been observed experimentally for O_2 adsorption on Ni(001) (139). As shown in Figure 45 the O_2^-/O^- ratio increases to a value of 0.04 where LEED experiments indicate the $p(2 \times 2)$ structure predominates. This value rises to a maximum of 0.16 at the $c(2 \times 2)$ coverage. Thus, the O_2^-/O^- ratio increases by a factor of 4 as the coverage is doubled, similar to what is predicted by the calculations for oxygen in a bridge position (158). The fact that the O atom density must be reasonably large to observe O_2 emission has been used in the analysis of SIMS data of oxygen on Pb (159). In this study both the O_2^- to O^- ratio and the PbO_2^- to PbO^- ratio were reasonably constant versus oxygen exposure. Even at low coverages of oxygen atoms, O_2^- and PbO_2^- clusters were being detected. This implies a nucleation mechanism for the adsorption of the oxygen. If the oxygen were adsorbing randomly, one would expect the O_2^- to O^- ratio to significantly increase with increasing oxygen exposure.

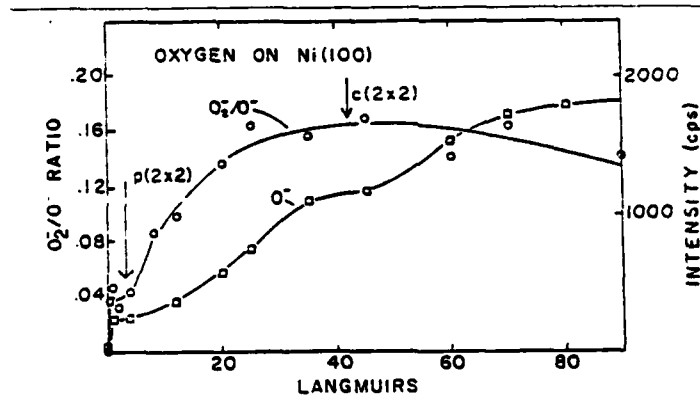


Figure 45 - Experimental ion yields vs oxygen exposure for O^- and the O_2^-/O^- ratio from Ni(001). From reference 158.

Many other types of molecular clusters have been observed to be ejected from a variety of oxidized metal single crystal surfaces. As mentioned previously, oxidized Ni is a good example with Ni^+ , Ni_2^+ , Ni_3^+ , O^+ , O_2^+ , NiO^+ , Ni_2O^+ and $Ni_2O_3^+$ all observable (151). The calculational model provides insight into how these clusters arise. For the case of oxygen on Cu(001), the atomic trajectories clearly show that all types of clusters form over the crystal surface after the components of the cluster eject in a more or less independent manner. The mechanism of cluster formation is completely analogous to that proposed for the

clean metals. Considerable rearrangement of atoms on the surface that form the cluster is possible; the species are not lifted out of the surface intact, although considerable local atomic order is preserved. Since the constituent atoms of a cluster originate from a localized region on the surface, the incorporation of oxygen into a nickel crystal to form NiO(001) should affect the Ni cluster yields. In these experiments the Ni_3^+ trimer yield is more dramatically reduced than is the Ni_2^+ dimer yield, since the exposed NiO crystal statistically has few Ni atoms in the localized region (151). All of the Ni-O clusters observed in SIMS have been found in the calculations to form by this "over the surface" mechanism.

No matter how favorable the surface morphology is for cluster formation, the clusters will not be observed if they are not thermodynamically stable. One measure of the stability of dimers is the well depth D_e of their mutual interaction potential. The yield of CuO dimers as a function of a hypothetical gas phase D_e is shown in Figure 46 (160). The yield

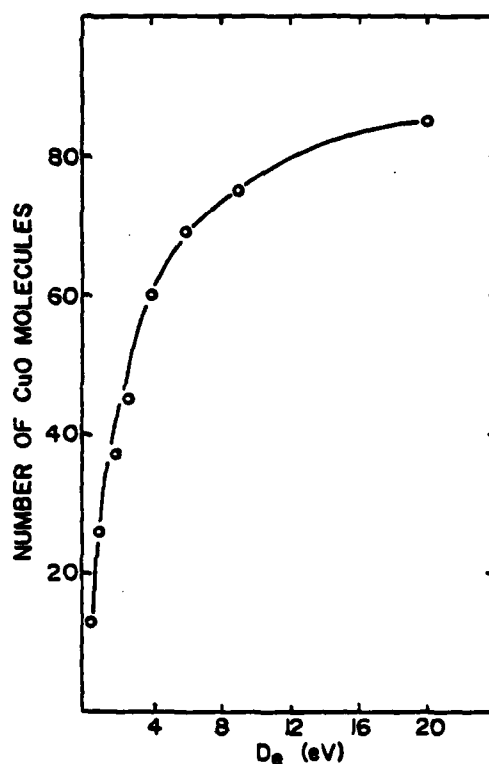


Figure 46 - CuO yield vs gas phase well depth D_e . The oxygen atoms were placed in a 2-fold bridge configuration in a $c(2 \times 2)$ coverage with a binding energy $E_b = 0.75$ eV. A total of 110 trajectories were calculated. From reference 160.

increases approximately linearly with D_e for $D_e < 4$ eV and then plateaus. The leveling off is due to a finite number of slow moving atoms that can form clusters. If the initial

energy of the incident ion were increased so that the total number of atoms available to form clusters were increased, then the linear region would be extended to larger values of D_e . Note that even at $D_e=0.1$ eV there are two pairs of atoms with extremely small relative kinetic energy so that two bound dimers are observed.

The binding energy E_b of an adsorbate to the surface also influences the yield of clusters. The effect of E_b on the CuO dimer yield is shown in Figure 47. In all cases the

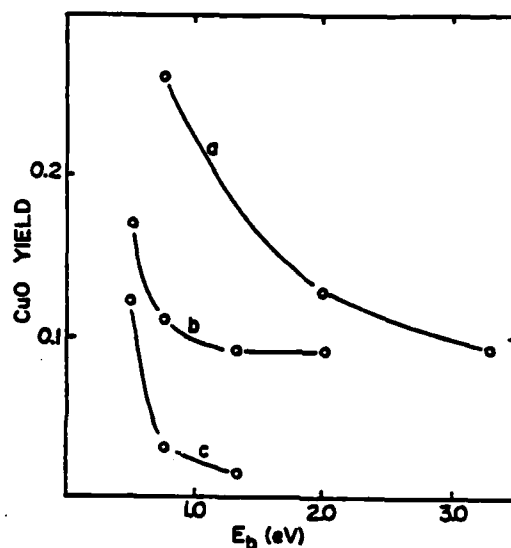


Figure 47 - CuO yield vs binding energy E_b . Curve a is for the c(2x2) fourfold bridge configuration, curve b is for the c(2x2) A-top configuration, and curve c is for the p(2x2) A-top configuration. A wall depth D_e of 2.7 eV is used to determine the yields. From reference 160.

qualitative trend is the same, the number of CuO dimers decreases with increasing binding energy of the oxygen to the surface. The calculations show that the O atom yield also decreases with increasing binding energy (99), thus the CuO yield reflects the total number of oxygens available for bonding. For all the calculations shown in Figure 47, the Cu yield is nearly constant. If the CuO molecules were ejecting intact, one would expect the opposite trend - the more strongly bound the oxygen is to the copper the more CuO dimers that should be found ejecting.

The response of a surface to ion bombardment covered with a molecularly adsorbed species is mechanistically distinct from the atomic adsorbate case. For CO on Ni(001), for example, the strong C-O bond of 11.1 eV and the weak NiCO bond of 1.3 eV help to keep the

molecule together during ejection. In the experimental studies, the main peaks in the SIMS spectra for a Ni(001) surface exposed to a saturation coverage of CO are Ni^+ , Ni_2^+ , Ni_3^+ , NiCO^+ , Ni_2CO^+ , and Ni_3CO^+ as shown in Figure 48. All ions show a smooth increase in intensity with CO adsorption and reach saturation after 2-L CO exposure (0.5 monolayer coverage). The yields of C^+ , O^+ , NiC^+ and NiO^+ , are all less than 0.01 of the Ni^+ intensity

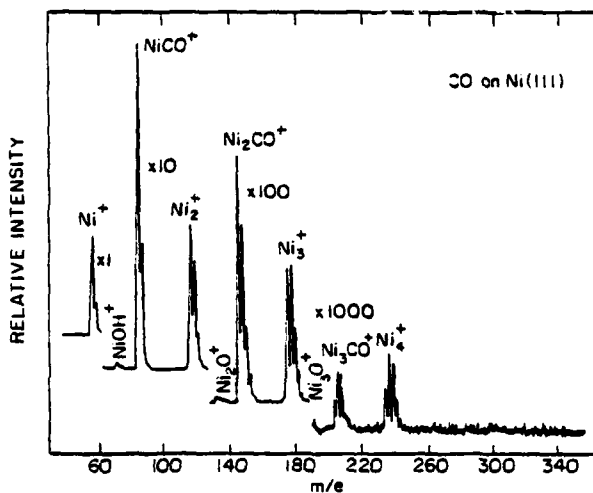


Figure 48 - SIMS spectrum of Ni(111) after 2L exposure to CO. The primary ion was 1000 eV Ar^+ with a total dose of 10^{12} ions.

The classical dynamics treatment for CO on Ni(001) yields results which are in qualitative agreement with these findings. Approximately 80% of the CO molecules that eject are found to eject intact, without rearrangement. The formation of NiCO and Ni_2CO clusters have been observed to form over the surface via reactions of Ni atoms and CO molecules. No evidence has been found for NiC or NiO clusters in the calculations. The ion bombardment approach, then, is a very sensitive probe for distinguishing between molecular and dissociative adsorption processes.

A number of workers have attempted to identify structural relationships found using other techniques such as LEED and vibrational spectroscopy to cluster yields in SIMS. The correlation of Ni_2CO^+ to bridge bonded CO and NiCO^+ to linear bonded CO is an example of this approach. As it happens, the calculations clearly show that the mechanism of cluster formation is not consistent with this picture since the clusters form over the surface via atomic collisions. Furthermore, recent combined LEED/SIMS results indicate that the cluster ion yields are not directly related to the adsorbate/ substrate geometry (161). The $c(2 \times 2)$ structure of CO on Ni(001) with all the molecules in the atop site gave the same $\text{Ni}_2\text{CO}^+/\text{NiCO}^+$ ratio as the compressed hexagonal LEED structure which must have both atop and

bridge bonded CO molecules. It is of interest, however, that Fleisch et al. (106) did find a change in the $\text{NiCO}^+/\text{Ni}^+$ ratio as the hexagonal structure began to form. Dawson and Tam (162) found that the secondary ion yields could not be simply correlated to linear or bridge bound species. They obtained the SIMS spectra for $c(2 \times 2)\text{-CO}$ on $\text{Ni}(001)$ where the CO is all linearly bound and for CO on a $\text{Ni}(001)$ surface presaturated with H_2 , where the CO is thought to be exclusively in a bridge bound state. They found no correlation between the presence of bridge bonded CO and the formation of Ni_2CO^+ . In fact, these workers concluded that changes in ion yields were more closely related to the heat of adsorption which varies with surface coverage than to any surface structural effects.

Although most of the above arguments are qualitative in nature, they do serve to muddle the notion that the cluster yields reflect the original bonding geometry of the CO. On the other hand, it is clear that angular distributions for atomic adsorbates are very sensitive to the surface structure so it is not unreasonable to anticipate similar effects for the Ni/CO system. Extensive calculations using the molecular dynamics procedure (115) have been completed for the atop and twofold bridge bonding configurations but statistical considerations have restricted the analysis to only the Ni atoms. As shown in Figure 49, when the CO is in the atop geometry, the calculated Ni distributions peak along azimuthal directions which are similar to the clean surface. For the twofold bridge case, however, the CO overlayer tends to randomly scatter the ejecting Ni atoms producing a much different pattern.

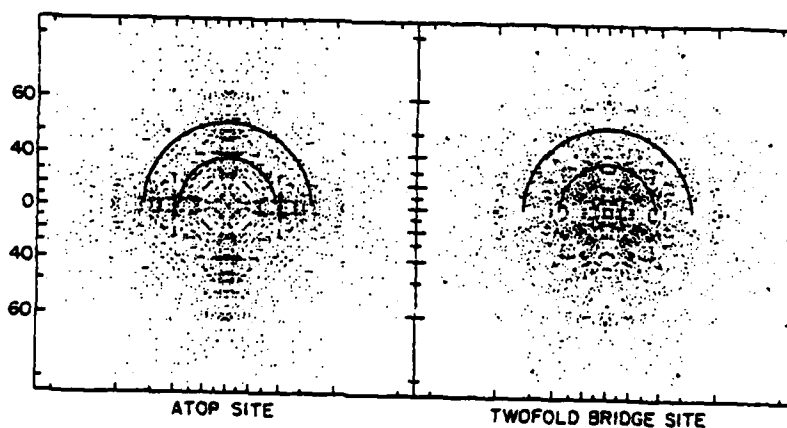


Figure 49 - Predicted angular distributions of Ni^+ ion intensity for the CO adsorbed in atop and twofold bridge sites. The numbers on the ordinate refer to the polar deflection angle given in degrees. The display is oriented the same as Figure 18 so that the horizontal and vertical directions correspond to $\phi=0^\circ$. The points between the circles contribute to the azimuthal distribution at $\theta=45 \pm 7^\circ$. Only those particles with kinetic energies of 3 ± 3 eV were counted. From reference 115.

There has been a recent attempt to confirm this prediction using the new angle-resolved SIMS apparatus discussed earlier (120). The experimental results for the azimuthal distributions for Ni^+ were found to be in excellent agreement with calculated values for Ni with atop bonded CO if the calculated values were corrected for the presence of the image force (115,138). Furthermore, there was poor agreement with calculations when assuming bridge bonded CO. Thus, there is no question that the angular distributions are sensitive to the surface structure of the adsorbed overlayer.

We are left with somewhat of a dilemma with regard to the interpretation of the static SIMS experiments for the CO on Ni(001) case. The original interpretation of the changes in the $\text{Ni}_2\text{CO}^+/\text{NiCO}^+$ ratio by Barber et al. (53,54) is clearly incorrect as indicated by the mechanistic implications of the molecular dynamics calculations. In addition, other workers have been unable to extend the predictions of their ideas. However, it is also clear that the scattering angles are sensitive to surface structure so there may well be reasons to correlate certain types of molecular clusters to certain types of surface structures, although in an indirect fashion. These generalizations and final resolution of this problem must still await further experiments and calculations on this very challenging system.

It is of interest to analyze the internal state distribution of the ejected CO molecules (100). Since the collisions which lead to ejection are often energetic, it is most appropriate to picture the molecule as dumbbell shaped, rather than spherical or elliptical as would be the case for very low energy collisions. Thus, the molecule is generally struck on one end, causing it to spin rapidly. Using the standard techniques of small molecule classical scattering (163), the available internal energy can be partitioned between vibrational and rotational energy. As shown in Figure 50, a significant fraction of the ejecting CO molecules are calculated to be vibrationally excited. A force-fit of the results to a Boltzmann distribution produces a vibrational temperature of 3400-15000 K. Note that the comparison to Boltzmann behavior is rather poor, indicating the system is far from thermodynamic equilibrium. The calculation also shows that the rotational states are highly excited, with an almost random population of states to J values as high as 100. The effective rotational and vibrational temperatures, then, are vastly different.

Similar experimental evidence for this type of internal state distribution has recently been reported by Lineberger and co-workers (164). They examined the fluorescent spectra of sputtered O_2^- and FeO^- and found that the vibrational temperature was approximately 5000 K in both cases. They further noted that the electronic temperature and the vibrational temperature were quite different, again arguing against a thermal equilibrium model. Their spectrum is shown in Figure 51.

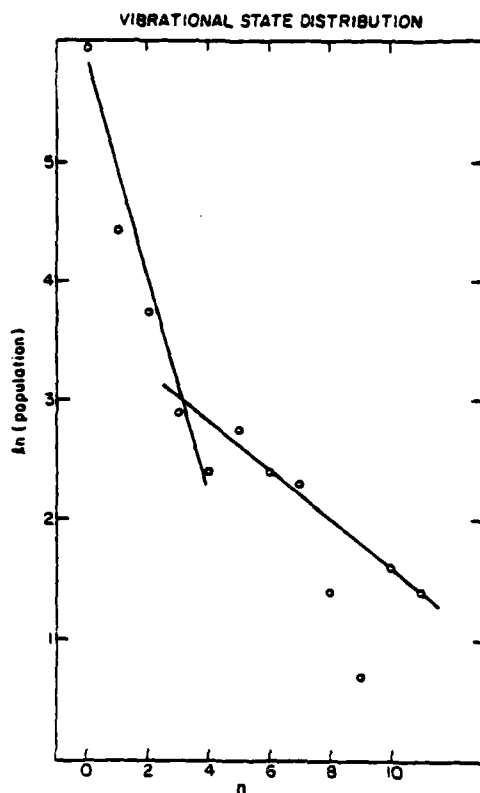


Figure 50 - Vibrational state distribution for the molecular ejected CO species. The temperature corresponding to the line of steepest slope is 3450 K, while the temperature corresponding to the other line is 15400 K. From reference 94.

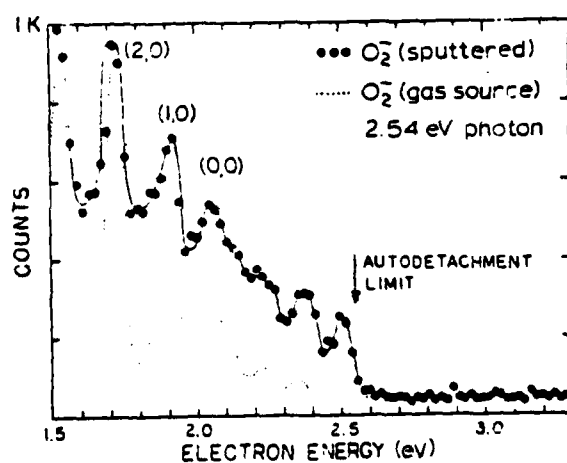


Figure 51 - O₂⁻ photoelectron spectra obtained with the gas-discharge ion source and the sputter ion source. The sharp break in the O₂ hot band progression at $v=4$ occurs because this state is no longer stable with respect to O₂ + e. From reference 164.

From the variety of the above studies, it is possible to put forth several general mechanisms of cluster formation which should be useful in the interpretation of mass spectra. First, for systems where the atoms in the solid have no preferred molecular identity, the recombination mechanism must surely predominate. This situation would exist for pure metals, alloys or chemically reacted surfaces where the adsorbate is not too strongly bonded to the substrate and interacts simultaneously with many substrate atoms.

From the variety of the above studies, it is possible to put forth several general mechanisms of cluster formation which should be useful in the interpretation of mass spectra. First, for systems where the atoms in the solid have no preferred molecular identity, the recombination mechanism must surely predominate. This situation would exist for pure metals, alloys or chemically reacted surfaces where the adsorbate is not too strongly bonded to the substrate and interacts simultaneously with many substrate atoms. Second, if the solid contains molecular entities with strong intramolecular forces but weak intermolecular forces, it is clearly possible that clusters may eject intact by lattice fragmentation. Examples of this type would include molecular solids like ice (165) and molecular adsorbates on metals where the adsorption bond strengths are much lower than the bond strengths within the adsorbing molecule. Finally, it is possible that clusters can form by a combination of both of the above mechanisms. For the case of ice, for example, each individual water molecule may eject intact, but then form water multimers over the surface by recombination.

B. Molecular Clusters and the Ionization Problem

As it has been applied so far, the molecular dynamics model ignores any effects related to electron exchange processes and ionization. It is reasonable to question the validity of the predictions of this model in view of the fact that positive or negative ions are detected in the SIMS experiment. A number of workers have addressed this question at least in a qualitative fashion, and the observations help considerably to understand the role of ionization in cluster formation processes.

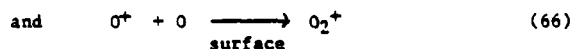
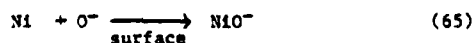
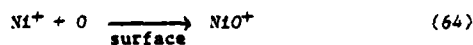
One of the first comments on this question was made in regard to differences in the interaction potential expected for charged species vs. neutral species. For oxygen adsorbed on Cu(001), for example, the molecular dynamics model indicates that the O_2 molecule would be expected to form by the recombination mechanism. For this specific system, it is also possible to examine the effect of charge state on the dimer formation probability since Morse potential parameters are known for O_2^+ and O_2^- . By putting these parameters as given in Table V into Equation 29 and using the criteria for dimer formation in Equation 22, the probability of forming a dimer between an O^- or O^+ ion and an O atom can be deduced (99). Of particular interest is that the number of calculated dimers differs by less than a factor of 2 for the three cases O_2^+ , O_2 and O_2^- . The most striking feature of the results, however, is that the thermodynamically most stable species, O_2^+ , produces the lowest number of dimers. The reason for this fact is that the range of the potential is the smallest for

Table V
Potential Parameters for O_2 , O_2^+ and O_2^-

Species	D_e (eV)	B (\AA^{-1})	R_e (\AA)
O_2	5.12	2.67	1.21
O_2^+	6.48	2.87	1.12
O_2^-	4.07	2.11	1.31

this species. Apparently, the number of possible two-body interactions that a particular atom might experience is more important than the ultimate stability of a dimer in its equilibrium configuration. If it is possible to generalize this idea further, we would expect oppositely charged species such as Na^+ and Cl^- to have a very high probability of forming an $NaCl$ molecule due to the infinite range associated with purely electrostatic interactions.

A test of the formation of cluster ions by an atom-ion collision mechanism was attempted using the $Ni(001)$ surface during exposure to oxygen (158). In this case, the ions Ni^+ , NiO^+ , O^+ and O_2^+ could be monitored as a function of the oxygen dose. The results as shown in Figure 52 are striking, as the shapes of the ion yield vs. coverage curves are quite different depending upon the ion involved. Note, however, that the NiO^+ yield has a similar shape as the Ni^+ yield whereas the NiO^- and O^- and the O_2^+ and O^+ curves also seem to track each other. If one invokes a cluster formation mechanism as discussed above, then the cluster ions could form as a result of collisions between neutral and ionized atoms. For example, the NiO^+ ion should form by interactions between Ni^+ ions and O atoms. The reaction of Ni atoms and O^+ ions would not be important due to the low levels of O^+ ions. Furthermore, if the number of ions above the surface is much less than the number of neutrals (which is the case for most materials except perhaps alkali halides), the intensity of the resulting cluster ion will be controlled by the amount of the corresponding atomic ion. Thus for Ni , the clusters would form by the following reaction:



The mechanism of cluster formation for ions would therefore be very similar to that of the neutrals.

This idea was examined in more detail by Yu (109) in a set of elegant experiments involving Cs deposition on oxidized Ti surfaces. Before Cs deposition, he observed using

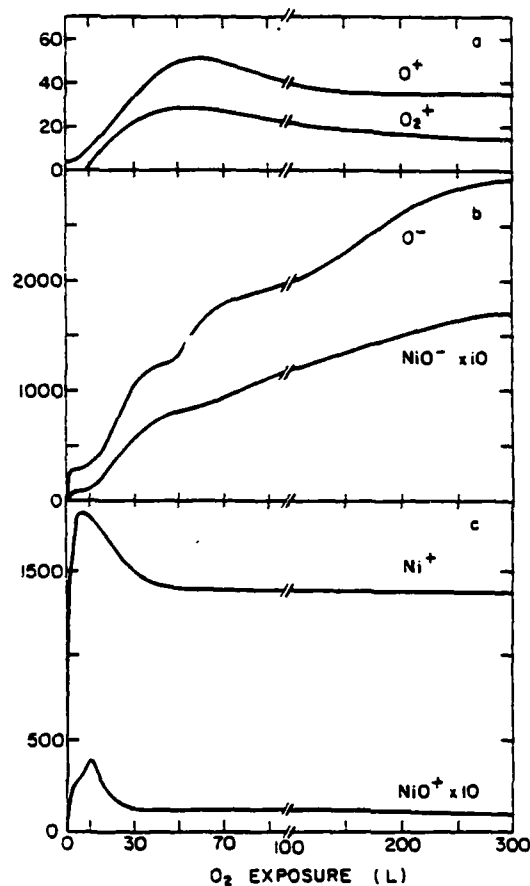
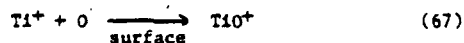


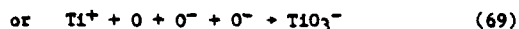
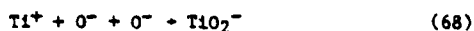
Figure 52 - Experimental ion yields vs oxygen exposure for Ni(001) bombarded by 2-keV Ar^+ ions. The ordinate gives the number of ions/s detected. From reference 158.

static SIMS, the ions Ti^+ , TiO^+ , TiO_2^+ and TiO_3^+ . If, for example, the TiO^+ species formed by recombination as



then suppression of the Ti^+ signal by Cs deposition should suppress the TiO^+ signal in a similar fashion. This experiment is superior to the O_2 on Ni situation since only small quantities of Cs (<0.25 monolayer) need to be deposited to change the ion yield by nearly three orders of magnitude. In addition, the oxygen coverage could be kept fixed during the entire analysis. His results showed that for the positive ions TiO^+ , TiO_2^+ and TiO_3^+ that the recombination model was clearly valid. For the negative ions, however, he found strong deviations from the predicted behavior. Because of this deviation, he concluded that these species probably formed directly by lattice fragmentation. It is of interest that he did

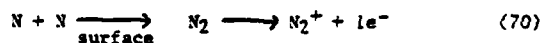
not consider reactions of the type



in his analysis. These pathways may indeed be favorable due to the long range attractive interaction that exists between oppositely charged atoms.

Yu has proposed, however, that since the electron affinity of negatively charged ions is usually low that unless the cluster constituents are in ground vibrational states that electron detachment is very favorable (166). To produce ground state molecules he feels it is necessary to invoke the condition that they form from nearest neighbors on the surface. Thus for the Ti-oxygen system, Yu proposes that the positive ions form by recombination while the negative ions are produced directly by lattice fragmentation.

Another possible mechanism for cluster ion formation has been suggested by Snowden and co-workers (167). In this scheme, which they tested by examining N_2^+ ejection from an ion bombarded nitrogen implanted silicon target, the electron is assumed to be emitted after formation of the N_2 molecule as



As shown in Figure 53, the first step (I) requires the ejection of two nitrogen atoms which form an N_2 molecule by the recombination mechanism. In the second step (II), the excited N_2 molecule vibrating within its molecular potential may cross to the N_2^+ potential curve by emitting an electron. This process can be detected in step (III) since the excited N_2^+ molecule decays to the ground state via a measurable photon. They provided evidence for this mechanism by determining that specific rotational levels of N_2^+ were populated during step (II). The proposed mechanism has considerable merit since essentially unbound N_2 molecules can be stabilized as N_2^+ by electron ejection. It has so far only been demonstrated to occur in this one instance, and it remains to be seen how common such processes really are. Further, the fact that they also found a continuum of vibrational and rotational states that were populated implies that a fraction of the N_2^+ molecules may form by ion-atom collisions.

Thus it appears that the relationship between ionization and cluster formation introduces a few additional twists when compared to cluster formation of the neutrals. Many of the basic ideas generated by the trajectory calculations, however, still appear to be valid and continue to provide valuable insight into the cluster ion formation process.

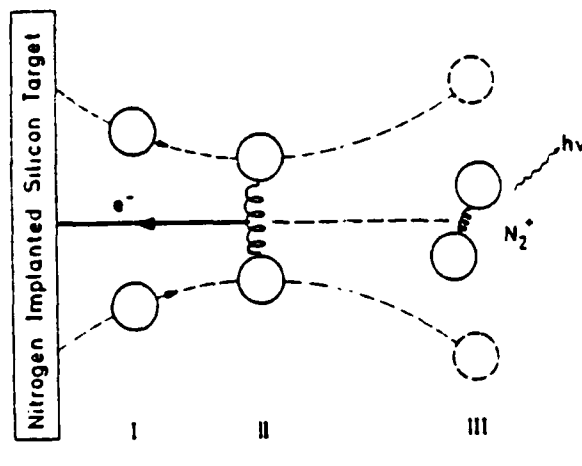


Figure 53 - Schematic illustration of the proposed sputtered molecule formation mechanism. The first step (I) requires the sputtering of two nitrogen atoms approaching on an appropriate collision trajectory. The second step (II) requires a molecular potential curve crossing followed by electron loss within a few molecular vibrations (the lifetime of the N_2 state). In the third step (III) the N_2^+ molecule decays to the ground state via photon emission. If the electron loss in II does not occur, the N_2 molecule generally predissociates and no N_2^+ is formed. From reference 5, p. 298.

VI. Molecular SIMS

The detection of molecular ions by static SIMS which are characteristic of the original sample has important implications in chemical analysis. The approach offers a complementary mass spectrometric method for vaporizing and ionizing nonvolatile or thermally unstable compounds. For example, in traditional mass spectrometry, a molecule is usually volatilized by heating, and ionized by electron impact. For molecules like amino acids, however, heating usually produces NH_3 and CO_2 whereas ion bombardment may directly produce the desired molecular ion. In other words, the sub-picosecond time scale of the ion impact event is sufficiently fast to beat out thermal rearrangements that occur on the nanosecond time scale.

The analysis of molecular solids by SIMS dates to the early investigations of Benninghoven on metal surfaces covered with rather ill-defined organic overlayers (168). From these observations, he and his co-workers found that even for very delicate organic molecules such as amino acids, ion bombarded powders of the sample could produce very well-defined spectra (51). For example, in Figure 54 is shown both the positive and

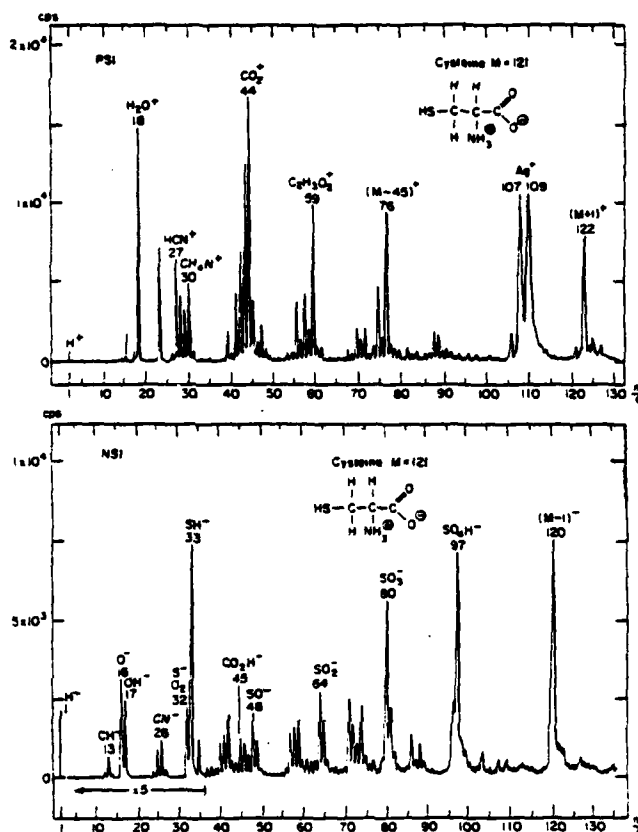


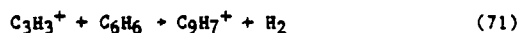
Figure 54 - Original positive and negative secondary-ion spectrum of cysteine on Ag. (Primary ion current: $2 \cdot 10^{-10}$ A. bombardment target area: 0.1 cm^2 . From reference 51.

negative ion spectra of cysteine deposited onto a silver foil. The main features of the spectra are the presence of the molecular ion peaks at $(M+1)^+$ and at $(M-1)^-$ and the rather simple fragmentation pattern associated with the lower mass ranges. The ultimate sensitivity of the method is $<10^{-12}$ grams, making SIMS a potentially very sensitive analytical tool (169,170). The cysteine example is a particularly powerful one since it is thermally unstable and the mass spectroscopy of amino acids is very tricky.

Many other experimental studies have now been reported which indicate that SIMS provides interesting information from almost any molecular solid. It is not our intent to review this field as it has recently been done quite capably by others (171,172). There are a number of mechanistic features of these experiments which are, however related to many of the ideas presented in earlier sections upon which we will focus.

A. A Model Study with Benzene

A good starting point in trying to understand the ejection of large molecules is to begin with an appropriate model system - in our case benzene. This molecule is simple enough to be examined theoretically yet large enough to be comparable in size to many of the more complex systems currently of interest to chemists. The static SIMS spectrum of this compound has been examined under a variety of conditions. Michl and co-workers first reported the spectrum of solid benzene at low mass (173) and was quickly extended to higher mass by Rabalais et al. (165). The spectrum is characterized by a series of hydrocarbon clusters of the stoichiometry C_nH_x where $n=1$ to 30 and x is on the order of n for $n < 10$ and on the order of $n/2$ for $n > 10$. The spectrum is clearly dominated by recombination of ejecting cluster sub-units, making direct identification of benzene itself nearly impossible. For example, the following types of gas phase reactions have been proposed to explain the formation of the larger carbon fragments (165):



A dramatically different spectrum is obtained by allowing benzene to chemisorb on a Ni(001) surface (174,175). For this situation, it is believed that the molecule forms an ordered $c(4 \times 4)$ (1/8 monolayer) overlayer with the benzene molecule laying flat on the surface in a close-packed arrangement (176,177). The geometry is sketched schematically in Figure 55. The SIMS spectrum consists almost entirely of the molecular ion complexed with a Ni atom as $NiC_6H_6^+$ as shown in Figure 56. Only weak fragmentation patterns are observed. Apparently, the benzene molecules are far enough apart such that recombination of the ejected molecule occurs mainly with Ni^+ .

One may question how these observations can be rationalized with the mechanistic ideas discussed in Section V. How, in the case of benzene, can 12 or more atoms be ejected from a solid retaining molecular structure information when bombardment energies are many times greater than chemical bond strengths? This situation has recently been modeled using the molecular dynamics treatment to see if the theory could be used to rationalize the experimental result using the structure shown in Figure 55 (101). The model was set-up by using a binding energy of 1.7 eV between the entire benzene molecule and the Ni surface. The majority of the interaction strength was arbitrarily put into the Ni-C interaction rather than into the Ni-H interaction. Also, interaction between benzene molecules was ignored. With this approach, the analysis indicated very high probability of C_6H_6 ejection with smaller amounts of fragments of the type C_6H_5 , C_5H_5 , C_2H_2 and CH. One case of NiC_6H_6 was also found where the species was formed by recombination of a Ni atom with a C_6H_6 unit.

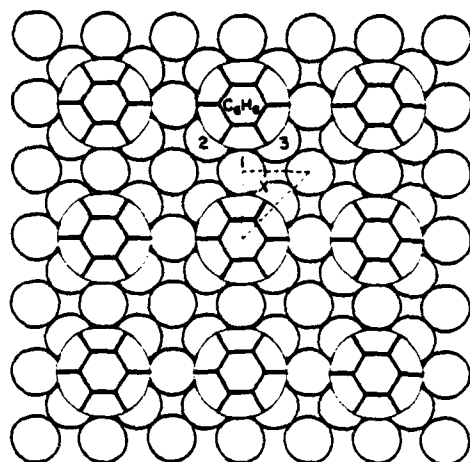


Figure 55 - Ni(001) with a c(4x4) overlayer of benzene, C_6H_6 . The dashed triangle is the impact zone for normal incidence ion bombardment. The numbered atoms correspond to the atoms shown in Figure 57. The x is the impact point for the Ar^+ ion which leads to the motion depicted in Figure 57. The circle around each C_6H_6 is the radial extent of the hydrogen position, 2.5 Å. From reference 101.

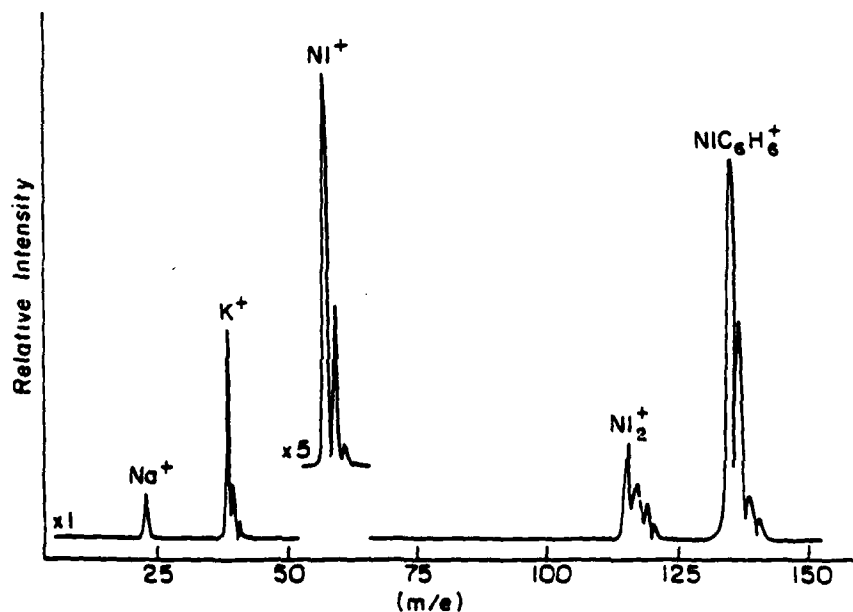


Figure 56 - SIMS spectrum of Ni(111) exposed to 3L of benzene at 300 K.

The calculations indicate that there are three factors that favor ejection of molecular fragments (101). First, a large molecule has many internal degrees of freedom and can absorb energy from an energetic collision without dissociating. Second, the more massive framework of a large organic molecule can be small in size compared to a metal atom, thus it is possible to strike several parts of the molecule in a concerted manner so that the entire molecule moves in one direction. Finally, by the time the organic molecule is struck, the energy of the primary ion has been dissipated so that the kinetic energies are tens of eVs rather than hundreds or thousands of eVs. A typical ejection sequence for benzene is shown in Figure 57.

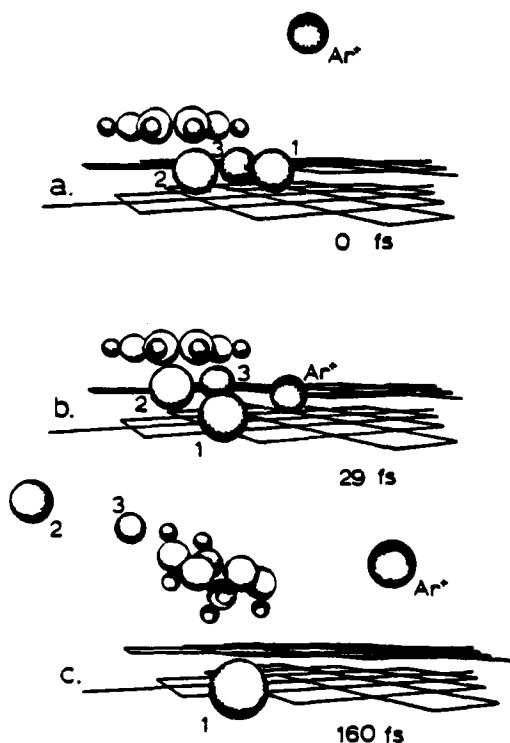


Figure 57 - Ejection of a C_6H_6 molecule by the simultaneous collision with two Ni atoms. Only the species (one Ar^+ ion, 3 Ni atoms and one C_6H_6 molecule) directly involved in the collision are shown. The grid lines are drawn between nearest neighbors in each plane, thus a Ni atom is initially situated at each intersection of lines. The sizes of the atoms are arbitrary. The elapsed time during the collision is shown in the lower right corner in femtoseconds (10^{-15} s).

- a) Initial positions of the atoms. The benzene is being viewed from the side.
- b) Positions as the 2 Ni atoms are about to collide with benzene.
- c) Distortion of the ejected benzene. From reference 101.

It should be noted here that the SIMS spectrum of water exhibits similar variations in cluster type with changes in the sample matrix. The spectrum of ice, for example, consists mainly of the series of ions $(H_2O)_nH^+$ with n up to at least 51 (165). When water is adsorbed on a cooled metal substrate, the $M(H_2O)_n^+$ ions dominate the spectrum (178).

B. Matrix Effects

The comparisons of the SIMS spectra of benzene under the different matrix conditions (solid benzene and benzene adsorbed on Ni(001)) suggest that fragmentation and recombination processes can be strongly influenced by sample preparation. This fact has been further demonstrated by a number of workers. Jonkman and Michl, for example, utilized a liquid He crystal to trap the organic molecule in solid argon in an attempt to simplify the spectra (179-181). For solid CH_4 , they found hydrocarbon fragments to masses assigned to $C_4H_7^+$ and higher. When CH_4 was diluted into an argon matrix [1:500] at 15 K, CH_4^+ was the highest molecular weight species observed (180). These effects are illustrated in Figure 58.

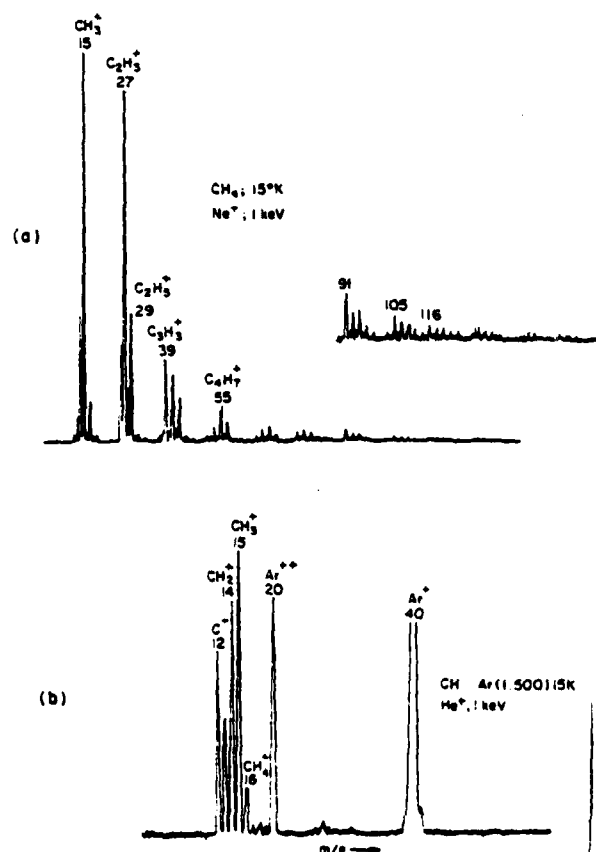


Figure 58 - (a) SIMS spectrum of neat methane at 15 K using 1 keV Ne^+ ions.
(b) SIMS spectrum of methane diluted in an argon matrix [1:500] at 15 K using 1 keV He^+ ions. From reference 180.

From reactions of the type given in Equations 71-73, it is obvious that the neutral molecule can be converted into an ion by recombination reactions. Cooks and co-workers have taken advantage of this idea by mixing large quantities of metal ions such as Li^+ and K^+ into the sample which results in intense cationized molecular ion peaks (182,183). These workers also found that p-aminobenzoic acid prepared as a film on Ag foil formed the argentated molecular ion $(\text{Ag}+\text{M})^+$ (182) as was found for benzene on $\text{Ni}(001)$.

C. Alkali Halides

The situation becomes more complex, but nonetheless fascinating, when the particles forming the cluster possess long range attractive forces. For the alkali halides MA, clusters of the type $(\text{MA})_n\text{M}^+$ and $(\text{MA})_n\text{A}^-$ are the most commonly observed species, with n increasing to numbers greater than 20 (178, 184-186). This situation is illustrated in Figure 59 for the positive ion spectrum of CsI (184). Presumably, these clusters form by recombination of an M^+ and A^- over the surface, a very favorable process due to the infinite range of the interaction. The (MA) molecule can then be sequentially cationized or anionized over the surface of the crystal to build up units contained in the observed cluster ion. The energy distributions tend to be narrower than the monomer ions (187). Further, there are certain cluster sizes which exhibit unusual stability. The peak at $n=13$, for example, is thought to be associated with a rhombohedral structure containing 27 atoms arranged in a $3 \times 3 \times 3$ structure.

D. Surface Reactions

In general, the SIMS spectra of monolayers adsorbed on metals appear to produce clusters which often minimize complexities introduced by recombination processes. This fact has inspired considerable research aimed toward utilizing SIMS to actually monitor surface reactions that may be occurring on surfaces. Benninghoven and co-workers have emphasized the sensitivity of SIMS to hydrogen by studying the reaction of H_2 with O_2 , C_2H_4 and C_2H_2 on polycrystalline Ni (188-190). For the $\text{H}_2 + \text{O}_2$ reaction, for example, they were able to detect an OH^- species at room temperature, a result similar to that found for the adsorption of H_2O on Ni under similar conditions (189). Other workers have followed the dehydrogenation of ethylene at 120 K on $\text{Ni}(111)$ (192). In a more complicated example, it has recently been observed that thiophene adsorbed on Ag undergoes a self hydrogenation to form tetrahydrothiophene (193).

E. Molecular SIMS and Related Methods

The search for new methods of introducing ions from non-volatile samples into a mass spectrometer has been of interest for many years. There is no question that static SIMS has

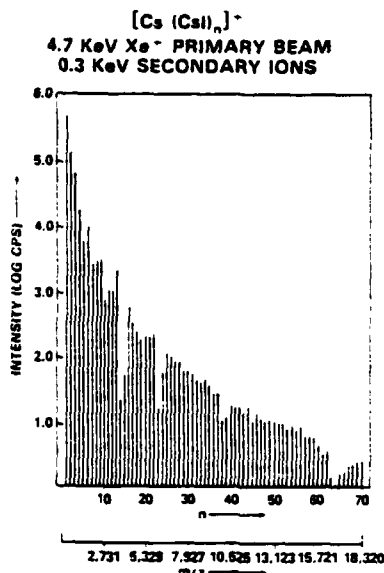


Figure 59 - Secondary ion mass spectra of CsI.
Figure courtesy of J.E. Campans.

found a niche in this field in the analysis of biochemical materials, inorganic and organic solids as well as salts and metals. It is interesting that there are currently two other approaches of very similar fundamental origin under current development. Macfarlane and co-workers have discovered that by bombardment of a thin mylar foil from the back by the fission products of a ^{252}Cf nucleus that molecular ions are ejected from the front of the foil (194,195). This technique has been referred to as plasma desorption mass spectrometry and is compared schematically to SIMS in Figure 60. We believe that the same general mechanisms of cluster formation are applicable to this method as well. Although the bombardment energy is in the MeV range and energy loss processes are almost certainly electronic in nature, any subsequent collision cascade emanating out from the fission track would lead to the ejection of clusters in a fashion nearly identical to SIMS. The fact that the $(M+1)^+$ and $(M-1)^+$ ions dominate the PDMS spectrum is qualitative evidence in support of this view (194). Of further interest is that a time-of-flight mass spectrometer has been developed to detect the ions. The spectrometer picks up its timing pulse from the individual ^{252}Cf fission event. This feature allows very high masses to be measured. The Macfarlane group, for example, has recently detected the molecular ion of a protein with m/e of greater than 12,000 (195).

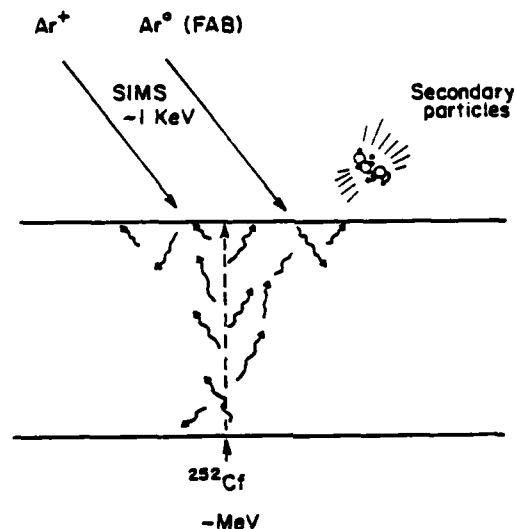


Figure 60 - Desorption due to energetic collision cascades.

Another approach has been the use of an atom beam rather than an ion beam to serve as the bombarding species (196,197). Probably for commercial reasons, the workers have termed the technique FAB or fast atom bombardment rather than SIMS. The physics of the two processes are completely identical and it is not clear why two names are needed (See Figure 60). On the other hand, the FAB source offers two unique practical advantages which promise to extend the SIMS applications. First, the use of an atom beam allows the secondary ions to be extracted from the sample with large electrostatic potential. The use of a primary ion would not be as straightforward since it would be deflected by such a field. Secondly, the proponents of the FAB source suggest that for insulating samples, charging is greatly minimized since the incident beam does not alter the sample charge. It is not yet clear that this apparent advantage cannot be offset by the use of standard charge compensation tools such as sample biasing and secondary electron flooding. It is of further interest, however, that these workers have discovered certain low vapor pressure liquids like glycerol which act as ideal solvents for the sample. For this case, the dilution by the matrix apparently minimizes recombination and serves to bring a continually fresh surface to the incident beam, virtually eliminating any sample damage problems. A typical SIMS spectrum taken using a FAB source and magnetic analyzer is shown in Figure 61.

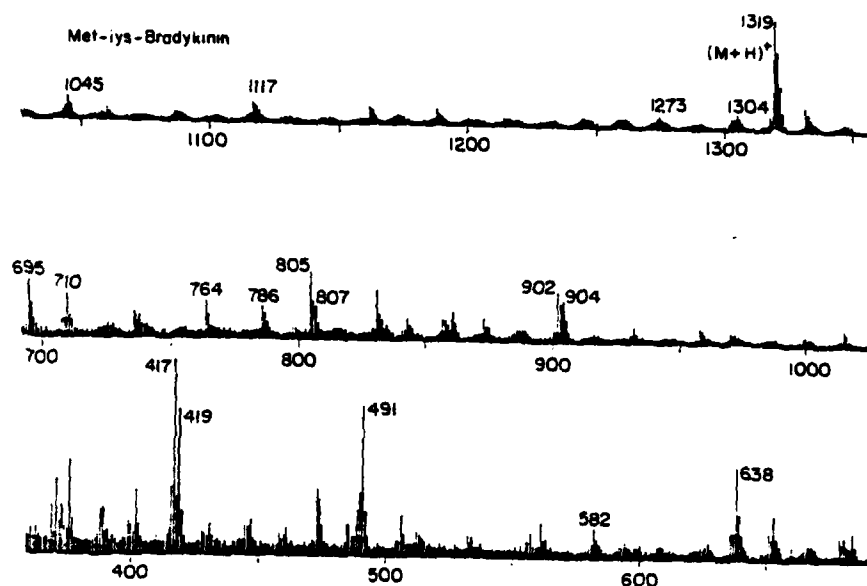


Figure 61 - Fast atom bombardment spectrum of undecapeptide, methionyl-lysl-brady-kinin, obtained from 1 μ g of material. From reference 197.

Acknowledgement

I would like to thank a number of my colleagues for helping me to gain the necessary perspective in this field. These include Barbara Garrison who has developed the thrust of our theoretical approach and has suggested many key experiments, and Don Harrison who got us originally involved in this field and gave generously of his knowledge about the ion bombardment process. Nick Delgass and Graham Cooks of Purdue University were extremely helpful in the initiation of our experimental program. Many graduate students and post-doctoral students have also been inspirational in helping to develop the approach presented here including: Rich Hewitt, George Slusser, Theo Fleisch, Rick Gibbs, Steven Holland, Alain Diebold, Karin Foley, and Eugene Karwacki.

I am also most appreciative of the help and cooperation provided by a variety of funding agencies - The National Science Foundation, The Air Force Office of Scientific Research, The Office of Naval Research, The Petroleum Research Foundation administered by the American Chemical Society, as well as The Pennsylvania State University.

References

1. G. Carter and J.S. Colligan, Ion Bombardment of Solids, American Elsevier, New York, 1968.
2. Inelastic Ion-Surface Collisions, Edited by N.H. Tolk, J.C. Tully, W. Heiland and C.W. White, Academic Press, 1977.
3. Atomic Collisions in Solids, Edited by D.P. Jackson, J.E. Robinson and D.A. Thompson, North Holland Publishing Co., New York, 1980.
4. Secondary Ion Mass Spectrometry SIMS-II, Edited by A. Benninghoven, C.A. Evans, Jr., R.A. Powell, R. Shimizu and H.A. Storms, Springer Series in Chemical Physics, 9, New York, 1980.
5. Proceedings of the Symposium on Sputtering, Edited by P. Varga, G. Betz and F.P. Viebock, Institute fur Allgemeine Physik Technische Universitat Wien, Vienna, 1980.
6. Inelastic Particle-Surface Collisions, Edited by E. Taglauer and W. Heiland, Springer Series in Chemical Physics 17, New York, 1981.
7. J.F. Van Der Veen, R.M. Tromp, R.G. Smeenk and F.W. Saris, Surf. Sci., **82**, 468 (1979).
8. M.W. Cole, D.R. Frankl and D.L. Goodstein, Rev. Mod. Phys., **53**, 199 (1981).
9. W. R. Grove, Trans. R. Soc. (London) **142**, 87 (1852).
10. P. Sigmond in Inelastic Ion-Surface Collisions, Edited by N.H. Tolk, J.C. Tully, W. Heiland and C.W. White, Academic Press, p. 121, 1977.
11. D. McKeown, Rev. Sci. Instrum., **32**, 133 (1961).
12. H. G. Scott, J. Appl. Phys., **33**, 2011 (1962).
13. M.W. Thompson and R.S. Nelson, Philos. Mag., **7**, 2015 (1962).
14. G. Carter, private communication.
15. G. K. Wehner, Advances in Electronics and Electron Physics, **7**, 239 (1955).
16. R.V. Stuart and G.K. Wehner, J. Appl. Phys., **35**, 1819 (1964).
17. D. Onderdelinden, Can. J. Phys., **46**, 739 (1968).
18. A.L. Southern, W.R. Willis, and M.T. Robinson, J. Appl. Phys., **34**, 153 (1963).
19. G.D. Magnuson and C.E. Carlston, J. Appl. Phys., **34**, 3267 (1963).
20. M. T. Robinson and A.L. Southern, J. Appl. Phys., **38**, 2969 (1967).
21. J.M. Fluit, P.K. Rol and J. Kistemaker, J. Appl. Phys., **34**, 690 (1963).
22. G.K. Wehner, Phys. Rev., **102**, 690 (1956).
23. G.S. Anderson and G.K. Wehner, J. Appl. Phys., **31**, 2305 (1960).
24. W. Szymczak and K. Wittmaack, Proceedings of the Symposium on Sputtering, Ed. by P. Varga, G. Betz and F.P. Viebock, Institute fur Allgemeine Physik Technische Universitat Wien, Vienna 1980.
25. T.R. Lundquist, J. Vac. Sci. Tech., **15**, 684 (1978).
26. H. Oechsner and W. Gerhard, Phys. Lett., **40A**, 211 (1972).
27. G.P. Konnen, J. Grosser, A. Haring, A.E. deVries and J. Kistemaker, Radia. Eff., **21**, 171 (1974).
28. J. Politiek and J. Kistemaker, Radia. Eff., **2**, 129 (1969).
29. E. Hulpke and Ch. Schlier, Z. Phys., **207**, 294 (1967).
30. H. Oechsner and W. Gerhard, Surf. Sci., **44**, 480 (1974).
31. D. Hammer, E. Benes, P. Blum and W. Husinsky, Rev. Sci. Instrum., **47**, 1178 (1976).
32. R.B. Wright, M.J. Pellin, D.M. Gruen and C.E. Young, Nucl. Instruments and Methods, **170**, 295 (1980).
33. A.L. Klein, Phys. Rev., **26**, 800 (1925).
34. R. Castaing and G. Slodzian, J. Microsc., **1**, 395 (1962).
35. H. Liebl, J. Appl. Phys., **38**, 5277 (1967).
36. K. Wittmaack in Inelastic Ion-Surface Collisions, Edited by N.H. Tolk, J.C. Tully, W. Heiland and C.W. White, Academic Press, p. 153, 1977.
37. G. Staudenmaier, W.O. Hofer and H. Liebl, Int. J. Mass. Spectrom. Ion, Phys., **21**, 103 (1976).
38. For example, H.W. Werner, Vacuum, **24**, 493 (1974).
39. A. Benninghoven, Phys. Status Solidi, **34**, K169 (1969).
40. A. Benninghoven, Surf. Sci., **28**, 541 (1971).
41. A. Benninghoven and E. Loebach, Rev. Sci. Instrum., **42**, 49 (1971).
42. P.H. Dawson and P.A. Redhead, Rev. Sci. Instrum., **48**, 159 (1977).
43. A. Benninghoven, Surf. Sci., **53**, 596 (1975).
44. R.E. Honig, J. Appl. Phys., **29**, 549 (1958).
45. R.E. Honig in Advances in Mass Spectrometry, R.M. Elliot, Ed., Vol. 2, p. 25, Pergamon Press, London, 1963.
46. G. Staudenmaier, Radia. Eff., **13**, 87 (1972).
47. K. Wittmaack and G. Staudenmaier, Appl. Phys. Lett., **27**, 318 (1975).
48. G.P. Konnen, A. Tip and A.E. DeVries, Radia. Eff., **21**, 269 (1974).
49. H.W. Werner, Surf. Sci., **47**, 301 (1975).
50. R. Buhl and A. Preisinger, Surf. Sci., **47**, 344 (1975).
51. A. Benninghoven, D. Jaspers and W. Sichtermann, Appl. Phys., **11**, 35 (1976).
52. F. Honda, Y. Fukuda and J.W. Rabalais, J. Chem. Phys., **70**, 4834 (1979).
53. M. Barber, J.C. Vickerman and J. Wolstenholme, Faraday Trans. I, **72**, 40, (1976).

AD-A112 904

PENNSYLVANIA STATE UNIV UNIVERSITY PARK DEPT OF CHEMISTRY F/8 7/4
CHARACTERIZATION OF SOLIDS AND SURFACES USING ION BEAMS AND MAS--ETC(U)
DEC 81 N WINOGRAD
N00014-80-C-0491

UNCLASSIFIED TR-4

NL

2 OF 2

AD-A
112 904



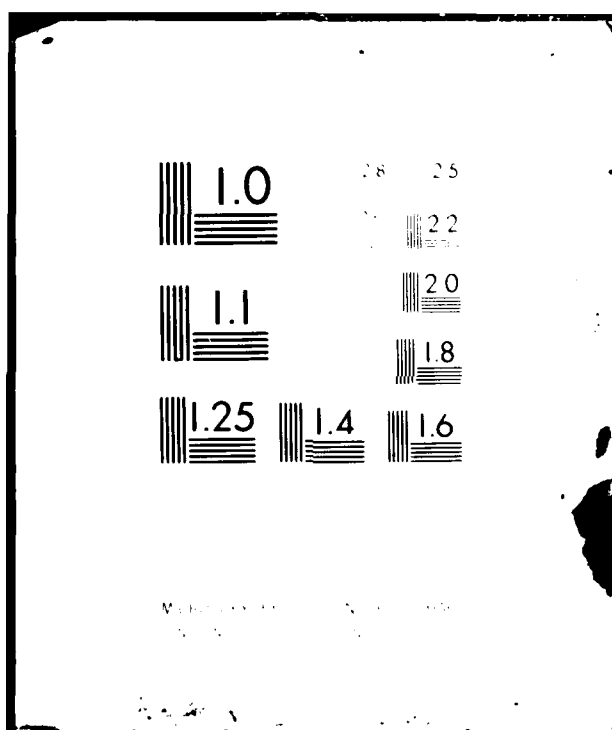
END

DATE

FILED

04-82

DTIC



54. M. Barber, J.C. Vickerman and J. Wolstenholme, *J. Catal.*, **42**, 48 (1976).
55. P. Sigmund, *Phys. Rev.*, **184**, 383 (1969).
56. P. Sigmund, *Phys. Rev.*, **187**, 768 (1969). (Errata)
57. P. Sigmund, *Rev. Roum. Phys.*, **17**, 1079 (1972).
58. M.W. Thompson, *Philos. Mag.*, **18**, 377 (1968).
59. P.D. Townsend, *Radia. Eff.*, **37**, 253 (1978).
60. I.S.T. Tsong and D. J. Barber, *J. Mater. Sci.*, **8**, 123 (1973).
61. J. Lindhard, V. Nielsen and M. Scharff, *Mat. Fys. Medd., Dan Vid. Selsk.* **36**, No. 10 (1968).
62. K.S. Kim, W.E. Baitzinger and N. Winograd, *Surf. Sci.*, **55**, 285 (1976).
63. D. Almen and G. Bruce, *Nucl. Instrum. Methods*, **11**, 257 (1961).
64. R.B. Wright and D.M. Gruen, *J. Chem. Phys.*, **72**, 147 (1980).
65. M.J. Pellin, R.B. Wright and D.M. Gruen, *J. Chem. Phys.*, **74**, 6448 (1981).
66. G.P. Konnen, A. Tip and A.E. deVries, *Radia. Eff.*, **21**, 269 (1974).
67. G.P. Konnen, A. Tip and A.E. deVries, *Radia. Eff.*, **26**, 23 (1975).
68. W. Gerhard, *Z. Phys.*, **B22**, 31 (1975).
69. See for example, D.G. Truhlar and J.T. Muckerman in *Atom Molecule Collision Theory*, R.B. Bernstein, Ed., Plenum Press, New York, 1979.
70. See for example, P. Lykos, Ed., *ACS Symp. Ser.*, No. 86 (1978).
71. D.J. Rossky and M. Karplus, *J. Am. Chem. Soc.*, **101**, 1913 (1979).
72. J.B. Gibson, A.N. Goland, M. Milgram and G.H. Vineyard, *Phys. Rev.*, **120**, 1229 (1960).
73. C. Erginsoy, G.H. Vineyard and A. Englert, *Phys. Rev.*, **133**, A595 (1964).
74. C. Erginsoy, G.H. Vineyard and A. Shimizu, *Phys. Rev.*, **139**, A118 (1965).
75. W.L. Gay and D.E. Harrison, Jr., *Phys. Rev.*, **135**, A1780 (1964).
76. D.E. Harrison, Jr., W.L. Moore and H.T. Holcombe, *Radia. Eff.*, **17**, 167 (1973).
77. D.E. Harrison, Jr., N.S. Levy, J.P. Johnson and H.M. Effron, *J. Appl. Phys.*, **39**, 3742 (1968).
78. R.H. Silsbee, *J. Appl. Phys.*, **28**, 1246 (1957).
79. D.P. Jackson and D.V. Morgan, *Contemp. Phys.*, **14**, 25 (1974).
80. D.P. Jackson, *Can. J. Phys.*, **53**, 1513 (1975).
81. M.T. Robinson and O.S. Oen, *Phys. Rev.*, **132**, 2385 (1963).
82. M.T. Robinson and I.M. Torrens, *Phys. Rev.*, **B9**, 5008 (1974).
83. V.E. Yurasova, V.I. Shulga and D.S. Karpuzov, *Can. J. Phys.*, **46**, 759 (1968).
84. M. Hou and M.T. Robinson, *Nucl. Instr. Methods*, **132**, 641 (1976).
85. M. Hou and M.T. Robinson, *Applied Physics*, **18**, 381 (1979).
86. G. Betz, R. Dobrozensky and F.P. Viehbock, *Int. J. Mass. Spect. Ion Phys.*, **6**, 451 (1971).
87. I. Ishitani and R. Shimizu, *Appl. Phys.*, **6**, 241 (1975).
88. L.G. Haggmark and W.D. Wilson, *J. Nucl. Mater.*, **76**, 149 (1978).
89. V.E. Yurasova, V.I. Shulga, I.G. Bunin, B.M. Mamaev, L.N. Nevsorova, A.S. Petrov, *Radia. Eff.*, **27**, 173 (1976).
90. D.E. Harrison, Jr., W.L. Gay and H.M. Effron, *J. Math Phys.*, **10**, 1179 (1969).
91. W.H. Miller and T.F. George, *J. Chem. Phys.*, **56**, 5668 (1972).
92. K.E. Foley and B.J. Garrison, *J. Chem. Phys.*, **72**, 1018 (1980).
93. D.E. Harrison, Jr. and C.B. Delaplain, *J. Appl. Phys.*, **47**, 2252 (1976).
94. B.J. Garrison, N. Winograd and D.E. Harrison, Jr., *J. Chem. Phys.*, **69**, 1440 (1978).
95. I.M. Torrens, *Interatomic Potentials*, Academic Press, New York, 1972, Chapter 8.
96. A. Anderman, AFRL-66-88 Atomics International, Canoga Park, California, unpublished. See also reference 76.
97. S. Kapur and B.J. Garrison, *J. Chem. Phys.*, **75**, 445 (1981).
98. D.E. Harrison, Jr., B.J. Garrison and N. Winograd in *Secondary Ion Mass Spectrometry SIMS-II*, Edited by A. Benninghoven, C.A. Evans, Jr., R.A. Powell, R. Shimizu and H. A. Storms, Springer Series in Chemical Physics 9, New York, 1980 p. 12.
99. B.J. Garrison, N. Winograd and D.E. Harrison, Jr., *Phys. Rev.*, **B18**, 6000 (1978).
100. N. Winograd, B.J. Garrison and D.E. Harrison, Jr., *J. Chem. Phys.*, **73**, 3473 (1980).
101. B.J. Garrison, *J. Am. Chem. Soc.*, **102**, 6553 (1980).
102. D.M. Hayes, M. Barber and J.H.R. Clarke, *Surf. Sci.*, **105**, 225 (1981).
103. B.J. Garrison, *Surf. Sci.*, in press.
104. H.A. Storms, R.F. Brown and J.D. Stein, *Anal. Chem.*, **49**, 2023 (1977).
105. C.A. Andersen and J.R. Hinthorne, *Science*, **175**, 853 (1972).
106. T. Fleish, G.L. Ott, N. Winograd and W.N. Delgass, *Surf. Sci.*, **78**, 141 (1978).
107. H. Oechsner, W. Ruhe, and E. Stumpe, *Surf. Sci.*, **85**, 289 (1979).
108. H. Oechsner, H. Schoof, and E. Stumpe, *Surf. Sci.*, **76**, 343 (1978).
109. M. L. Yu, *Phys. Rev. B*, in press.
110. G. Slodgian and J.F. Hennequin, *Compt. Rend. (Paris)* **B263** 1246 (1966).
111. V. Krohn, *J. Appl. Phys.*, **33**, 3523 (1962).
112. P. Williams and C.A. Evans, Jr., *Surf. Sci.*, **78**, 324 (1978).
113. V.E. Yurasova, A.A. Sysyov, G.A. Samsonov, V.N. Bukhanov, L.N. Nevsorova, and L.B. Shelyakin, *Radia. Eff.*, **20**, 89 (1973).
114. S.P. Holland, B.J. Garrison and N. Winograd, *Phys. Rev. Lett.*, **44**, 756 (1980).
115. R.A. Gibbs, S.P. Holland, K.E. Foley, B.J. Garrison and N. Winograd, *J. Chem. Phys.*, submitted.

116. E. Taglauer, W. Englert, W. Heiland and D.P. Jackson, *Phys. Rev. Lett.*, **45**, 740 (1980).
117. D.J. Godfrey and D.P. Woodruff, *Surf. Sci.*, **105**, (1981).
118. D.J. Godfrey and D.P. Woodruff, *Surf. Sci.*, **89**, 76 (1979).
119. F.G. Satkiewicz, *Proc. 23rd Ann. Conf. on Mass Spectrometry*, Houston Texas, 1975.
120. R. A. Gibbs and N. Winograd, *Rev. Sci. Instruments*, **52**, 1148 (1981).
121. C.A. Andersen and J.R. Hinthorne, *Anal. Chem.*, **45**, 1421 (1973).
122. P. Williams, *Surf. Sci.*, **90**, 588 (1979).
123. V. Deline, C.A. Evans, Jr., and P. Williams, *Appl. Phys. Lett.*, **33**, 578 (1978).
124. Z. Sroubek, *Surf. Sci.*, **44**, 47 (1974).
125. Z. Sroubek, in *Inelastic Particle-Surface Collisions*, Edited by E. Taglauer and W. Heiland, Springer Series in Chemical Physics 17, p. 277 (1981).
126. L.I. Schiff, *Quantum Mechanics*, McGraw-Hill, New York, 1968, p. 282.
127. J.K. Norskov and B.I. Lundqvist, *Phys. Rev. B*, **19**, 5661 (1979).
128. Z. Sroubek, K. Zdansky and J. Zavadil, *Phys. Rev. Lett.*, **45**, 580 (1980).
129. J.C. Tully in *Dynamics of Molecular Collisions, Part B*, Edited by W. H. Miller, Plenum Press, New York, 1976.
130. Z. Sroubek, J. Zavadil, F. Kubec and K. Zdansky, *Surface Sci.*, **77**, 603 (1978).
131. A.C. Diebold, B.J. Garrison and Z. Sroubek, to be published. 132. G. Slodzian, *Surf. Sci.*, **48**, 161 (1975).
133. M.L. Yu, *Phys. Rev. Lett.*, **40**, 574 (1978).
134. W.F. Van der Weg and D.J. Bierman, *Physica*, **44**, 206 (1969).
135. H.D. Hagstrom, *J. Vac. Sci. Technol.*, **12**, 7 (1975).
136. M.W. Siegel and M.J. Vasil, *Rev. Sci. Instrum.*, in press.
137. C.W. White and N.H. Tolk, *Phys. Rev. Lett.*, **26**, 486 (1971).
138. R.A. Gibbs, S. P. Holland, K.E. Foley, B.J. Garrison and N. Winograd, *Phys. Rev. B*, submitted.
139. M. L. Yu, *Phys. Rev. Lett.*, submitted.
140. P. Williams, *Phys. Rev. B*, **23**, 6187 (1981).
141. M.L. Knorek and P.J. Feibelman, *Phys. Rev. Lett.*, **40**, 964 (1968).
142. D.E. Harrison, Jr., P.W. Kelly, B.J. Garrison and N. Winograd, *Surf. Sci.*, **76**, 311 (1978).
143. C. Lehmann and P. Sigmund, *Phys. Status Sol.*, **16**, 507 (1966).
144. N. Winograd, B.J. Garrison and D.E. Harrison, Jr., *Phys. Rev. Lett.*, **41**, 1120 (1978).
145. R.G. Muscat and H.P. Smith, Jr., *J. Appl. Phys.*, **39**, 3579 (1968).
146. H.F. Winters and P. Sigmund, *J. Appl. Phys.*, **45**, 4760 (1974).
147. E. Taglauer, U. Beitz and W. Heiland, *Third International Conference on Ion Beam Analysis Proceedings*, Washington D.C., 1977 (unpublished).
148. N. Winograd and B.J. Garrison, *Acc. of Chem. Res.*, **13**, 406 (1980).
149. S.P. Holland, B.J. Garrison and N. Winograd, *Phys. Rev. Lett.*, **43**, 220 (1979).
150. S. Kapur and B.J. Garrison, *Surf. Sci.*, in press.
151. T. Fleisch, G.L. Ott, W.N. Delgass and N. Winograd, *Surf. Sci.*, **81**, 1 (1979).
152. H. Grade, N. Winograd and R.G. Cooks, *J. Am. Chem. Soc.*, **99**, 7725 (1977).
153. A.P.M. Baede, W.F. Jungmann and J. Los, *Physica*, **54**, 459 (1971).
154. B. Rosen, *International Tables of Selected Constants*, Pergamon, New York, 1970.
155. N. Winograd, D.E. Harrison, Jr., and B.J. Garrison, *Surf. Sci.*, **78**, 467 (1978).
156. M. Barber, R.S. Bardoli, J.C. Vickerman and J. Wolstenholme, *Proc. 7th Intern. Vac. Congr. and 3rd Intern. Conf. Solid Surf.*, Vienna 1977 p. 983.
157. G. Staudenmaier, *Radia. Eff.*, **18**, 181 (1973).
158. N. Winograd, B.J. Garrison, T. Fleisch, W.N. Delgass, and D.E. Harrison, Jr., *J. Vac. Sci. Technol.*, **16**, 629 (1979).
159. R.W. Hewitt and N. Winograd, *Surf. Sci.*, **78**, 1 (1978).
160. B.J. Garrison, N. Winograd and D.E. Harrison, Jr., *J. Vac. Sci. Technol.*, **16**, 789 (1979).
161. H. Hopster and C.R. Brundle, *J. Vac. Sci. Technol.*, **16**, 548 (1979).
162. P.H. Dawson and W.C. Tam, *Surf. Sci.*, **91**, 153 (1980).
163. M. Karplus, R.N. Porter and R.D. Sharma, *J. Chem. Phys.*, **43**, 3259 (1965).
164. R.R. Cordeman, P.C. Engelking and W.C. Lineberger, *Appl. Phys. Lett.*, **36**, 533 (1980).
165. G.M. Lancaster, F. Honda, Y. Fukuda and J.W. Rabalais, *J. Am. Chem. Soc.*, **101**, 1951 (1979).
166. M. Yu, *Appl. of Surf. Sci.*, in press.
167. K.J. Snowden, W. Heiland and E. Taglauer, *Phys. Rev. Lett.*, **46**, 284 (1981).
168. A. Benninghoven, *Surf. Sci.*, **35**, 427 (1973).
169. A. Benninghoven and W.K. Sichtermann, *Anal. Chem.*, **50**, 1180 (1978).
170. S.E. Unger, T.M. Ryan and R.G. Cooks, *Anal. Chim. Acta.*, **118**, 169 (1980).
171. R.J. Colton, *J. Vac. Sci. Tech.*, **18**, 737 (1981).
172. R.J. Day, S.E. Unger and R.G. Cooks, *Anal. Chem.*, **52**, 557A (1980).
173. H.T. Jonkman, J. Michl, R.N. King and J.D. Andrade, *Anal. Chem.*, **50**, 2078 (1978).
174. W.N. Delgass, private communication.
175. E. Karwacki and N. Winograd, to be published.
176. J.C. Bertolini, G. Dalmai-Imelik and J. Rousseau, *Surf. Sci.*, **67**, 478 (1977).
177. J.C. Bertolini and J. Rousseau, *Surf. Sci.*, **89**, 467 (1979).

178. J. Estel, H. Hoinkes, H. Kasermann, H. Nahr and H. Wilsch, *Surf. Sci.*, 54, 393 (1976).
179. H.T. Jonkman and J. Michl, *Chem. Commun.*, 751 (1978).
180. H.T. Jonkman and J. Michl, in *Secondary Ion Mass Spectrometry - SIMS-II*, Edited by A. Benninghoven, C.A. Evans, Jr., R.A. Powell, R. Shimizu and H.A. Storms, Springer Series in Chemical Physics 9, New York, 1980 p. 292.
181. H.T. Jonkman and J. Michl, *J. Am. Chem. Soc.*, 103, 733 (1981).
182. R. Grade and R.G. Cooks, *J. Am. Chem. Soc.*, 100, 5615 (1978).
183. R.J. Day, S.E. Unger and R.G. Cooks, *J. Am. Chem. Soc.*, 101, 501 (1978).
184. R.J. Colton, J.E. Campana, T.M. Barlak, J.J. DeCorpo and J.R. Wyatt, *Rev. Sci. Instrum.*, 51, 1685 (1980).
185. J.A. Taylor and J.W. Rabalais, *Surf. Sci.*, 74, 229 (1978).
186. F. Honda, G.M. Lancaster, Y. Fukuda and J.W. Rabalais, *J. Chem. Phys.*, 69, 4931 (1978).
187. P.T. Murray and J.W. Rabalais, *J. Am. Chem. Soc.*, 103, 1007 (1981).
188. A. Benninghoven, K.H. Muller, M. Schemmer, and P. Beckmann, *Appl. Phys.*, 16, 367 (1978).
189. A. Benninghoven, P. Beckmann, K.H. Muller and M. Schemmer, *Surf. Sci.*, 89, 701 (1979).
190. K.H. Muller, P. Beckmann, M. Schemmer, and A. Benninghoven, *Surf. Sci.*, 325 (1979).
191. A. Benninghoven, K.H. Muller, C. Plog, M. Schemmer, and P. Steffens, *Surf. Sci.*, 63, 403 (1977).
192. D.J. Surman, J.C. Vickerman and J. Wolstenholme, *LeVide, Les Couches Minces*, 201, 525 (1980).
193. S.E. Unger, R.G. Cooks, B.J. Steinmetz and W.N. Delgass, *Surf. Sci. Lett.*, submitted.
194. R.D. Macfarlane and R.D. Torgenson, *Science*, 191, 920 (1976).
195. R.D. Macfarlane, *J. Am. Chem. Soc.*, 103, 1609 (1981).
196. D.J. Surman and J.C. Vickerman, *J. Chem. Soc., Chem. Commun.*, 324, (1981).
197. M. Barber, R.S. Bordoli, R.D. Sedgewick and A.N. Tyler, *J. Chem. Soc., Chem. Comm.*, 325 (1981).

DATE
FILMED
-8